New Computational And Experimental Approaches For Studying Ion Acceleration And The Intense Laser-Plasma Interaction

DISSERTATION

Presented in Partial Fulfillment of the Requirements for the Degree Doctor of Philosophy in the Graduate School of The Ohio State University

By

Ginevra E. Cochran, B.S., M.S.

Graduate Program in Physics

The Ohio State University

2018

Dissertation Committee:

Professor Douglass Schumacher, Advisor

Professor Louis DiMauro

Professor Robert Perry

Professor Junko Shigemitsu

Abstract

This thesis studies the relativistic laser plasma interaction ($a_0 = eE_0/m_e\omega c > 1$) using joint experimental and computational approaches, the former using high power, short pulse laser systems and the latter via particle-in-cell (PIC) modeling and high performance computing. Different aspects are explored including determination of criteria for physically meaningful PIC simulations, development of the technology needed for such experiments including new systems for targetry and a new model for understanding dielectric plasma mirrors and, finally, a study of laser based ion acceleration in three different acceleration regimes.

We have shown that, although in the laboratory frame an electron accelerated via direct laser acceleration undergoes a decreased oscillation frequency, the criterion on the time resolution required to model this process actually becomes more restrictive. This is due to the difficulty of resolving the stopping points in the electron trajectory giving rise to dephasing. It is shown that when using the Boris particle pusher, the time step must satisfy $\Delta t \ll T/a_0$, where a_0 is the dimensionless vector potential. An adaptive time step algorithm based on this criterion is demonstrated that achieves more than an order of magnitude improvement in preserving the constant of the motion $\gamma - p_x/m_e c = 1$ with only a $1/\sqrt{a_0}$ increase in the number of time steps required, as opposed to the $1/a_0$ scaling in the non-adaptive algorithm.

High pulse contrast is crucial for performing many experiments on high intensity lasers in order to minimize modification of the target surface by pre-pulse. Dielectric plasma mirrors are commonly used to enhance the contrast of laser pulses and their subsequent ion production, but have not been modeled extensively. Presented here are novel 2D3V LSP particle-in-cell simulations of liquid crystal plasma mirror operation which include

a dielectric model with a population of cold neutral atoms and incorporating multiphoton ionization, low temperature modifications to the collision model, and dimensionality corrections. For the first time, plasma mirror behavior is modeled as a function of laser intensity, with excellent agreement to experiment over three orders of magnitude. In the future, this simulation framework can be used to make predictions about plasma mirror behavior about aspects that are difficult to measure, such as pulse shortening and mode degradation at full power.

Results from a high-contrast, ion acceleration experiment are presented, which used the Draco laser ($\sim$3 J, 10^{21} W/cm^2) at 45° angle of incidence on liquid crystal targets. 450 shots were collected in 5 days with each shot having up to 9 diagnostics in use. The data showed predominantly target normal directed ions for all target thicknesses from > 1 μm down to 10 nm, with peak protons energies up to 26 MeV found for the thinnest targets. Target normal ions are often considered to be an indication of the target normal sheath acceleration (TNSA) mechanism, but the TNSA-like signal in this experiment persisted down to target thicknesses < 30 nm, well under a predicted theoretical transition to radiation pressure acceleration (RPA) of ~ 130 nm for these conditions. By comparison, experimental measures of the transmitted light and particle-in-cell simulations indicate that relativistic transparency was achieved for 30 nm targets. 3D particle-in-cell simulations using LSP reproduce the dominance of target normal acceleration seen in the DRACO experiment with a good quantitative match to experimental peak proton energies. Tracking individual particles in simulations reveals that target normally directed ions are produced by TNSA for thick targets, but by radiation pressure acceleration (RPA) for thin targets. A simple analytical model is derived for RPA-driven target deformation that agrees well with 2D and 3D simulation results, supporting this conclusion. Using these simulations, the amount of energy in accelerated protons can be broken down into TNSA and RPA contributions. For a 300 nm target, TNSA makes up 90% of this energy with RPA contributing 10%, while in a 100 nm target TNSA and RPA each make up 30%, with the remaining due to relativistic transparency effects.

In memory of my grandmothers, Shirley Price and Betty Cochran

Acknowledgments

"Knowledge is like the honey in the flower, the industrious bee gathers and stores it away for a useful purpose..."
—W.G. Cochran, Reminiscences Of A Forty-Niner

"How will I food if I don't physics for money?"
—M. McMahon

To my advisor Douglass Schumacher, who I have learned so much from over the last six years. Thank you for supporting me in my obstinate quest to be both a modeler and an experimentalist. I hope to one day have half as much confidence in myself as you have shown in me.

I would also like to thank my undergraduate advisor David Dunlap, who first introduced me to research, and fanned the flames of my interest in physics with his enthusiasm; Scott Wilks, who has given me much valuable feedback about my simulation projects; and my collaborator Alexey Arefiev. All of your advice and support over the years has been greatly appreciated.

No PhD emerges from Scarlet without owing a great deal to Becky, who does three jobs better than I do one, and whose wicked sense of humor has brightened many a sad laser day for all of us. We should pay you more.

I am lucky to have been able to count my grad student mentors as my friends. Drs. Poole and Willis, who have formed much of my template for how to be a scientist; Drs. McMahon and King, who were ready with a helping hand for my modeling troubles. Thanks for always indulging my curiosity and for introducing me to video games.

My officemates Anthony and Alex, thank you for your willingness to talk out a problem

with me, or have a knock-down fight over what constitutes a taco. I'll miss you!

I have always been able to count on my comrade-in-arms Sarah to raise my spirits or commiserate with me about a rough day in the lab. Joanna and Stephanie, thank you for taking care of me even from far away.

Lastly, to Mom, Dad, Alex, Roddy, Sam, and Ben, who have always lent a patient, much-needed ear, and as a result have learnt far more about my research than they cared to know - but who love me anyway.

Vita

June 24, 1990	Born—Colorado Springs, CO
May 2008	Del Norte High School
May 2012	B.S. in Physics and Applied Mathematics Cum Laude, University of New Mexico, Albuquerque, NM
May 2015	M.S. in Physics, The Ohio State University, Columbus, OH

Publications

"On-shot characterization of single plasma mirror temporal contrast improvement". L. Obst, J. Metzkes-Ng, S. Bock, G. E. Cochran, T. E. Cowan, T. Oksenhendler, P. L. Poole, I. Prencipe, M. Rehwald, C. Rodel, H.-P. Schlenvoigt, U. Schramm, D. W. Schumacher, T. Ziegler, and K. Zeil, *Plasma Physics and Controlled Fusion*, **60**, 054007 (2018).

"Laser-driven ion acceleration via target normal sheath acceleration in the relativistic transparency regime". P. L. Poole, L. Obst, G. E. Cochran, J. Metzkes, H.-P. Schlenvoigt, I. Prencipe, T. Kluge, T. Cowan, U. Schramm, D. W. Schumacher, K. Zeil, *New Journal of Physics*, **20**, 013019 (2018).

"Liquid Crystal Targets and Plasma Mirrors For Laser Based Ion Acceleration". D. W. Schumacher, P. L. Poole, C. Willis, G. E. Cochran, R. Daskalova, J. Purcell, R. Heery, *Journal of Instrumentation*, **12**, C04023 (2017).

"Moderate repetition rate ultra-intense laser targets and optics using variable thickness liquid crystal films". P. L. Poole, C. Willis, G. E. Cochran, R. T. Hanna, C. D. Andereck, D. W. Schumacher, *Applied Physics Letters*, **109**, 151109 (2016).

"Experiment and simulation of novel liquid crystal plasma mirrors for high contrast, intense laser pulses". P. L. Poole, A. Krygier, G. E. Cochran, P. S. Foster, G. G. Scott, L. A. Wilson,

J. Bailey, N. Bourgeois, C. Hernandez-Gomez, D. Neely, P. P. Rajeev, R. R. Freeman, D. W. Schumacher, *Scientific Reports*, **6**, 32041 (2016).

"Criterion for correctly simulating relativistic electron motion in a high-intensity laser field". Alexey V. Arefiev, Ginevra E. Cochran, Douglass W. Schumacher, Alexander P. L. Robinson, Guangye Chen, *AIP Conference Proceedings*, **1777**, 050001 (2016).

"Liquid Crystals as High Repetition Rate Targets for Ultra Intense Laser Systems". Patrick Poole, Christopher Willis, Ginevra Cochran, Matthew McMahon, Enam Chowdhury, C. David Andereck, Douglass Schumacher, *Frontiers in Optics 2015*, FTh3A.5 (2015).

"Temporal resolution criterion for correctly simulating relativistic electron motion in a high-intensity laser field". Alexey V. Arefiev, Ginevra E. Cochran, Douglass W. Schumacher, Alexander P. L. Robinson, Guangye Chen, *Physics of Plasmas*, **22**, 013103 (2015).

Presentations

"Identifying ion acceleration regimes using ultrathin targets at non-normal laser incidence". G.E. Cochran, P.L. Poole, T. Cowan, T. Kluge, J. Metzkes-Ng, L. Obst, I. Principe, H.-P. Schlenvoigt, U. Schramm, K. Zeil, D.W. Schumacher, *NNSA/CEA-DAM Postdoctoral Exchange Workshop for the International Agreement on Fundamental Science*, Paris, France (2018).

"Ultraintense laser ion acceleration and contrast-enhancing plasma mirrors - experiment and simulations.". G. E. Cochran, *University of California San Diego - Center for Energy Research*, invited talk, San Diego, CA (2018).

"Investigating Ultraintense Laser Ion Acceleration Regimes With 3D Particle-In-Cell Simulations". G. E. Cochran, *Ohio Supercomputer Center Statewide Users Group Meeting*, Columbus, OH (2018).

"Particle-in-cell modeling of plasma mirrors from dielectric response to saturation". G. E. Cochran, *JIFT Japan-US workshop on theory and simulation on the high field and high energy density physics*, Hiroshima, Japan (2018).

"Particle-in-cell studies of ultrathin target ion acceleration at non-normal laser incidence". G. E. Cochran, P. L. Poole, D. W. Schumacher, *Stewardship Science Academic Programs Symposium*, Bethesda, MD (2018).

"Studying Ultrashort Pulse Laser Ion Acceleration At Non-Normal Incidence With 3D Particle-In-Cell Simulations". G. E. Cochran, P. L. Poole, D. W. Schumacher, *National Ignition Facility/Jupiter Laser Facility Users Meeting*, Livermore, CA (2018).

"Particle-in-cell simulations of ultrashort, ultraintense laser plasma mirror operation and ion acceleration". G. E. Cochran, P. L. Poole, D. W. Schumacher, *Voss Scientific* invited talk, Albuquerque, NM (2017).

"Ultrashort, ultraintense laser plasma optics and ion acceleration simulations and experiment". G. E. Cochran, P. L. Poole, D. W. Schumacher, *Los Alamos National Laboratory - XCP-6* invited talk, Los Alamos, NM (2017).

"Ultrathin Target Laser Ion Acceleration At Oblique Incidence". G. E. Cochran, P. L. Poole, D. W. Schumacher, *Division of Plasma Physics Annual Meeting*, Milwaukee, WI (2017).

"Modeling plasma mirrors for laser pulse contrast enhancement". G. E. Cochran, P. L. Poole, A. Kryiger, R. R. Freeman, D. W. Schumacher, *OSU Physics Poster Competition*, top prize, Columbus, OH (2017).

"Experiments and PIC simulations on liquid crystal plasma mirrors for pulse contrast enhancement". G. E. Cochran, P. L. Poole, D. W. Schumacher, *Division of Plasma Physics Annual Meeting*, San Jose, CA (2016).

"PIC simulations of liquid crystal plasma mirrors for ultra-intense lasers". G. E. Cochran, P. L. Poole, D. W. Schumacher, *Stewardship Science Academic Programs Symposium*, Bethesda, MD (2016).

"Modeling liquid crystal plasma mirrors using PIC simulations". G. E. Cochran, *Ohio Supercomputer Center Statewide Users Group Meeting*, Columbus, OH (2015).

"Liquid crystal film development for plasma mirrors and waveplates". G. E. Cochran, P. L. Poole, C. Willis, R. J. Hanna, K. Pytel, K. S. Sullivan, C. D. Andereck, D. W. Schumacher, *Division of Plasma Physics Annual Meeting*, Savannah, GA (2015).

"Timestep criterion for PIC simulation of relativistic electron acceleration in a high-intensity laser field". Ginevra Cochran, Alexey V. Arefiev, Douglass W. Schumacher, Kasandara S. Sullivan, Alexander P. L. Robinson, *Inertial Fusion Sciences and Applications Meeting*, Seattle, WA (2015).

"1 Hz planar target formation by spinning disk inserter with variable thickness liquid crystal films". G. E. Cochran, P. L. Poole, C. Willis, R. J. Hanna, K. Pytel, C. D. Andereck, D. W. Schumacher, *National Ignition Facility/Jupiter Laser Facility Users Meeting*, 3^{rd} place graduate student poster, Livermore, CA (2015).

"Convergence criteria for PIC simulations of electrons in an ultraintense laser field". Ginevra E. Cochran, Alexey V. Arefiev, Douglass W. Schumacher, A. P. L. Robinson, Guangye Chen, *Ohio Supercomputer Center Statewide Users Group Meeting*, 2^{nd} place flash talk, Columbus, OH (2014).

"Intensity-dependent criteria for PIC simulations of relativistic electrons in a laser field". Ginevra E. Cochran, Alexey V. Arefiev, Douglass W. Schumacher, A.P.L. Robinson, Guangye Chen, *Division of Plasma Physics Annual Meeting*, New Orleans, LA (2014).

"Temporal resolution criterion for PIC simulations of relativistic electron dynamics in an ultra-intense laser field". Ginevra E. Cochran, Alexey V. Arefiev, Douglass W. Schumacher, A.P.L. Robinson, Guangye Chen, *High Power Laser Workshop*, Palo Alto, CA (2014).

"Intensity-Dependent Convergence Criteria for PIC Simulations of the Laser Acceleration of Free Electrons". Ginevra E. Cochran, Alexey V. Arefiev, Douglass W. Schumacher, *Omega Laser Facility Users Group Workshop*, Rochester, NY (2014).

Fields of Study

Major Field: Physics

Table of Contents

List of Figures

Figure **Page**

List of Tables

Chapter 1
Introduction

1.1 High Energy Density Physics

The field of high energy density physics (HEDP) studies systems with energy densities above 10^{11} J/m^3, or equivalently, pressures in excess of 1 Mbar. These conditions occur naturally in giant planet and solar interiors and during fuel compression in fusion, but have only been able to be formed and characterized in a controlled laboratory setting within the last few decades. High-intensity lasers play a key role in creating and probing HEDP conditions. Laser generated HEDP systems are interesting to study from a fundamental physics perspective, and are also sources of secondary radiation which are of interest for a number of applications. Selection of various laser and target parameters can cause transfer of laser energy into electron beams [25], x-rays or neutron beams for radiography or remote detection applications [26, 27], positron-electron plasmas for fundamental studies related to astrophysical environments [28], and ion beams, which relate to radiography [29], generation of warm dense matter [30], and, possibly, cancer therapy [31, 32, 33, 34].

The intense laser-matter interaction begins with propagation of the laser to the target, typically though some amount of blow-off plasma, and transfer of energy to the electrons. The blow-off plasma is often due to noise or non-ideal light that precedes the laser pulse itself, termed pre-pulse, in which case the plasma is called pre-plasma. There is dramatic variation in the laser propagation and electron heating depending on the intensity, pulse width, and degree of pre-pulse present. Regimes can be defined based on, whether the intensity is nonrelativistic or relativistic, the pulse duration is on a nanosecond, picosecond,

or femtosecond scale, and whether the pre-plasma spatial scale is small or large compared to a wavelength. The next chapter will define some basic scale parameters but the dimensionless field amplitude, $a_0 = eE_0/m\omega c = 1$ (intensity $I \approx 10^{18}$ W/cm^2 for 1 μm wavelength light), is usually taken to define the boundary between a non-relativistic interaction and a relativistic one. For optical or near-infrared light, intensities below this will have electron heating mechanisms dominated by collisions [35]. For intensities above this, in addition to a relativistic treatment being required as the electron spends an increasing fraction of its oscillation cycle near the speed of light, the cross-section for electron collisions drops and other mechanisms must provide the dephasing necessary for electron heating. If the pre-plasma scale length is large, significant propagation effects occur such as self-focusing and phase modulation, due to laser modification of the index of refraction [36, 37]. In turn, the laser modifies the density and temperature profile of the plasma itself as gradients in the laser electromagnetic field push plasma particles [38, 39]. The plasma-modified laser and the laser-modified plasma continue to interact until the laser is either absorbed or reflected. There are many absorption mechanisms (collisions, vacuum heating, resonance absorption and J×B heating) that assume different relative roles that vary with intensity, density, and the density gradient [40, 41, 42, 43]. Most absorption processes are angle dependent as well and, due to laser modification of the critical surface, the region of sufficient density such that the pulse is reflected, the laser electric field will intersect the critical surface at a range of angles. The resulting distribution of hot electrons plays a key role in the generation of other types of secondary radiation (eg. ions [44], neutrons, x-rays, gamma rays, and even anti-matter). The foregoing does not exhaust the list of processes that can contribute, of course, with multiple nonlinear processes, instabilities, and other effects that can play a role present such as stimulated Raman scattering (SRS) [45], the Weibel instability [46], or magnetic field generation via the Biermann Battery mechanism [47]. Despite the complexity of the intense laser plasma interaction (LPI), it is often the case that a small number of processes will dominate a given effect of interest allowing a "story" to be told – this is part of the attraction of this field. An example of this will be given in the study of ion acceleration described in this thesis.

Although petawatt class lasers became available in the early 1990s with the Nova laser [48] at the Lawrence Livermore National Laboratory, and the intense-laser matter interaction has been explored for decades, the number of contributing processes and the variation in their behavior and interplay with different intensities, wavelengths, pulse properties, and the choice of target (eg. gas, liquid, solid, choice of material, geometry) has kept this area fresh and exciting. It is necessary, however, to limit the parameter phase space to keep any given research effort tractable. This thesis focuses on the LPI when peak intensities are relativistic (up to 10^{21} W/cm^2), the pulse durations are ultrashort (down to 30 fs), and the pre-plasma scale length is short (much less than a wavelength). The short pulse duration restricts hydrodynamic expansion during the pulse, although at these intensities significant deformation of the target can occur anyway. The short pre-pulse scale length preserves a well-defined vacuum/target interface as much as possible by the time the pulse reaches the target surface. This thesis addresses issues such as the requirements to model processes under these conditions, the development of technology to perform such experiments, and a combined experimental/computational study of ion acceleration. Energetic ions are one of the most useful types of secondary radiation to come from the relativistic LPI, and two applications which rely on them will be discussed in the following sections.

1.2 Ion Beam Applications

1.2.1 Ion Cancer Therapy

Ions are advantageous in delivering carefully targeted radiation doses to a tumor without adversely affecting surrounding healthy tissue. An x-ray deposits the majority of its energy as it passes through tissue on the way to its target, while an ion slowly loses energy until it comes to a sudden stop as its cross section increases and deposits its remaining energy (the Bragg peak). The advantage of this is shown in Fig. 1.1, which compares the decrease in healthy tissue irradiated in the frontal lobe of the brain by using protons instead of photons for treatment. Existing large-scale accelerators, such as synchrotrons and cyclotrons, are already capable of treating patients using this method, but are expensive and require a

great deal of space. Laser-based proton acceleration has the potential to be a lower-cost alternative to this type of facility.

A short pulse laser (< 1 ps) with a peak intensity $I > 10^{18}$ W/cm^2 which irradiates a μm scale solid target can accelerate protons and heavier ions to energies of tens of MeV/nucleon. An effective laser-based ion cancer therapy source will require up to $\sim$ 200 MeV protons in order to reach sufficient depths to treat all tumors – efforts toward this application are focused on improving peak ion energy, as well as control of ion beam spectrum, particle flux, directionality and angular spread. Finally, increasing the repetition rate of both laser and target is of interest, both to increase the average delivered dose and allow more study of the underlying ion acceleration mechanisms. An example of such a study enabled by high repetition rate technology will be presented in Chapters 7 and 8.

1.2.2 Neutron Radiography

Neutrons have a number of radiographic uses due to their propensity to scattering from low Z materials. An example of this is given in Fig. 1.2 - an analog camera's film is visible in a neutron radiograph, while it is largely obscured in a x-ray of the same object. A neutron's low mass allows it to travel through metals almost unimpeded, allowing it to travel where an x-ray cannot. Non-destructive evaluation (NDE) using neutrons can be used to detect fissile materials, find inner defects in airplane parts, and determine composition of fragile archaeological samples [49]. As is the case with ion cancer therapy, these studies are possible using existing large-scale accelerators, but these could be complemented by laser-based sources.

Protons and deuterons produced via short pulse lasers can also be used to create neutron beams [50, 51]. Ions produced at a primary "pitcher" target interact with a secondary "catcher" converter target and produce neutrons, mostly commonly through p-Li, d-d, or d-Li reactions. Alternate promising schemes involve laser-irradiated CD_2 nanowire arrays which have recently shown a 500$\times$ increase in d-d neutrons over flat targets [52], as well as deuterated clusters [53] and cryogenic deuterium [54]. The energy content, directionality, number of neutrons, and shot rate are also parameters of interest here, with the added loss

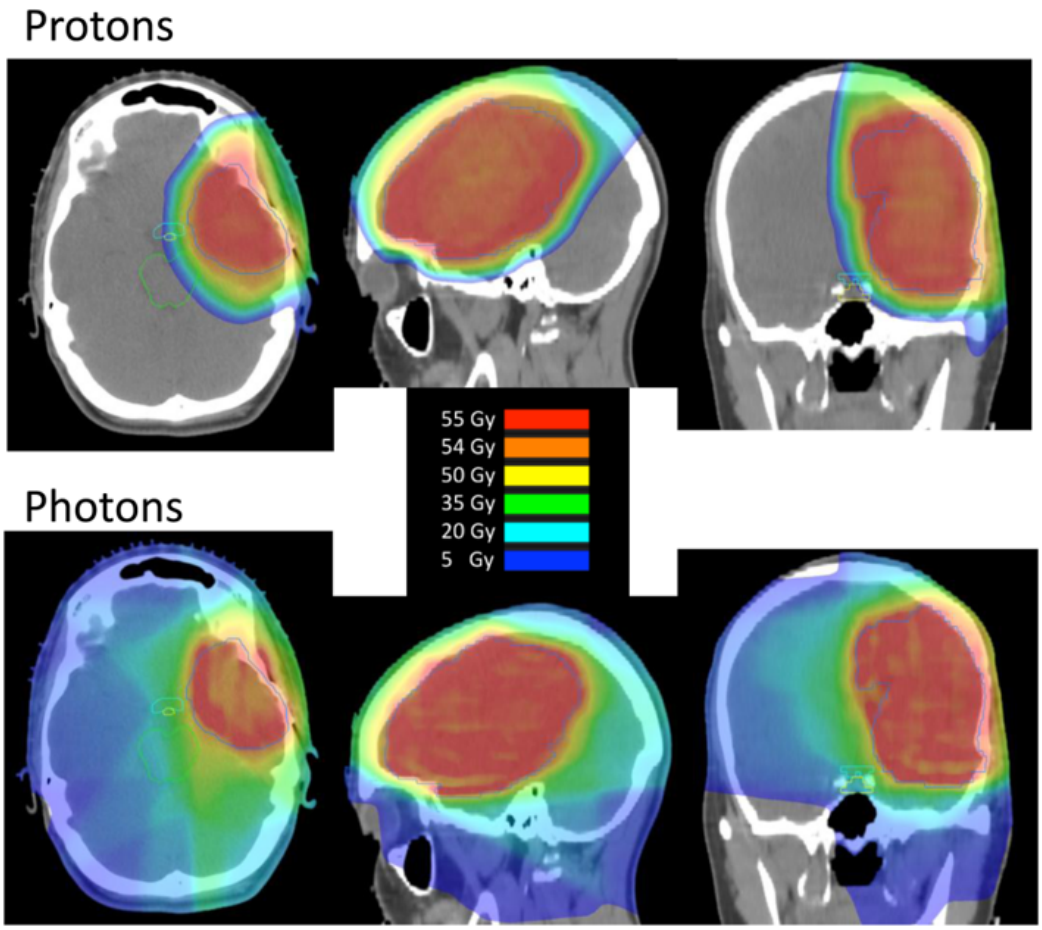

Figure 1.1: Above: amount of dose in Gy deposited in proposed proton treatment of brain tumor in the frontal lobe, as viewed from above (left), side (middle), and back (right). Below: Photon-based treatment scheme reaching the same peak irradiation (same three views). Much more surrounding tissue receives unnecessary dose. Figure reprinted from [1].

in efficiency of a converter target.

1.3 This Work

In the ultrathin target regime, controlling the laser pre-pulse is key to optimizing acceleration mechanisms which can serve as sources for secondary radiation. This thesis presents the development of new simulations which dynamically model how this is done with plasma mirrors allows the study of how the beam's characteristics are altered. Determining the underlying acceleration mechanism responsible can be difficult; an experiment in which this was the case will be discussed, as well as the simulations which were necessary to explain it.

This thesis is arranged as follows:

- Chapter 2 summarizes important aspects of plasma physics to orient the reader. Theory related to specific simulation or experimental efforts will be presented in the appropriate chapters.
- Chapter 3 gives an introduction to the particle-in-cell (PIC) numerical simulation technique, focusing on how the method's computational advantage is achieved and the resulting resolution requirements.
- Chapter 4 presents a new error analysis of the Boris particle pusher used in many PIC codes, using the simple problem of an electron accelerated in a plane wave. An intensity-dependent timestep criterion for mitigating the problems found is derived.
- Chapter 5 describes freestanding liquid crystal films and film formation devices used in Chapters 6-8, and briefly describes future applications.
- Chapter 6 presents a novel PIC framework for dynamically modeling the behavior of dielectric plasma mirrors with varying laser intensity, focusing on dimensionality and ionization and collisional models.
- Chapter 7 summarizes the results of a short-pulse ion laser acceleration experimenty performed at the DRACO facility using liquid crystal targets.

Figure 1.2: Top: neutron radiograph of an analog camera. Film can be seen to the left and right of the lens. Bottom: the same camera imaged with x-rays. Figure from [2].

- Chapter 8 studies the dynamics of the results from the DRACO experiment using a series of 3D PIC simulations, with emphasis on identifying primary acceleration mechanisms as a function of target thickness.
- Chapter 9 will conclude with a brief summary of this work.

Chapter 2
A Brief Overview Of Relevant Plasma Concepts

This chapter provides a brief introduction to basic plasma concepts relevant to this thesis as well as a few figures of merit to give the reader a sense of scale. More in depth aspects of theory will be discussed in the context of the appropriate chapters. SI is used unless indicated otherwise.

2.1 Plasma Definitions

Plasma abhors a charge imbalance. A charge q introduced in an otherwise neutral plasma will cause the surrounding electrons and ions to rearrange themselves, acting to screen it. Assuming the electron density can be described as a Boltzmann distribution, $n_e = n_o \exp(e\phi/kT)$, the modified potential due to the introduction of this charge can be described as

$$-\nabla^2\phi = \frac{\rho}{\epsilon_0} = \frac{n_o e}{\epsilon_0}\left(1 - \exp(e\phi/k_B T)\right) + \frac{q}{\epsilon_0}\delta(r), \tag{2.1}$$

where ϕ is the electric potential, $e = 1.6 \times 10^{-19}$ C, ϵ_0 is the vacuum permittivity, k_B is the Boltzmann constant, and T is the electron temperature. If $e\phi \ll k_B T$, $\exp(e\phi/k_B T)$ can be approximated as $1 + e\phi/k_B T$, and we can then write

$$-\frac{1}{r}\frac{d^2}{dr^2}(r\phi) = \frac{n_0 e}{\epsilon_0}\left(\frac{-e\phi}{k_B T}\right) + \frac{q}{e_0}\delta(r). \tag{2.2}$$

Outside of $r = 0$, this can be written as

$$\frac{d^2}{dr^2}(r\phi) = \frac{n_0 e^2}{\epsilon_0 k_B T}(r\phi), \tag{2.3}$$

which has a solution of the form

$$\phi = \phi_0 \exp(-r/\lambda_D), \tag{2.4}$$

so λ_D, the Debye length, is the characteristic length over which the potential from the introduced charge drops off:

$$\lambda_D = \sqrt{\frac{\epsilon_0 k_B T}{e^2 n_0}}. \tag{2.5}$$

The degree to which this approximation is valid depends on how many particles are contained within this characteristic distance; we write the number of particles in the Debye sphere $N_D = 4/3\pi\lambda_D^3$, and say if it is much greater than 1, Debye theory is a good description.

Electrons displaced from their equilibrium position and released will oscillate – since ions are much more massive than electrons, they can be taken as immobile to first order. If a long patch of electrons is displaced from the ion background by a distance x, resembling a parallel plate capacitor, an electric field is set up between the exposed charged sections $E_x = \sigma/\epsilon_0$, where $\sigma = n_e e x$, and n_e is the electron density. Electrons within the slab then experience a restoring force $F = -n_e e^2 x/\epsilon_0 = m_e \ddot{x}$. Assuming a harmonic response $x(t) = x_0 \cos\omega_p t$, one can then write $\omega_p^2 x = n_e e^2 x/(m_e \epsilon_0)$, or

$$\omega_p = \sqrt{\frac{n_e e^2}{m_e \epsilon_0}}. \tag{2.6}$$

A laser incident on a plasma of increasing density will transmit through until the density dependent ω_p is equal to the laser frequency $\omega_L = 2\pi c/\lambda_L$. The electron density at which this occurs is the critical density, which can be expressed as

$$n_c = \frac{\omega_L^2 m_e \epsilon_0}{e^2} \tag{2.7}$$

For a 1 μm laser, $n_c = 1.1 \times 10^{21}/\text{cm}^3$. Solids typically have 100-200 times this density. As an example, solid aluminum, which has 3 conduction electrons and $\rho = 2.7$ g/cm^3, $n_e \simeq 160 n_c$ ($\lambda = 1$ μm). Many experiments take advantage of the fact that the critical density increases with decreased wavelength, using short wavelength optical light or x-rays to probe plasmas that are opaque in the infrared.

The laser cannot propagate past the position at which $n_e = n_c$, but its field does extend a short distance past this point, decaying in an evanescent wave. This is the skin depth, which can be written as $\delta_s \sim c/\omega_p$.

2.2 Laser Definitions

The phenomena described in this thesis depend strongly on the intensity of the laser. In addition to the intensity, it is equally common to characterize the laser by the dimensionless vector potential

$$a_0 = \frac{eE_0}{m_e \omega_L c} \tag{2.8}$$

where E_0 is the peak electric field of the laser. For non-relativistic laser intensities ($a_0 < 1$), the electron oscillates in the electric field with a time-averaged energy

$$\Phi = \frac{e^2 E_0^2}{4 m_e \omega_L^2} \tag{2.9}$$

often called the ponderomotive potential. Although this can be derived from the time-averaged kinetic energy of a charge in the field, it behaves like the potential energy of a repulsive force thus, for example, an otherwise free electron near the center of an intense laser beam will experience a time-average force pushing it away from the region of highest intensity.

If $a_0 > 1$, which occurs at 1.38 $\times 10^{18}$ W/cm^2 for 1 μm light, the magnetic component of the Lorentz force law becomes non-negligible. Above this intensity, electrons do not just oscillate transversely in its electric field, but are driven forward with the laser, reaching substantial energies which they can keep if they separate from the laser at the right time.

Their Lorentz gamma factor can be estimated to be the average gamma factor due to the laser,

$$\langle \gamma_L \rangle = \sqrt{1 + a_0^2/2} \tag{2.10}$$

for a linearly polarized laser.

Chapters 7 and 8 are concerned with the problem of an ultrashort (< 30 fs) intense laser interacting with a target which can initially be described as a density step function. The evolution of this interface, the laser plasma interaction (LPI) is complex, as it involves a large range of temperatures and densities, and hence physical regimes. As the laser heats plasma at the front of the target, it will begin to expand, forming a profile that can sometimes be approximated by the form

$$n_e(x) = n_0 e^{-x/L} \tag{2.11}$$

The Debye length and plasma frequency define fundamental length and time scales for a plasma. The laser wavelength, period and the collionless skin depth define additional scales for the interaction with light. In a case where the leading edge of a laser pulse (or the noise light that often precedes the pulse) establishes a density profile like that of Eq. 2.11, the Debye length and plasma frequency will vary over many orders of magnitude over a small multiple of L, a distance which, in turn, may be small or large compared to a wavelength. Both cases are commonly encountered in practice and in the literature [55], and require different treatments. The relative sizes of these scale lengths and times establish the physical regime in which an experiment occurs. For example, the heating mechanisms by which the laser transfers energy to the electronic system vary depending on the intensity of the light and the sharpness of the interface, specified by L. Relativistic intensities tend to be non-collisional, for example, but sharp interfaces provide an additional mechanism for dephasing of the electrons with the light, Brunel heating [41]. Here, electrons can escape the laser field by moving into the plasma if its density exceeds the critical density. Of considerable importance to this work, the strategies for designing a numerical model are

dictated in part by these scale lengths and times. For example, even if the Debye length does not need to be resolved for the physical processes of interest, it may still need to be resolved for numerical stability, as discussed in Chapter 3.

Chapter 3
The Particle-In-Cell Method

3.1 Why and When to Use Particle-In-Cell

High density plasmas pose a challenge for theory. In the context of this work, they generally involve a large range of conditions from solid density to well below critical density, and from room temperature to temperatures greatly exceeding that of the surface of the sun. A large number of processes can occur simultaneously in these interactions – laser self-focusing and filamentation in preplasma, laser absorption in preplasma, and hot electron generation at the target critical surface or front surface, to name a few. The data obtained from an HEDP experiment is often not always straightforward to interpret, as diagnostics are generally time-integrated and cannot directly give insight into dynamic processes. For these reasons, simulations are needed to interpret experimental results and identify the underlying physics. Two main categories of code for modeling HEDP plasmas are fluidic and kinetic.

Fluid codes assume the plasma is in local thermal equilibrium and that the particle distribution function can be described with a Maxwell-Boltzmann distribution. Macroscopic state variables, such as temperature, pressure and density of each species (such as electrons or protons), can be used to describe the plasma state and its evolution. However, there are many areas of interest in HEDP that fluid codes cannot treat, for example ultrashort pulse laser interactions where plasmas do not have sufficient time to equilibrate, and where relativistic particles are present. In these cases, kinetic modeling is the better-suited approach, which treats the interactions between individual electrons and ions. The principal difficulty in kinetic modeling is the sheer number of calculations involved which, for pair-

wise interactions for example, scales as the square of the number of particles, N^2. Consider a singly-ionized carbon plasma at solid density, there are a total of 2×10^{23} particles/cm^3 including electrons and ions. For a cubical volume 40 μm on a side, this amounts to $\sim 10^{16}$ particles, and $\sim 10^{32}$ calculations between them. Assuming one calculation per computer clock cycle, a 3.0 gigahertz processor would take 10^{12} years to complete these once. Particle-in-cell (PIC) modeling, one example of a kinetic method, cleverly reduces the number of calculations required, and will be described in the following sections. The PIC method was first developed in the early 1960s, arguably starting with the work of Buneman and Dawson [56]. Early work introduced a grid and finite differencing, developed fast algorithms suitable for the computers of those times, and explored the consequences of the approximations introduced. PIC has become a mainstay of the plasma physics community and the development effort is, if anything, even more active today. PIC simulations play a prominent role in the results described in this work and, accordingly, a brief discussion of the PIC method is provided in this chapter.

3.2 The Grid and Macroparticles

Circumventing calculating pair-wise interactions is key to modeling a large number of particles kinetically and, for fully electromagnetic simulations, is desirable in any case. In Fig. 3.1, an example of the PIC grid is shown. Particles (red), exist in continuous space, but space itself is divided into cells. Instead of calculating force interactions between each red particle, the charge and current associated with each is assigned to a node (blue). The exact manner in which this is done is referred to as the particle shape, discussed in Sec. 3.4. At each node, the total charge and current assigned from surrounding particles are used to solve Maxwell's equations and obtain new electric and magnetic fields. While the number of force calculations between particles goes as particle number squared N^2, the PIC method allows evolution of the system for, of order, $N + M$ calculations, where M is the number of nodes. The resulting increase in speed is dramatic.

It is worth noting that the current and charge play different roles depending on the

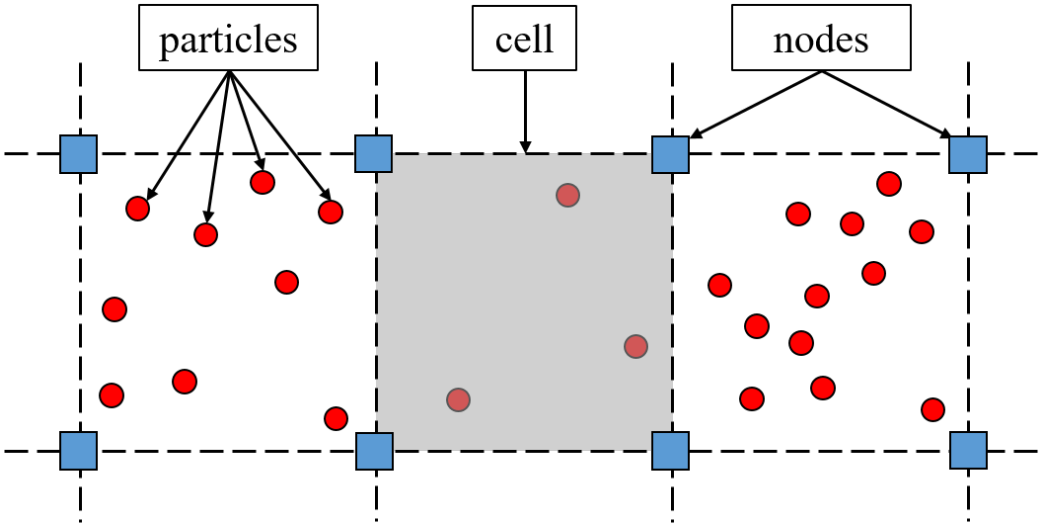

Figure 3.1: Example of a two-dimensional particle-in-cell grid. Space is discretized into cells (one is in gray), which contain particles (red circles). Nodes (blue squares), the cell vertices, are where fields are calculated. The nodal distribution is usually more complicated than this [3], but this is illustrative.

nature of the simulation and, for some types of simulation, both may not even be needed. For the work described here, the current is used to advance the fields in time while the charge is used for error correction and specialized physics models. This is a common arrangement and, for simplicity of discussion, it is assumed this is the mode of operation. Likewise, there are many variations in implementation, for example, in approximating the differential equations with difference equations. The methods described below are sometimes simplified, but illustrative, versions of the approaches used in this work.

Conveying information between particles and nodes for, say, 10^{16} particles is still a prohibitively expensive operation. To model a relatively large volume, PIC employs a "macroparticle", which represents many particles of a single species (electrons, for example). This macroparticle has the same charge to mass ratio as the particle it represents, and so will be affected in the same way by the Lorentz force law. PIC simulations of the kind discussed in Ch. 8 can have $\sim 10^8$ macroparticles representing electrons; in the case of the plasma in Sec. 3.1, each macro-electron would represent $\sim 6 \times 10^7$ real electrons. There are many PIC codes in use in HEDP with different capabilities; the work described in this

thesis was conducted using the Large Scale Plasma code (LSP) [57].

3.3 The PIC Cycle

3.3.1 Overview

With particle evolution and field evolution occurring at different locations, in general, some method must be chosen to connect the two. In a PIC code, as shown in Fig. 3.2, the following operations take place within a single timestep Δt:

1. Particle velocities and positions are updated using forces calculated at their positions.

2. Particle charge and current information is assigned to nearby nodes according to particle shape. Some frequently used particle weighting functions will be discussed in Sec. 3.4.

3. Node currents are used to update electric and magnetic fields via Maxwell curl equations. Node charges are used for error correction and other models.

4. Fields at nodes are interpolated back to particle positions in preparation for the next particle advance.

3.3.2 Leapfrog Integration

In LSP, the particle equations of motion and Faraday's and Ampere's law are integrated as central-difference formulas, using the leapfrog method. Updating the electric field E at a cell to E_{new} as in Fig. 3.3 requires E_{old} and B_{new}; offsetting the evaluation of B with respect to E provides a more current value for updating E. Leapfrog is used because the error of this method goes as $(\Delta t)^2$, while the error forward-centered formula where E and B are located on the same time grid only goes as Δt. Both the field solve and particle advance are staggered in this way, with x and E evaluated on one time grid and v and B on the other. The specific particle advance used in LSP and many other codes is discussed in the next section. It should be noted that all methods described in this chapter are fully

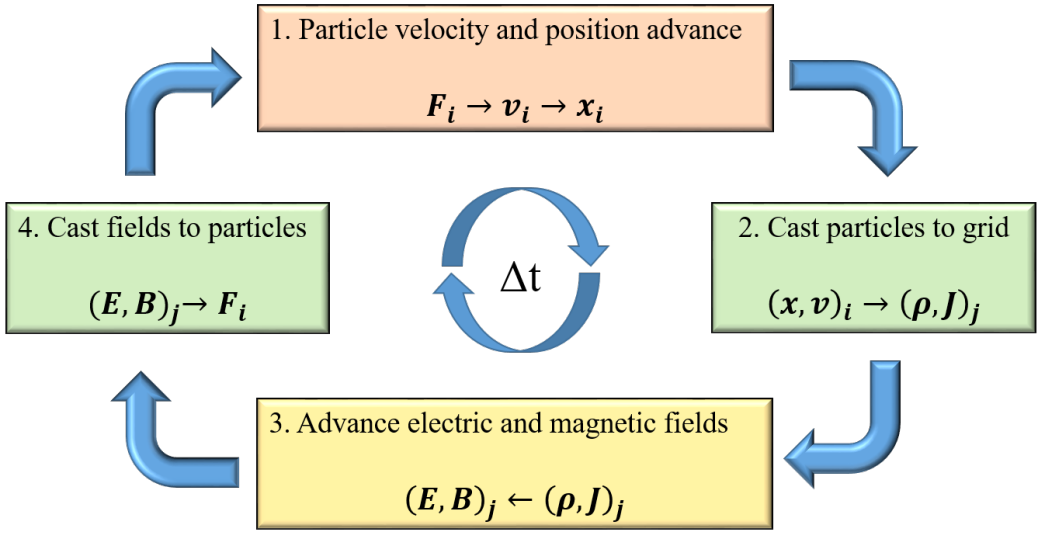

Figure 3.2: The PIC cycle over one timestep. Adapted from [4]. The "i" refers to a particle and the "j" to a node.

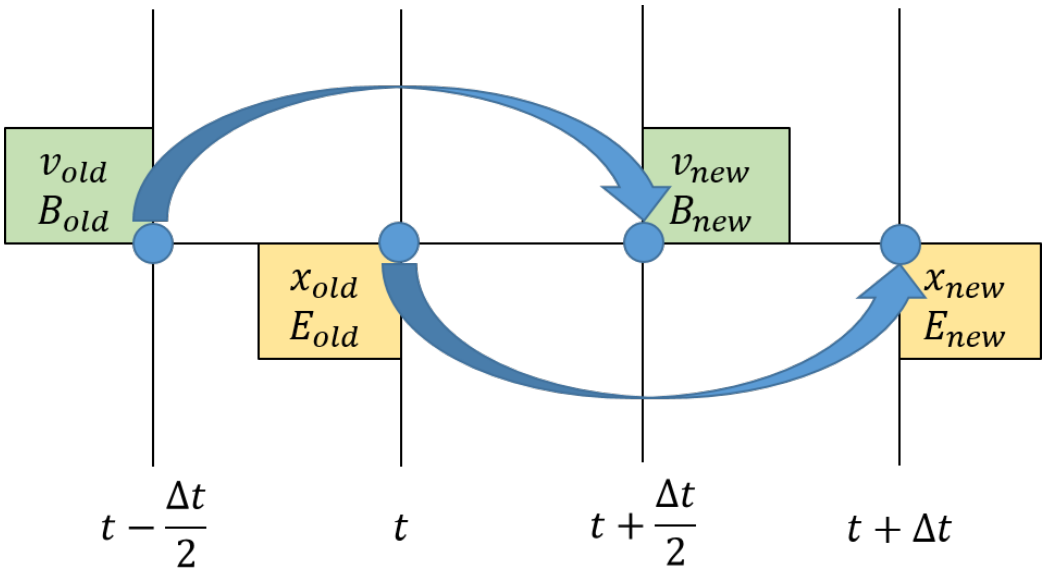

Figure 3.3: Cartoon illustrating leapfrog integration. Particle velocities (magnetic fields) are advanced on odd half-integer timesteps, while particle positions (electric fields) are advanced on even half-integer timesteps. Adapted from [4].

explicit, i.e. rely only on prior timesteps to advance quantities. Implicit integration, which also uses the value at the current timestep, is included in LSP in a prediction-correction form and used for the simulations in Ch. 8. Implicit simulations can be more forgiving of some of the resolution restriction to which explicit PIC is bound, at the cost of increased computation and possibly some numerical artifacts. A detailed treatment of this method can be found in Ref. [58].

3.3.3 The Boris Pusher

In the Boris pusher [59], a particle with charge q and mass m has its momentum advanced by $\Delta\vec{p}/\Delta t = q\left(\vec{E} + \vec{v}\times\vec{B}\right)$, which is split into three steps. Here, it is written in terms of $\vec{u} \equiv \gamma\vec{v}$.

1. A half acceleration using the electric field:

$$\vec{u}_- = \vec{u}_{t-\Delta t/2} + \frac{1}{2}\frac{q\Delta t\vec{E}_t}{m}. \tag{3.1}$$

2. A full rotation using the magnetic field:

$$\begin{aligned} \vec{u}' &= \vec{u}_- + \vec{u}_- \times \vec{t}_t, \\ \vec{u}_+ &= \vec{u}_- + \vec{u}' \times \frac{2\vec{t}_t}{1+t_t^2}, \\ \vec{t}_t &= \hat{B}\tan\left(\frac{q\Delta t}{2m\gamma_t}B_t\right). \end{aligned} \tag{3.2}$$

   This is equivalent to a rotation of the momentum vector by $\theta = qB_t\Delta t/m$ – at relativistic intensities, this has implications which will be discussed in Ch. 4.

3. A second half acceleration using the electric field:

$$\vec{u}_{t+\Delta t/2} = \vec{u}_+ + \frac{1}{2}\frac{q\Delta t\vec{E}_t}{m}. \tag{3.3}$$

Once new momenta have been obtained at $t + \Delta t/2$, $\gamma_{t+\Delta t/2}$ is calculated, and particle

positions are advanced:

$$\begin{aligned} \gamma_{t+\Delta t/2} &= \sqrt{1+(u_{t+\Delta t/2}/c)^2}, \\ \vec{x}_{n+1} &= \vec{x}_n + \frac{\vec{u}_{t+\Delta t/2}\Delta t}{\gamma_{t+\Delta t/2}}. \end{aligned} \tag{3.4}$$

3.4 Particle Weighting

To carry out the field solves and particle advances described in Sec. 3.3, the particle charge and current quantities must be assigned to nodes, and the updated fields interpolated back to particle positions to determine forces. This process is defined by the particle's weighting function, which determines how many nodes each particle contributes to and in what amount. These interpolative steps should use the same particle shape in each direction to avoid a particle exerting a spurious force on itself [4]. Two particle weighting functions, nearest-grid-point (NGP) and cloud-in-cell (CIC), are shown in Fig. 3.4.

The NGP particle weighting function is the simplest method (and is rarely used) – the charge and current from particle x_i are all assigned to the nearest node X_j (Fig. 3.4(a)). This results in a rectangular grid density of width equal to the cell size, Δx, on the grid, which while computationally efficient, generates noisy density and electric field distributions because of the sudden changes as a particle leaves one cell and enters another.

In CIC weighting, used in this work, the particle's weighting function is considered to be a uniformly charged cloud of width Δx; the particle charge is assigned to neighboring nodes X_j and X_{j+1} (Fig. 3.4(b)) as follows:

$$Q_j = q_i\left(\frac{X_{j+1}-x_i}{\Delta x}\right), Q_{j+1} = q_i\left(\frac{x_i - X_j}{\Delta x}\right). \tag{3.5}$$

The grid density in CIC is a triangle of width $2\Delta x$, which transitions in and out of cells more smoothly, resulting in less noisy plasma densities and fields. The currents are weighted similarly to the charges. It is common for higher order particle weighting functions than these to be used [60], at the cost of increased computation but with less noise and better resistance to some instabilities.

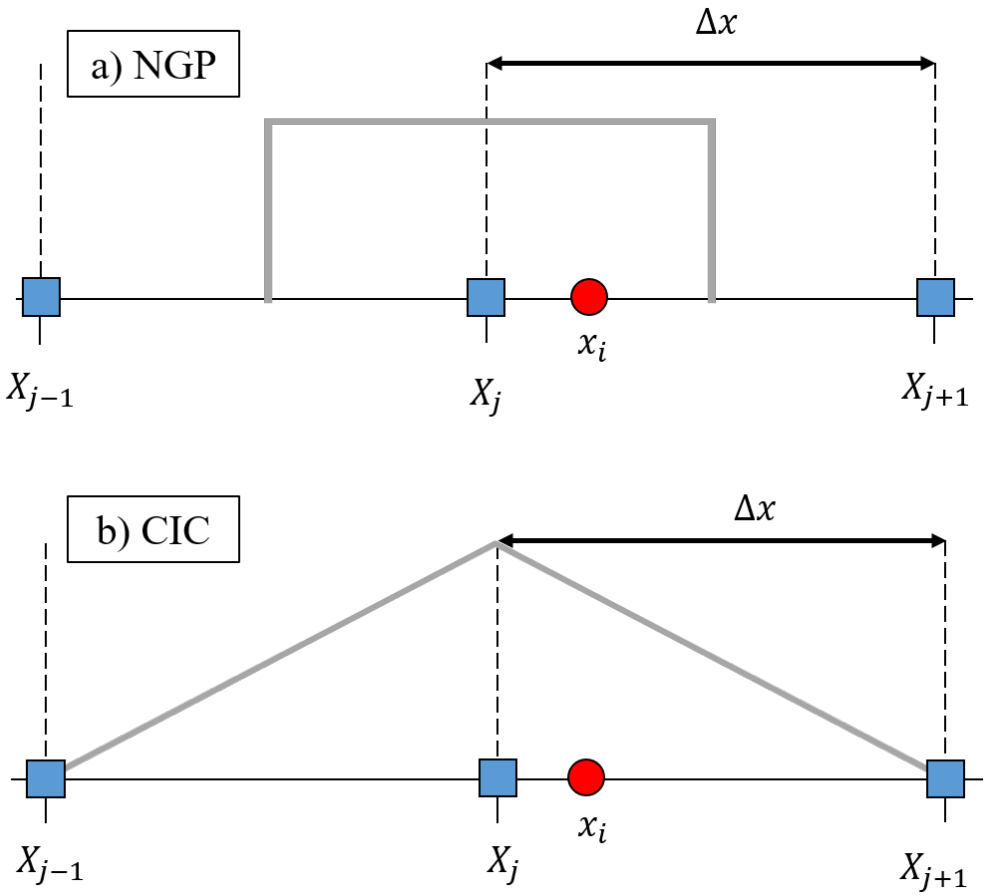

Figure 3.4: Examples of (a) nearest grid point (NGP) and (b) cloud-in-cell (CIC) particle weighting functions. NGP assigns all quantities from x_i to the nearest node (X_{j-1}). CIC splits the particle's weight between its two nearest neighbors proportionately to their distance from it. Gray outlines indicate the grid density at the particle position produced by these particle shapes. Adapted from [4].

3.5 Resolution and Dimensionality Considerations

There are a number of restrictions on the minimum size of a cell or time step; which of these is the most stringent depends on the specifics of the problem. For an underdense, high temperature plasma, the laser period may determine the required timestep. A high density cold plasma is more likely to be defined by the timestep required to resolve the plasma frequency. In explicit PIC, a few conditions are required for simulation stability - two are listed briefly below.

3.5.1 The Courant-Friedrichs-Lewy Condition and Debye Heating

Discretizing Maxwell's equations leads to a restriction on timestep and cell size to ensure light cannot cross more than one cell in one timestep, known as the Courant-Friedrichs-Lewy condition [61] (commonly Courant condition):

$$\left(\frac{1}{c\Delta t}\right)^2 \geq \left(\frac{1}{\Delta x}\right)^2 + \left(\frac{1}{\Delta y}\right)^2 + \left(\frac{1}{\Delta z}\right)^2. \tag{3.6}$$

This simplifies to $c\Delta t \leq \Delta x$ for a 1-D problem. Where a simulation operates with respect to this limit is given as $R = c\Delta t/\Delta x$, the Courant ratio.

The Debye length which characterizes a plasma can lead to an unstable simulation if not resolved, with the plasma temperature increasing nonphysically until the Debye length is resolved by the chosen cell size. For very cold dense plasmas, λ_D can be less than a nanometer, and resolving it is often not computationally possible. There are a few tactics for avoiding or mitigating this problem currently in use in ion acceleration literature – curtailing the simulation duration to keep it under the instability's growth time, artificially raising the plasma temperature and/or lowering plasma density at the simulation initialization, or employing an implicit model, which is more resistant to the instability. A more detailed discussion can be found in [62].

3.5.2 Simulation Dimensionality

Since the size of a simulation and minimum cell size are often set by the problem being considered, the number of simulation dimensions in which a particle can move is often reduced to conserve computational power, or simply make the simulation possible. However, only the spatial extent is reduced in dimensionality in PIC. Vector quantities retain all 3 components. For example, a particle may only be allowed to move in one dimension, but its velocities are always accounted in 3 dimensions - this is notated as 1D3V. Electric and magnetic fields are always computed in all three dimensions, but the dimensionality of the simulation affects the falloff of the fields – for example, particles in a 2D3V simulation effectively take the shape of line charges, and so the field due to such a particle goes as $1/r$ as opposed to $1/r^2$. A problem whose geometry naturally produces fields with this dependence can be well modeled in 2D3V; a plasma which is blown out hemispherically may not. Since particle movement is restricted in reduced dimensionalities, effects which depend on target expansion are underestimated in 1D3V and 2D3V.

Chapter 4

High Intensity Temporal Resolution Criterion For Relativistic Electron Motion

4.1 Introduction

[1] Ongoing progress in laser engineering has significantly increased the maximum laser intensity available for ultra-intense laser-plasma experiments. A number of emerging applications now rely on the ability of high intensity laser beams to accelerate electrons to relativistic energies that considerably exceed the electron rest mass [63, 64, 65]. It has therefore become critical to accurately simulate electron dynamics in an ultra-intense electromagnetic field. However, it is not always possible to determine whether the simulation has been done with required accuracy and whether the simulation results are physically correct without performing a convergence study. Such a study can be a time-consuming effort without guarantee of a conclusive outcome if the parameter space has not been narrowed down sufficiently using relevant test cases. Convergence studies are best performed based on a fundamental understanding of the numerical and physical constraints on simulation parameters.

A commonly used tool for simulating laser-plasma interactions is the particle-in-cell (PIC) code. As described in the previous chapter, it consists of two key blocks: a wave solver on a given spatial grid and a particle pusher that uses the calculated fields to ad-

[1] Much of this chapter is reprinted with permission from Alexey V. Arefiev, Ginevra E. Cochran, Douglass W. Schumacher, Alexander P. L. Robinson, and Guangye Chen, Physics of Plasmas, vol.22, 013103 (2015). Copyright 2015, American Institute of Physics [5].

vance particles. Two key parameters, besides the number of particles, which determine the accuracy and speed of a simulation are the cell size and the timestep. The choice of the two is interrelated through the Courant criterion [4], which limits the maximum timestep for a given cell size, particularly for explicit codes. Depending on the problem, different criteria are used to determine the cell size and the timestep.

Here, we are particularly interested in the regime where the plasma density is significantly below the critical density [66, 67, 68] or, equivalently, where the laser frequency is significantly above the plasma frequency. This is, in some ways, a simpler and more fundamental regime than that of the higher density plasmas considered in the following chapters. In this regime, the group and phase velocities of an electromagnetic laser pulse inside the plasma are close to the speed of light, which enables electron acceleration to high energies as the electron moves forward with the pulse via direct laser acceleration. For this type of problem, one typically determines the spatial resolution first based on the wavelength of the laser pulse and its transverse dimensions. The timestep is then determined using the Courant criterion, so that the numerical scheme remains stable. It is usually chosen close to its maximum value allowed by the Courant criterion in order to reduce the numerical dispersion of the wave caused by the grid [4]. However, we find that at sufficiently high intensities in a low density environment, the wavelength does not set the scale for accurate treatment of electron motion. Instead, the electron motion near its stopping points becomes the critical factor resulting in surprisingly stringent requirements for convergence. Given the current widespread use of a large number of differing PIC codes, often incorporating multiple algorithms, simple test cases and criteria for evaluating them are highly beneficial. In particular, since experiments employing intensities of up to $10^{21}\mathrm{W/cm}^2$ [69] are now commonplace and experiments at significantly higher intensities are underway or anticipated [70], evaluation of PIC codes in this regime is crucial. This chapter describes such a study.

We revisit the dynamics of a single free electron irradiated by a high-intensity plane electromagnetic wave as a test problem for evaluating the performance of a particle-in-cell code. The electron motion becomes relativistic at large normalized wave amplitudes, $a_0 \gg 1$. In this regime, most of the electron energy is associated with the longitudinal

motion (parallel to the field propagation direction) and the maximum relativistic γ-factor increases as $\gamma \approx a_0^2/2$. As a result of the longitudinal motion with relativistic velocity, the frequency of the transverse electron oscillations decreases by a factor of γ, which can become substantial for large wave amplitudes. If, for a given timestep, the simulation correctly reproduces the electron motion with $a_0 \approx 1$, one might expect that the relativistic motion of an electron with $a_0 \gg 1$ would also be correctly reproduced since the period of the oscillations increases with a_0. The numerical results presented below (in 1D3V) show an exactly opposite trend, with the accuracy quickly deteriorating with an increase of a_0 for a fixed timestep. A primary goal of this chapter is to understand this effect and develop a strategy for its avoidance or mitigation.

In what follows, we outline a criterion that must be considered when simulating electron acceleration by a high amplitude electromagnetic wave in an under-dense plasma. We show that the electron dynamics can be correctly reproduced only if the timestep is sufficiently small to resolve the electron motion near stopping points along the trajectory. This condition requires that the timestep in the simulation is less than $1/a_0\omega$, where ω is the wave frequency. This criterion is independent of constraints on spatial resolution. It becomes more stringent at higher wave amplitudes due to the fact that the acceleration is more rapid near the stopping points for larger a_0. This means that the error accumulates primarily along relatively small segments of the electron trajectory in the vicinity of the stopping points. We therefore propose adaptive electron sub-cycling as an efficient remedy. The idea is to reduce the timestep for a given electron when the acceleration can no longer be correctly reproduced using the original timestep. Our results show that sub-cycling permits a dramatic increase in accuracy with only a modest increase in the total number of time steps. Given current interest in direct laser acceleration [71, 72, 73], the rapidly increasing focus on using ultra-intense lasers to study radiation reaction [74, 75] and the ambition to explore QED effects with lasers in the near future [76], it is important that the new constraint on timestep described here be taken into account.

The rest of the chapter is organized as follows. In Sec. 4.2, we review the dynamics of a free electron irradiated by an incoming electromagnetic wave to establish the context

for the analysis that follows. In Sec. 4.3, we demonstrate using a significantly under-dense plasma that relative numerical errors grow with wave amplitude in the case of an electron accelerated by a laser pulse. In Secs. 4.4 and 4.5, we analyze the errors originating from the particle pusher and derive a corresponding criterion for the timestep. In Sec. 4.6, we show that the errors can be greatly reduced using adaptive sub-cycling which helps to better resolve the electron dynamics near stopping points. Finally, in Sec. 4.7, we summarize our results and discuss possible implementation of the sub-cycling in a particle-in-cell code.

4.2 Single Electron Dynamics in a Plane Wave

In this section, we summarize the key features of single electron dynamics in a plane wave in order to establish the context for the subsequent analysis of the numerical results. We consider a free electron irradiated by a plane wave that propagates along the x-axis. The wave electric field is directed along the y-axis and the wave magnetic field is directed along the z-axis. The wave propagation can be described using a normalized vector potential

$$\mathbf{a}\left(x,t\right)=a\left(\xi\right)\boldsymbol{e_y}, \tag{4.1}$$

where a is only a function of a dimensionless phase variable

$$\xi\equiv\ 2\pi\left(ct-x\right)/\lambda. \tag{4.2}$$

Here, λ is the wave-length, c is the speed of light, t is the time in the laboratory frame of reference, and $\boldsymbol{e_y}$ is a unit vector. The electric and magnetic fields of the wave are given by:

$$E=-\frac{m_e c}{|e|}\frac{\delta a}{\delta t}, \tag{4.3}$$

$$B=\frac{m_e c^2}{|e|}\frac{\delta a}{\delta x}. \tag{4.4}$$

An initially stationary electron irradiated by this wave moves only in the (x, y)-plane

according to the following equations:

$$\frac{d}{dt}\left(\frac{p_x}{m_e c}\right) = -\frac{|e|B}{\gamma m_e c}\frac{p_y}{m_e c}, \tag{4.5}$$

$$\frac{d}{dt}\left(\frac{p_y}{m_e c}\right) = -\frac{|e|E}{m_e c} + \frac{|e|B}{\gamma m_e c}\frac{p_x}{m_e c}, \tag{4.6}$$

$$\frac{dx}{dt} = \frac{c}{\gamma}\frac{p_x}{m_e c}, \tag{4.7}$$

$$\frac{dy}{dt} = \frac{c}{\gamma}\frac{p_y}{m_e c}, \tag{4.8}$$

where p_x and p_y are components of the electron momentum and

$$\gamma = \sqrt{1 + \left(\frac{p_x}{m_e c}\right)^2 + \left(\frac{p_y}{m_e c}\right)^2} \tag{4.9}$$

is the relativistic factor. This system of equations has two integrals of motion:

$$\frac{d}{dt}\left(\frac{p_y}{m_e c} - a\right) = 0, \tag{4.10}$$

$$\frac{d}{dt}\left(\gamma - \frac{p_x}{m_e c}\right) = 0. \tag{4.11}$$

We skip the derivation here, which can, for example, be found in Refs. [77] and [66].

The second integral of motion implies that the electron dephases from the wave at a constant rate. In order to show that, we first take the derivative of the phase variable ξ defined by Eq. 4.2 with respect to time t, which yields

$$\frac{d\xi}{dt} = \frac{\omega}{\gamma}\left(\gamma - \frac{p_x}{m_e c}\right). \tag{4.12}$$

On the other hand, the proper time that we denote as τ and the time t are related by the expression $d\tau/dt = 1/\gamma$. The proper time is the elapsed time that would be measured

by the electron itself. Using this relation in Eq. 4.12, we find that

$$\frac{d\xi}{d\tau} = \omega\left(\gamma - \frac{p_x}{m_e c}\right). \tag{4.13}$$

According to the integral of motion Eq. 4.11, the expression on the right-hand side is a constant and, therefore, $d\xi/d\tau$ is also a constant. This means that the phase of the field sampled by the electron increases linearly with proper time. It is then appropriate to interpret the integral of motion Eq. 4.11 as the corresponding dephasing rate. It should be emphasized that the value of the dephasing rate has a direct and significant impact on the maximum energy that the electron gains during acceleration by the wave [66, 68]. This aspect will play a key role in the subsequent analysis in Secs. 4.3 to 4.6.

If the electron is at rest ($p_x = p_y = 0$) before the wave arrives ($a = 0$), then it follows from Eq. 4.11 that

$$\gamma - \frac{p_x}{m_e c} = 1. \tag{4.14}$$

Using Eqs. 4.10 and 4.14, and the definition of γ, we find that

$$\frac{p_y}{m_e c} = a, \tag{4.15}$$

$$\frac{p_x}{m_e c} = \frac{a^2}{2}. \tag{4.16}$$

In momentum space, the electron always moves along a parabola $p_x/m_e c = (p_y/m_e c)^2/2$, with only the maximum displacement along p_x and p_y changing with the wave amplitude. Eqs. 4.15 and 4.16 give p_x and p_y only in terms of ξ and one still needs to integrate Eq. 4.7 in order to find $p_x(x,t)$ and $p_y(x,t)$. One can find from Eq. 4.7 using the definition of ξ given by Eq. 4.2 that

$$\frac{ct}{\lambda} = \frac{1}{2\pi}\int_0^{\xi} \gamma d\xi', \tag{4.17}$$

$$\frac{x}{\lambda} = \frac{1}{2\pi}\int_0^{\xi} (\gamma - 1)\, d\xi', \tag{4.18}$$

where $\gamma = 1 + a^2(\xi)/2$ according to Eqs. 4.9, 4.15, and 4.16. Equations 4.15 to 4.18 allow one to implicitly determine components of the electron momentum as functions of time t and axial distance x. To summarize, a free electron irradiated by a plane wave moves along a parabola in momentum space due to the fact that its dephasing rate $\gamma p_x/m_e c$ remains constant. The maximum electron γ-factor is $\gamma = 1 + a_0^2/2$ and the corresponding maximum electron energy gain is $\gamma m_e c^2$, where a_0 is the maximum value of a.

4.3 Simulation Results for a Significantly Underdense Plasma

In this section, we present several results from 1D3V particle-in-cell simulations (one spatial and three velocity dimensions) in order to determine how well the single electron dynamics described in Sec. 4.2 are reproduced numerically. We initialize a low-density hydrogenic plasma slab ($n_e = n_i = 10^{-3} n_c$, where n_c is the critical density for 1 μm light) with cold electrons that are irradiated by a plane electromagnetic wave. The plasma density is deliberately set very low so that space-charge effects are negligible during our runs and each electron effectively behaves as a free electron in a vacuum. The plasma is essentially acting as a convenient cold electron source. At this density, the effect of the electron currents on the field of the wave is also negligible in our runs. This setup mimics the initial conditions considered in Sec. 4.2. The normalized pulse amplitude a ramps up to a_0 and then remains constant. The exact profile of the electron density and the wave amplitude are not important. All the plasma electrons are equivalent in this setup and they only differ by their initial location. In what follows, we select one electron and track it throughout the simulation.

Figure 4.1 shows numerical results for $a_0 = 10$ and three different cell sizes, $\Delta x/\lambda = 1/20$, $1/40$, and $1/80$. In all three runs, the ratio of the timestep Δt to the cell size Δx was the same, with $c\Delta t/\Delta x = 0.95$. Figure 4.1(a) shows the trajectory of a single electron in momentum space and (b) shows the corresponding dephasing rate as a function of the

distance traveled by the electron from its initial location. The electron data is shown with dots, because it was recorded at discrete time intervals $dt = 0.075\lambda/c$. According to the analytical solution of Sec. 4.2, the electron should be moving along a parabola $p_x/m_e c = (p_y/m_e c)^2/2$, with $|p_y/m_e c| \leq a_0$ and $0 \leq p_x/m_e c \leq a_0^2/2$. The dephasing rate must remain constant and equal to unity, $\gamma p_x/m_e c = 1$. Not surprisingly, the convergence to the analytical solution improves as we decrease Δx, which in this case is equivalent to decreasing Δt because their ratio is maintained.

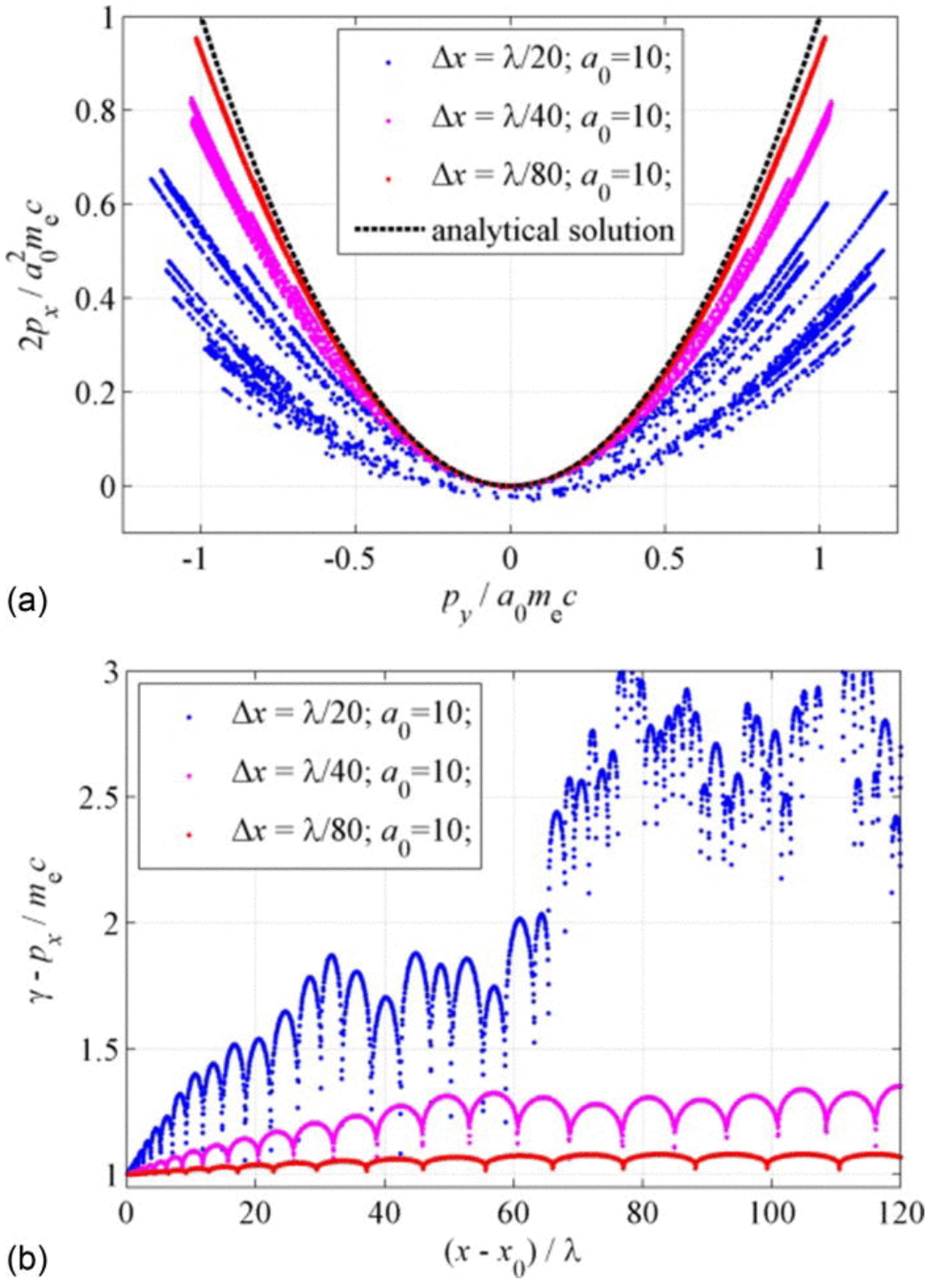

Figure 4.1: Electron momentum space (a) and the dephasing rate (b) for different values of cell size, Δx, at $a_0 = 10$. For all three runs, we set $c\Delta t/\Delta x = 0.95$. Figure reprinted from [5].

Figure 4.1 shows that there is a correlation between the deviation of the dephasing rate from unity and the deviation of the numerical solution in momentum space from the analytical result. This trend is also not surprising, because the dephasing rate determines how the field acting on the electron changes in time. An error in the dephasing causes an error in the electron acceleration and, consequently, leads to an error in the electron momentum. Note that errors in the dephasing rate also lead to considerable asymmetry in the transverse momentum p_y (see the results for $\Delta x = \lambda/20$ in Figs. 4.1 and 4.2), which can result in an unphysical electron drift perpendicular to the direction of the wave propagation.

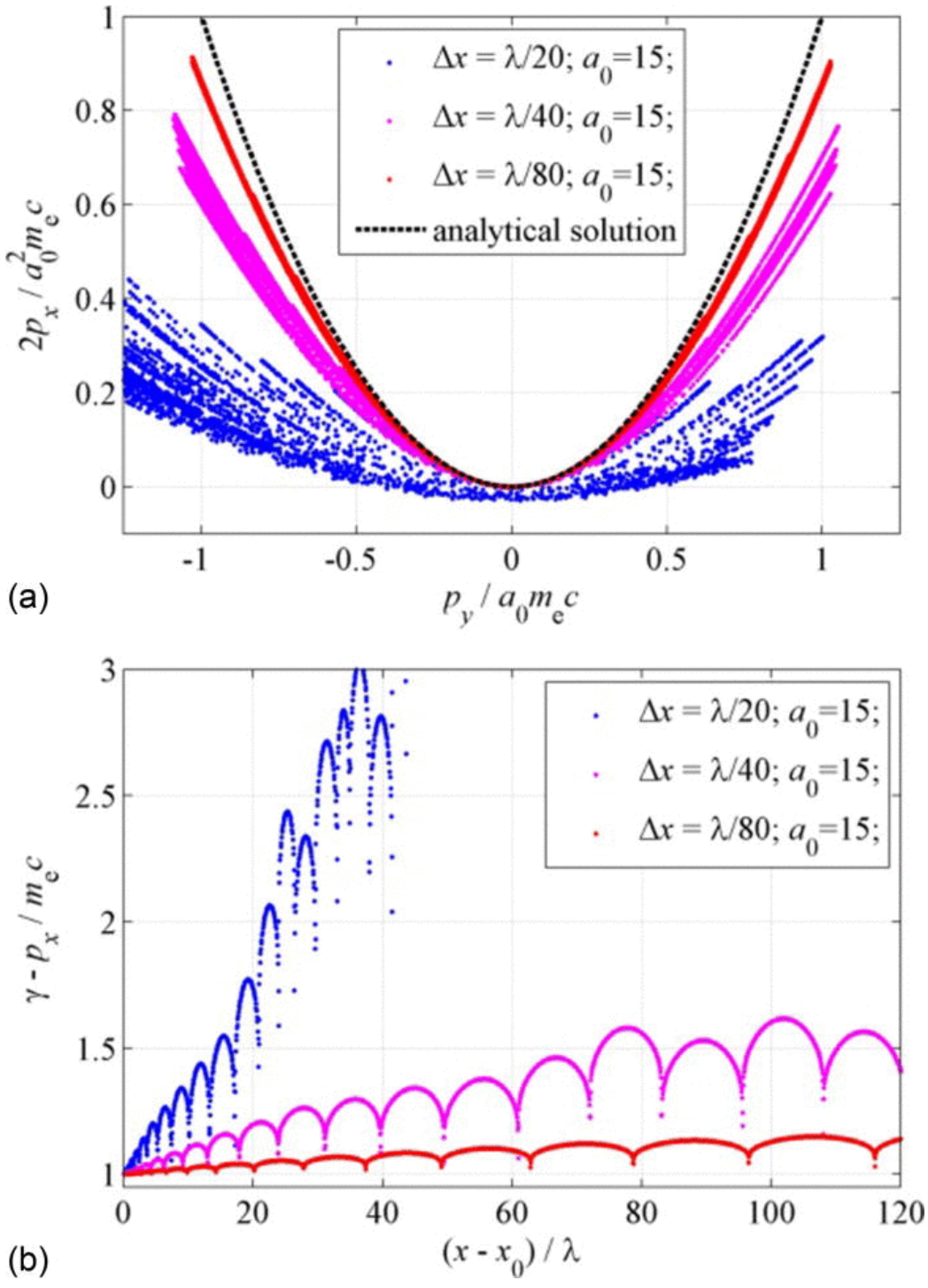

Figure 4.2: Electron momentum space (a) and the dephasing rate (b) for different values of cell size, Δx, at $a_0 = 15$. For all three runs, we set $c\Delta t/\Delta x = 0.95$. Figure reprinted from [5].

There is a distinct periodic structure of sharp downwards spikes in the dephasing rate. By comparing the time evolution of the dephasing rate and the electron momentum, we find that the downwards spikes correspond to stopping points. The numerical errors in the dephasing rate change considerably along the electron trajectory and they are the most significant in the vicinities of the stopping points. This is immediately evident from the change in the vertical distance between adjacent data points (dots) in Fig. 4.1(b). As stated earlier, the time interval between the adjacent data points is constant and, therefore, the dephasing rate changes at a greater rate around the downwards spikes.

Figure 4.2 shows the same quantities as Fig. 4.1, but for a higher wave amplitude of $a_0 = 15$. The already discussed trends seem to be similar in this case. We deliberately used the same set of cell sizes and the same ratio $c\Delta t/\Delta x$ as in the case of $a_0 = 10$ in order to determine how numerical errors scale with wave amplitude. Let us examine the runs with $\Delta x = \lambda/40$ for $a_0 = 10$ and $a_0 = 15$. The period of electron oscillations in the laser field increases with a_0 due to the increased γ-factor that is primarily associated with the longitudinal motion. This can be seen by comparing the distance between the downwards spikes in the dephasing rate that is also the distance between stopping points. Since the velocity of the longitudinal motion is close to c, longer distance translates directly into a longer interval between stopping points and thus a longer period of oscillations. The timestep for both runs at $a_0 = 10$ and $a_0 = 15$ is the same, so one might expect that the higher amplitude run would be better resolved and the numerical errors would be reduced. The comparison of the deviation in the dephasing rate from unity indicates that the trend is exactly the opposite. Greater errors in the dephasing rate then lead to greater errors in the electron momentum at higher wave amplitude.

We therefore conclude that the numerical accuracy deteriorates with increasing wave amplitude for a fixed timestep despite the fact that the period of the electron oscillations increases. In Secs. 4.4 to 4.7, we examine the source of the discovered increasing inaccuracy.

4.4 Analysis of Errors Originating from the Particle Pusher

In general, there are a wide range of factors that contribute to numerical errors in a particle-in-cell simulation (see Refs. [4, 78, 79, 80]). The results of Sec. 4.3 indicate that in our test problem the numerical errors in the dephasing rate tend to significantly increase around specific points of the electron trajectory the stopping points. This observation serves as a motivation for us to consider the particle pusher separately.

In what follows, we specify the wave field *analytically*. In the test problem under consideration, this is simply an electromagnetic pulse propagating in a vacuum. This approach allows us to isolate the errors introduced by the particle pusher. We use the standard Boris pusher [4], coded in MATLAB, to advance the electron momentum and coordinates in time using the analytical solution for the field at the electron location. The following results are for an initially immobile single electron irradiated by a plane electromagnetic wave.

Figure 4.3 shows the results for three different wave amplitudes and the same timestep, $c\Delta t/\lambda = 1/50$; (a) shows the electron momentum space. Deviation from the analytical solution predicting $p_x/m_e c = (p_y/m_e c)^2/2$ [see Eqs. 4.15 and 4.16] increases with wave amplitude. Part (b) shows the dephasing rate as a function of the longitudinal displacement. The errors in the dephasing rate and the deviation from $\gamma p_x/m_e c = 1$ also increase with a_0. Both trends for the momentum and dephasing are similar to those that emerge from comparing the results for $a_0 = 10$ and $a_0 = 15$ in Sec. 4.3 (see Figs. 4.1 and 4.2). However, the wave fields in Sec. 4.3 were calculated numerically using a finite difference scheme for the Maxwell equations. This suggests that the increase in numerical errors is caused by the particle pusher, whereas the errors resulting from numerical integration of the field equations are less significant for the cell size and timestep used.

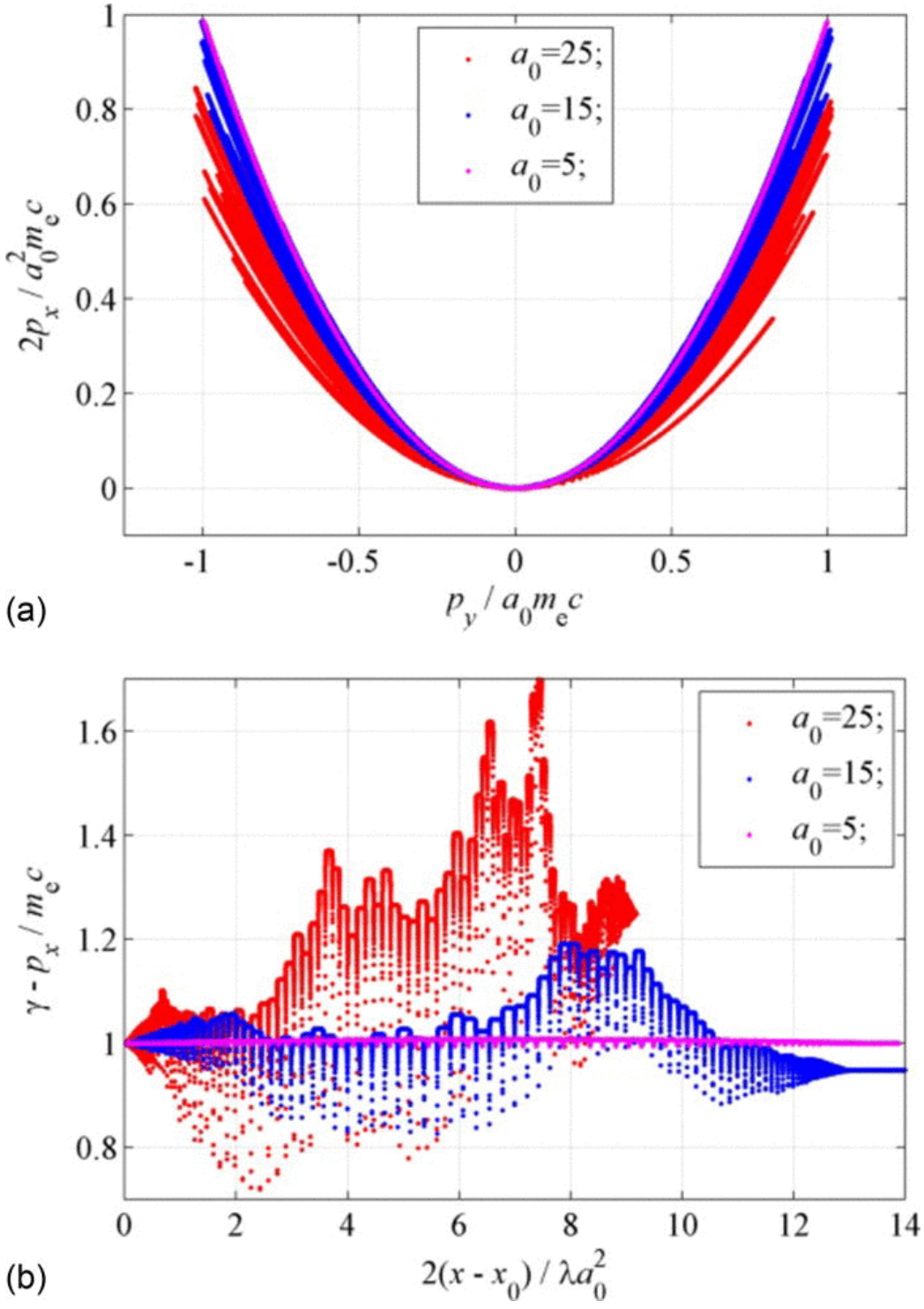

Figure 4.3: Electron momentum space (a) and the dephasing rate (b) for $a_0 = 5$, 15, and 25 calculated using a particle pusher and an analytical field. We set $c\Delta t/\lambda = 1/50$ for all three runs. Figure reprinted from [5].

In order to see the trend for the numerical errors more clearly, we have performed field amplitude scans for three different timesteps, $c\Delta t/\lambda = 1/60$, $1/120$, and $1/180$. The results are shown in Fig. 4.4 for $5 \leq a_0 \leq 40$. Part (a) shows the discrepancy in the electron energy gain and (b) shows the discrepancy in the dephasing rate. For each field amplitude, we determine the maximum γ-factor achieved by the electron in the simulation, denoted as γ_{max}. The analytical solution in Sec. 4.2 predicts the maximum γ-factor to be

$$\gamma_* = 1 + a_0^2/2, \tag{4.19}$$

where a_0 is the peak amplitude of the pulse. The quantity plotted in Fig. 4.4(a) is $(\gamma_{max}\gamma)/\gamma$, which is the relative error in the predicted electron energy gain. For each wave amplitude, we also determine the maximum absolute deviation of the dephasing rate $\gamma p_x/m_e c$ from unity. This is the quantity plotted in Fig. 4.4(b).

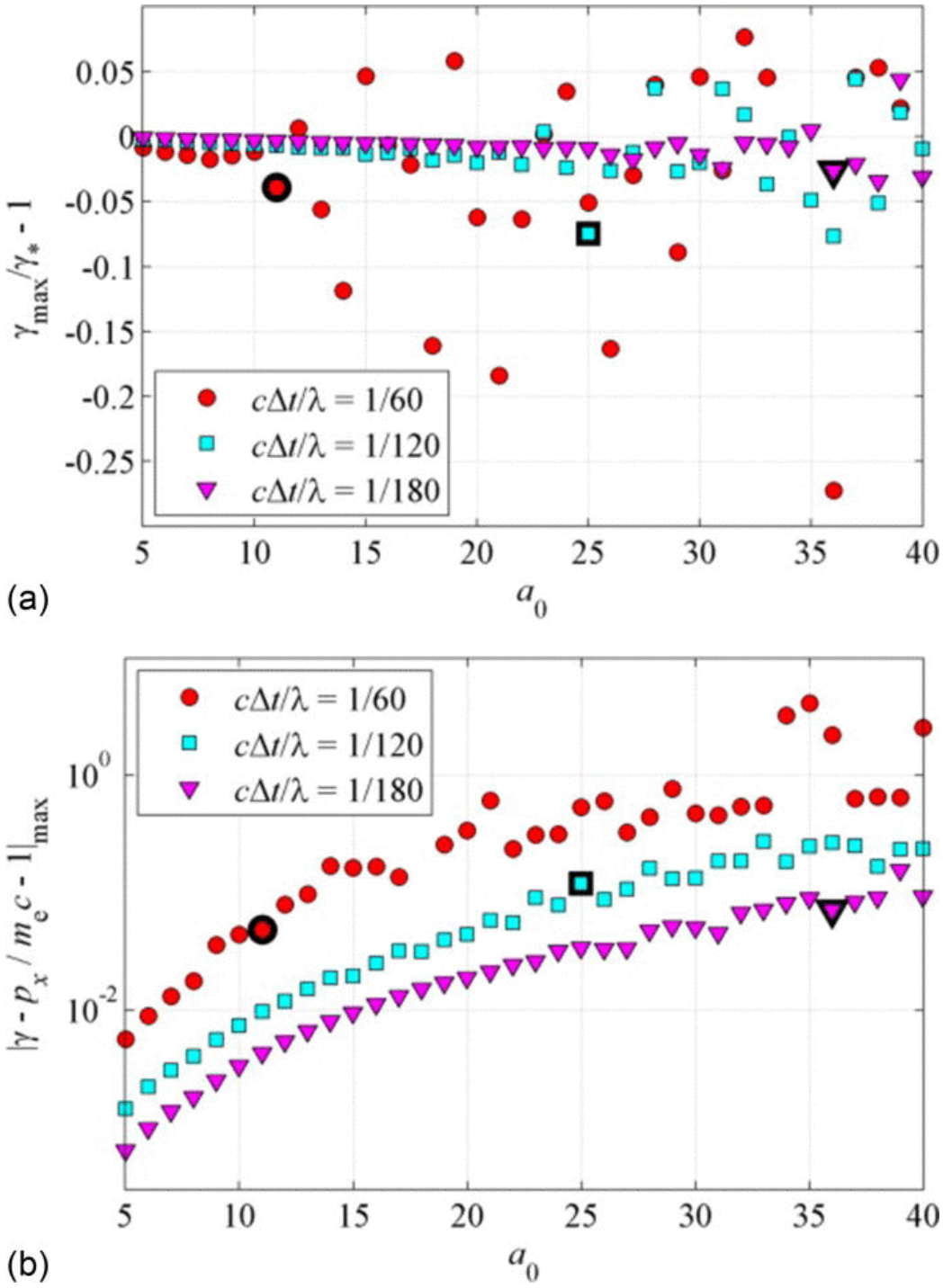

Figure 4.4: Field amplitude scans of the relative error in the electron energy gain (a) and the error in the dephasing rate (b) using three different time steps: $c\Delta t/\lambda = 1/60$, $1/120$, and $1/180$. See discussion in text of these figures of merit. The enlarged markers indicate the threshold intensity for the onset of large errors in the electron energy gain for each value of $c\Delta t/\lambda$ (see Table 4.1). Table reprinted from [5].

There are several important trends that become apparent from the scans presented in Fig. 4.4. The error in the dephasing rate gradually increases with a_0 regardless of the timestep used to integrate the electron equations of motion. In contrast with that, the discrepancy in the electron energy gain exhibits a threshold behavior with the increase of a_0. The threshold for the onset of large errors in the electron energy gain appears to scale inversely proportional to the timestep used in the particle pusher. If, for example, we define this threshold as $|\gamma_{max} - \gamma|/\gamma = 0.025$, then we find that the discrepancy exceeds the threshold value at $a_0 = 11$, 25, and 36 for $c\Delta t/\lambda = 1/60$, $1/120$, and $1/180$. This is indeed a threshold, since the discrepancy in the energy gain jumps up considerably at these wave amplitudes. We have listed these numbers in Table 4.1. We have also listed in Table 4.1 $|\gamma - p_x/m_e c - 1|_{max}$ above the threshold. The threshold clearly occurs at roughly the same level of discrepancy in the dephasing rate in all three cases. The values from Table 4.1 are shown with enlarged markers in Fig. 4.4.

We can summarize this section by concluding that there is a general trend for the errors in the dephasing rate to increase with wave amplitude. Once the discrepancy in the dephasing rate approaches 10%, a rapid increase in the discrepancy in the electron energy gain takes place. The corresponding threshold wave amplitude scales inversely proportional to the timestep used to integrate the electron equations of motion.

4.5 Criterion for the Timestep

In Secs. 4.3 and 4.4, we showed that the numerical errors tend to increase with wave amplitude. In this section, we formulate a criterion for the timestep that must be satisfied in order to accurately reproduce the electron dynamics in a strong electromagnetic wave.

Table 4.1: Threshold for errors in the energy gain. Table reprinted from [5].

$c\Delta t/\lambda$	a_0	$\lvert\gamma - p_x/m_e c - 1\rvert_{max}$
1/60	11	0.080
1/120	25	0.088
1/180	36	0.083

Chapter 3 described how a standard Boris particle pusher advances the electron momentum in time. It is done in three subsequent stages using given electric and magnetic fields. It first accelerates the electron using the electric field. It then performs a rotation in the magnetic field. The last stage is another push using the electric field. The (half) rotation angle is

$$\Psi = -\frac{1}{2}\frac{|e|E\lambda}{\gamma m_e c^2}\frac{c\Delta t}{\lambda}, \tag{4.20}$$

where B is the magnetic field and γ is the relativistic factor of the electron after the first push by the electric field.

This procedure necessarily requires the rotation angle to be small, which can be easily understood in the context of the test problem that we are considering. As the electron is pushed forward by the wave, its transverse momentum oscillates while the longitudinal momentum remains positive. Therefore, the electron never performs a full rotation in momentum space. On the other hand, to pick an extreme case, if the rotation angle in the Boris pusher is comparable to π, then the particle pusher qualitatively changes the electron motion causing the electron to move backwards.

Our next step is to determine the relation between the rotation angle and the wave amplitude in our test problem. Let us take a pulse that, after some initial ramp-up, has a constant amplitude, with $a = a_0 \sin(\xi)$. In this case, the electric and magnetic fields acting on the electron are

$$E = B = -m_e c^2 a_0 \cos(\xi) 2\pi/\lambda|e|. \tag{4.21}$$

According to the analytical solution of Sec. 4.2, the γ-factor of the electron is

$$\gamma = 1 + \frac{a^2}{2}. \tag{4.22}$$

The ratio B/γ has the largest absolute value for $a = 0$. Thus, the rotation angle for a

given timestep Δt has also the largest value for $a = 0$,

$$|\Psi|_{max} = \pi a_0 \frac{c\Delta t}{\lambda}. \tag{4.23}$$

The requirement $|\Psi|_{max} \ll \pi$ now yields

$$\frac{c\Delta t}{\lambda} \ll \frac{1}{a_0}. \tag{4.24}$$

This condition indicates that the wave amplitude imposes an upper limit on the timestep that can be used by the particle pusher. It should be noted that the discussed criterion is equivalent to the requirement that the smallest time scale in the problem must be resolved. In our case, the restriction is imposed by the wave magnetic field and the corresponding time scale that must be resolved is the gyro-period at $a = 0$.

The points along the electron trajectory where a vanishes are stopping points. This is evident from the analytical solution of Sec. 4.2. Equations 4.15 and 4.16 give p_x and p_y as functions of a, with both vanishing for $a = 0$. On the other hand, the electric and magnetic fields of the wave reach their maximum amplitude at a stopping point. Therefore, the vicinity of a stopping point is that part of the electron trajectory where the electron experiences the strongest acceleration and, as a result, the rotation angle has the largest amplitude.

It might seem that the derived criterion for the timestep is unnecessarily restrictive due to the fact that it is imposed by electron dynamics near stopping points. Indeed, even if the criterion is not satisfied, the electron momentum gain that would be calculated incorrectly would still be relatively small compared to both $|p_y| = a_0$ and $p_x = a_0^2/2$. However, this argument does not take into account the corresponding error in the dephasing rate and its impact on the subsequent electron acceleration by the wave.

In order to show that errors in acceleration near stopping points are indeed critical, let us first estimate how the dephasing rate changes as a result of these errors. We define the

dephasing rate as

$$I \equiv \gamma - \frac{p_x}{m_e c} = \sqrt{1 + 1 + \left(\frac{p_x}{m_e c}\right)^2 + \left(\frac{p_y}{m_e c}\right)^2} - \frac{p_x}{m_e c}. \tag{4.25}$$

Let us consider an electron as it starts its motion right at the stopping point with correct initial conditions determined from the analytical solution, so that $p_x = p_y = 0$ and $a = 0$. The electron dephasing rate is then $I = 1$. We now use a standard Boris pusher to advance the electron momentum by one timestep. We assume that the rotation is calculated incorrectly and we want to estimate the resulting error in the dephasing rate. The momentum gain resulting from the acceleration by the wave electric field over a time interval equal to Δt is roughly $|\Delta p/m_e c| = 2\pi a_0 c \Delta t/\lambda$. Deliberately assuming the worst case scenario, we set $p_y = 0$ and $p_x = \pm|\Delta p|$ in Eq. 4.25. For $|\Delta p/m_e c| \ll 1$, we have the following estimate for the dephasing after just one timestep:

$$I \approx 1 \pm |\Delta p/m_e c| \approx 1 \pm 2\pi a_0 c \Delta t/\lambda. \tag{4.26}$$

An electron with an initial axial momentum $p_x = \pm|\Delta p|$ would have the same dephasing rate. An analytical solution for such an electron is given in Ref. [66]. The maximum electron γ-factor according to Eq. (25) of Ref. [66] is $\gamma_{max} = (1 + a_0^2 + I^2)/2I$. The difference in the maximum γ-factor achieved by this electron as compared to the case considered in Sec. 4.2 where the electron is initially at rest is

$$\frac{\gamma_{max} - \gamma_*}{\gamma_*} = (1 - I)\frac{1 + a_0^2 - I}{I\left(2 + a_0^2\right)}. \tag{4.27}$$

We can now employ this expression to estimate the impact that an error in the dephasing has on the electron energy gain. We use the estimate for the dephasing rate given by Eq. 4.26 and assume that the error in the dephasing rate is relatively small, $|1 - I| \ll 1$. It then follows from Eq. 4.27 that

$$\frac{\gamma_{max} - \gamma_*}{\gamma_*} \approx 1 - I \approx \pm 2\pi a_0 \frac{c\Delta t}{\lambda}. \tag{4.28}$$

This estimate indicates that the relative error in the electron energy gain is of the same order as the error in dephasing rate.

These estimates elucidate the physical basis for the restriction on the timestep given by Eq. 4.24. If the condition Eq. 4.24 is not satisfied, then the numerical error resulting from numerical integration of the electron equations of motion near a stopping point leads to a considerable error in the dephasing rate. The error in the momentum gain is relatively small at this stage. However, the error in the dephasing rate affects the subsequent electron acceleration by the wave even if no additional errors are introduced, causing a considerable error in the maximum electron energy gain.

4.6 Adaptive Sub-Cycling

We have so far examined the errors introduced by a standard Boris pusher and determined that the electron dynamics in the vicinity of stopping points imposes a stringent upper limit on the timestep. Guided by these observations, we develop in this section a procedure that allows us to considerably improve the accuracy with only a modest increase of the total number of time steps when calculating the electron dynamics.

A direct way to reduce numerical errors generated by the particle pusher is by decreasing the timestep Δt. However, if the timestep reduction necessary to satisfy the criterion Eq. 4.24 is significant, then this approach would greatly increase the total number of timesteps needed to simulate the same time interval. On the other hand, the increased precision is not helpful and thus unnecessary for the majority of the electron trajectory.

A more efficient way to reduce the numerical errors is by adaptively decreasing the timestep only when necessary to ensure that the criterion Eq. 4.24 is always satisfied. We implement this by introducing a critical rotation angle Ψ_*. We also choose a base value for the timestep $\Delta t = \Delta_0$. At the beginning of each timestep, we estimate the rotation angle for the particle pusher, Ψ_{est}, using Eq. 4.20, where the value of γ is taken from the previous timestep and $\Delta t = \Delta_0$. If this estimate exceeds Ψ_*, then we reduce Δt, which reduces Ψ_{est}, to make Ψ_{est} less than Ψ_*. For convenience, we choose the reduced timestep

from a list of discrete values $\Delta t = \Delta_0/4^k$, where $k = 1, 2, 3....$ We pick the largest value that yields $\Psi_{est} < \Psi_*$. The algorithm automatically resets Δt to the base value Δ_0 if a reduced timestep is no longer necessary.

The standard Boris pusher updates electron position and momentum at interleaved time points, staggered such that they leapfrog over each other. In order to successfully implement the described algorithm, one must synchronize the electron position and momentum at a time point corresponding to the momentum before changing the timestep. Therefore, the particle pushing algorithm should involve the following two steps after the momentum has been updated and the timestep has to be changed. The first step is to advance the electron position by $\Delta t/2$, where Δt is the original timestep. The second step is to advance the electron position by $\Delta t/2$, where Δt is the new timestep. After this, the standard particle pushing algorithm can be used with a new timestep, starting with a momentum update.

4.6.1 Subcycling Example

As an example, we re-run the three cases presented in Fig. 4.3 (see Sec. 4.4) now using adaptive sub-cycling. The base timestep for all three runs is set to $c\Delta_0/\lambda = 1/50$, which was the timestep used to generate Fig. 4.3. The critical rotation angle is set to $\Psi_* = 0.05$. The resulting electron momentum and electron dephasing are shown in Fig. 4.5. The deviation of the dephasing rate from unity has been significantly reduced, as compared to the results in Fig. 4.3(b). It is less than 10% even for $a_0 = 25$. As a result, the deviation of the electron momentum from the analytical solution given in Sec. 4.4 is no longer visually detectable. It has been dramatically reduced compared to the results in Fig. 4.3(a).

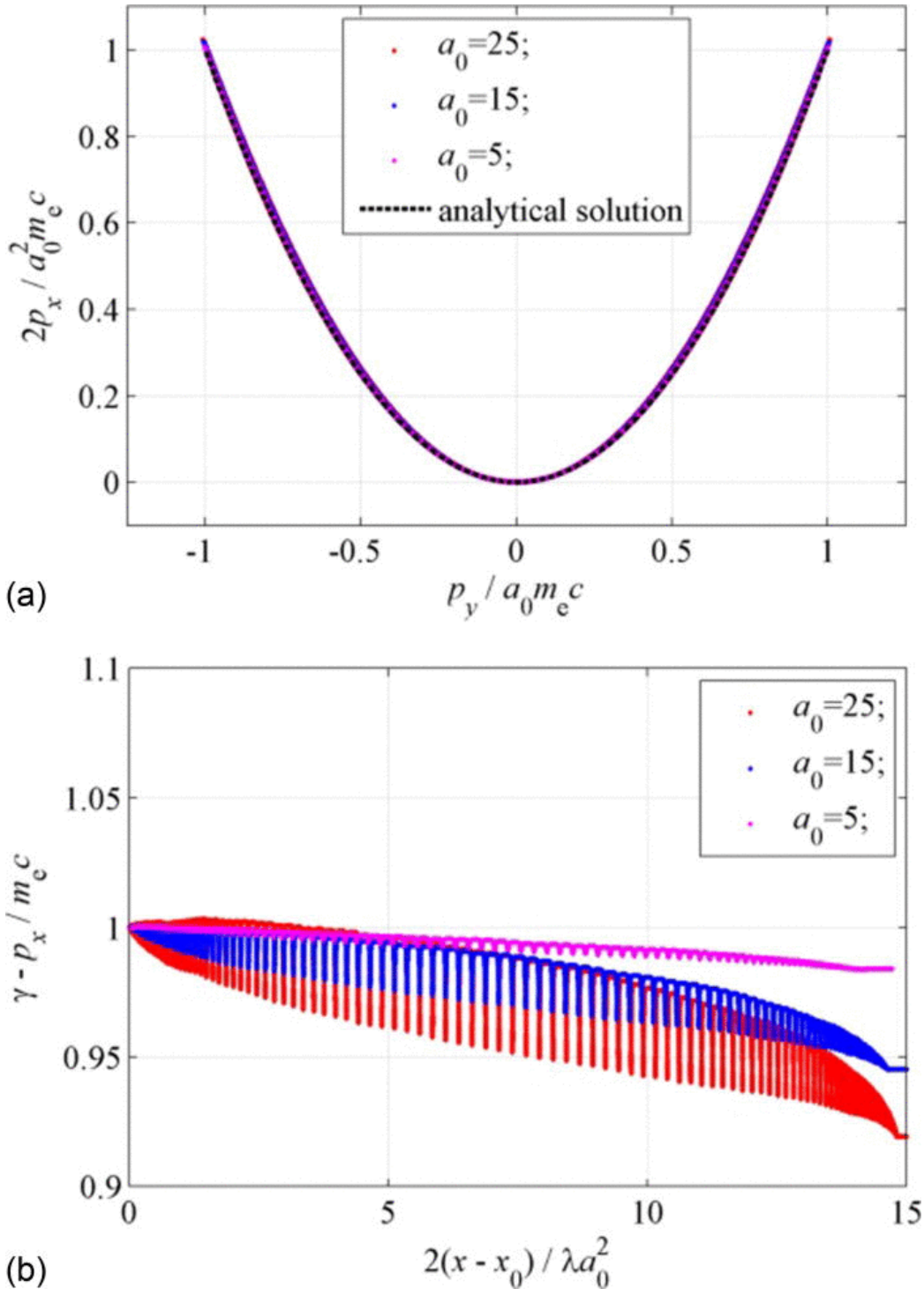

Figure 4.5: Electron momentum space (a) and the dephasing rate (b) for $a_0 = 5$, 15, and 25 calculated using adaptive sub-cycling. The particle pusher uses an analytical field. The base timestep is set at $c\Delta_0/\lambda = 1/50$ for all three runs. Figure reprinted from [5].

In Table 4.2, we have listed how many times each timestep value is used during the sub-cycling. The relative number of steps using the base timestep value increases with increasing a_0, so that the number of reduced timesteps is less than 13% for $a_0 = 25$. Recall that the same value of a_0 had the largest deviation from the analytical solution in Fig. 4.3. Therefore, the sub-cycling algorithm becomes more efficient at higher wave amplitudes and a significant improvement of the numerical results can be achieved using only a modest increase in the total number of timesteps. This is not surprising, since the electron spends only a small fraction of its time near the stopping points, as the time interval between the stopping points increases as $\gamma_{max} \propto a_0^2$.

We have performed wave amplitude scans for three different base timestep values, $c\Delta_0/\lambda = 1/60$, $1/120$, and $1/180$ for $5 \leq a_0 \leq 40$. The critical rotation angle was set to $\Psi_* = 0.05$. Without sub-cycling, these three scans would produce the results shown in Fig. 4.4. The results using sub-cycling are shown in Fig. 4.6. As in the case of Fig. 4.4, part (a) shows the discrepancy in the electron energy gain and (b) shows the discrepancy in the dephasing rate. For each wave amplitude, we determine the maximum γ-factor achieved by the electron in the simulation, denoted as γ_{max}. The analytical solution in Sec. 4.2 predicts the maximum γ-factor to be $\gamma_* = 1 + a_0^2/2$, where a_0 is the peak amplitude of the pulse. The quantity plotted in Fig. 4.6(a) is $(\gamma_{max}\gamma)/\gamma$, which is the relative error in the predicted electron energy gain. For each wave amplitude, we also determine the maximum absolute deviation of the dephasing rate $\gamma p_x/m_e c$ from unity. This is the quantity plotted in Fig. 4.6(b).

Table 4.2: Number of timesteps used for sub-cycling. Figure reprinted from [5].

a_0	Ψ_{max}	Δt(%)	$\Delta t/4$(%)	$\Delta t/16$(%)	$\Delta t/64$(%)
5	0.05	58	30	12	0
15	0.05	78	13	8	1
25	0.05	87	7	4	2

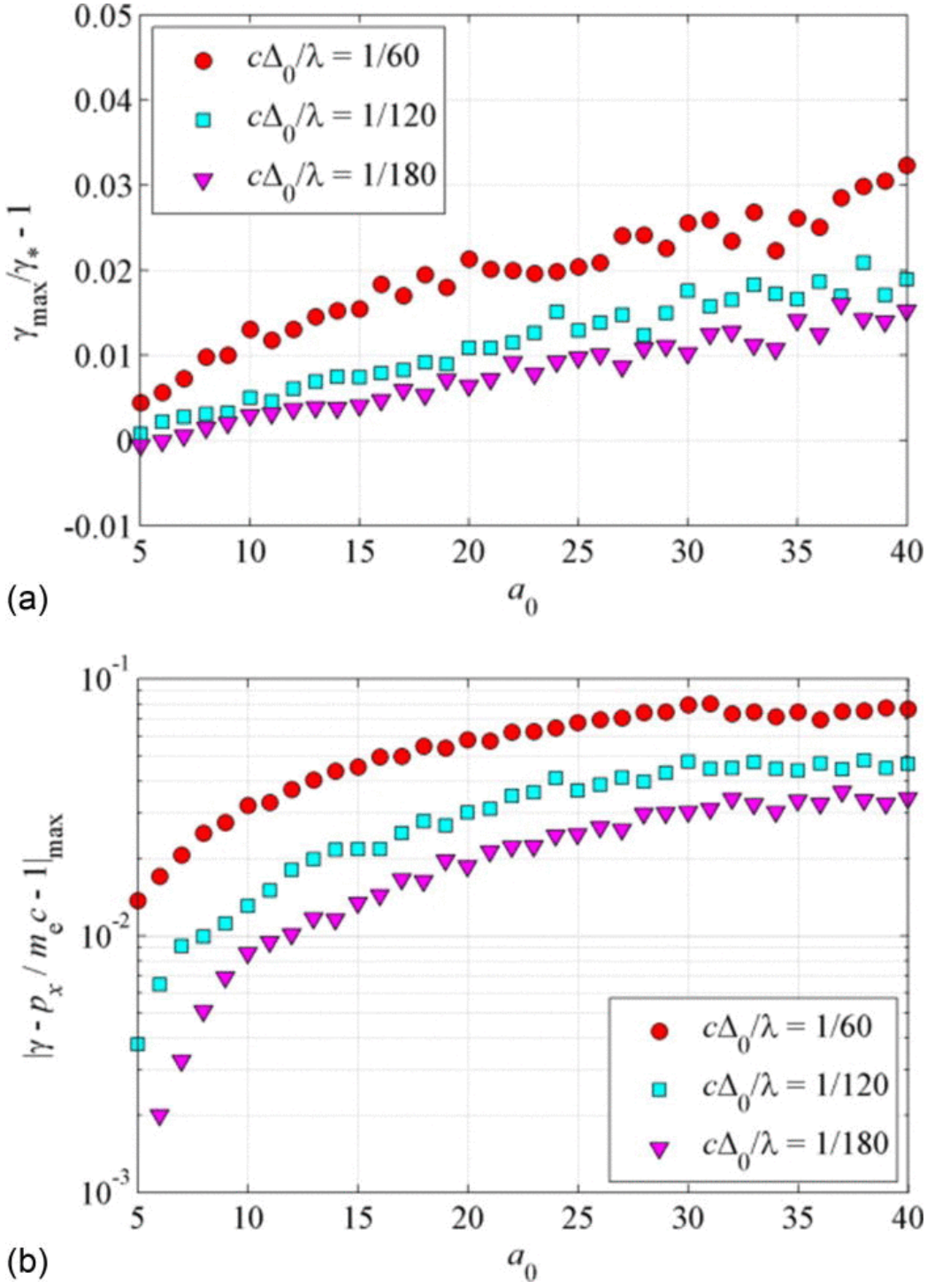

Figure 4.6: Field amplitude scans of the relative error in the electron energy gain (a) and the error in the dephasing rate (b) using adaptive sub-cycling for base timestep values $c\Delta_0/\lambda = 1/60$, 1/120, and 1/180. Figure reprinted from [5].

The trends seen in Fig. 4.5 are confirmed by the wave amplitude scans in Fig. 4.6. The deviation from the analytical solution of the dephasing and the electron energy gain has been dramatically reduced. The errors in the dephasing rate remain below 10% for all runs. The errors in the electron energy gain now increase gradually with a_0 and do not exhibit the threshold behavior seen in Fig. 4.4. This is due to the fact that the amplitude of the rotation angle in the particle pusher always remains smaller than $\Psi_* = 0.05$, which prevents the particle pusher from introducing qualitative changes to the electron dynamics near the turning points.

4.6.2 Efficiency of the Subcycling Algorithm

The key metric of the proposed algorithm is the relative increase in the total number of time steps between two stopping points due to the sub-cycling. In order to evaluate this quantity, we consider a vicinity of a stopping point $\xi = 0$ where the wave amplitude is $a(\xi) = a_0 \sin(\xi)$. We assume that $a_0 \gg 1$ and that the condition given by Eq. 4.24 is not satisfied for $\Delta t = \Delta_0$, so that the sub-cycling is required.

The fact that the criterion Eq. 4.24 is not satisfied implies that the rotation angle Ψ defined by Eq. 4.20 exceeds Ψ_* at $\xi = 0$. As the electron accelerates from the stopping point, the rotation angle decreases with the increase of ξ. We use Eq. 4.20 together with the expressions for the fields given by Eq. 4.21 to find that

$$\Psi(\xi) = \pi \frac{c\Delta t}{\lambda} \frac{a_0 \cos(\xi)}{1 + a_0^2 \sin^2(\xi)/2}. \tag{4.29}$$

The condition $\Psi(0) = \Psi_*$ sets the smallest timestep Δt_{min} that the sub-cycling procedure would have to use, which is

$$\frac{c\Delta t_{min}}{\lambda} = \frac{\Psi_*}{\pi a_0}. \tag{4.30}$$

The sub-cycling is only needed for $|\xi| < \xi_*$, where ξ_* is defined by the condition $\Psi(\xi_*) = \Psi_*$. Away from the stopping point, where $\Psi < \Psi_*$, the sub-cycling is not necessary. We assume that Ψ matches Ψ_* close to $\xi = 0$, with $\xi \ll \pi$. Otherwise, the base timestep is too

large and most of the electron trajectory has to be sub-cycled. The reduction of Ψ at $\xi \ll 1$ occurs due to the denominator in Eq. 4.29 when the term proportional to $\sin(\xi)$ starts to dominate. In order to find the value of ξ that yields $\Psi = \Psi_*$, we retain only the $\sin(\xi)$-term in the denominator and expand the expression in Eq. 4.29 with respect to ξ. To the lowest order in ξ, we then have

$$\Psi(\xi) = \pi \frac{c\Delta_0}{\lambda} \frac{2}{a_0 \xi^2}. \tag{4.31}$$

It follows from Eq. 4.31 that $\Psi = \Psi_*$ at

$$\xi \approx \xi_* \equiv \sqrt{\frac{1}{a_0} \frac{2\pi}{\Psi_*} \frac{c\Delta_0}{\lambda}}. \tag{4.32}$$

The travel time from the stopping point to the point where $\xi = \xi_*$ can be calculated using Eq. 4.17. Taking into account that $\gamma = 1 + a^2(\xi)/2$ and assuming that $\xi \ll 1$, we find that to the lowest order in ξ_* this travel time is

$$\frac{ct}{\lambda} = \frac{ct_*}{\lambda} \equiv \frac{1}{2\pi} \frac{a_0^2}{2} \frac{\xi_*^3}{3}. \tag{4.33}$$

On the other hand, the travel time to the next stopping point is

$$\frac{ct}{\lambda} = \frac{ct_s}{\lambda} \equiv \frac{a_0^2}{8}. \tag{4.34}$$

We found this expression by performing the integration in Eq. 4.17 from $\xi = 0$ to $\xi = \pi$ and retaining only the leading term, which involves a_0. The total number of timesteps with $\Delta t = \Delta a_0$ between two stopping points is

$$N_0 = t_s/\Delta_0. \tag{4.35}$$

The total number of timesteps N_* with the sub-cycling can be estimated by using $\Delta t = \Delta t_{min}$ for the time interval that requires the sub-cycling

$$N_* = \frac{t_s - 2t_*}{\Delta_0} + \frac{2t_*}{\Delta t_{min}}. \tag{4.36}$$

This gives an upper estimate, since the actual algorithm is adaptive and not all timesteps are as small as Δt_{min}. The relative increase in the total number of timesteps is

$$\frac{N_* - N_0}{N_0} = \frac{2t_*}{t_s}\frac{\Delta_0}{\Delta t_{min}}. \tag{4.37}$$

We next use the expressions for t_*, t_s, Δt_{min}, and ξ to obtain that

$$\frac{N_* - N_0}{N_0} \approx \frac{2}{3\pi} a_0^2 \xi_*^5 = \frac{2}{3\pi}\frac{1}{\sqrt{a_0}}\left(\frac{2\pi}{\Psi_*}\frac{c\Delta_0}{\lambda}\right)^{5/2}. \tag{4.38}$$

Therefore, the relative number of extra timesteps decreases at least as fast as $1/\sqrt{a_0}$, which makes the sub-cycling mechanism more efficient at higher wave amplitudes.

Finally, it is important to point out the role of the adjustable parameter Ψ_* on two measures of performance. On the one hand, the number of extra steps increases as $\Psi_*^{-5/2}$ according to Eq. 4.38, which means that the efficiency of the sub-cycling decreases with a decrease of the critical rotation angle Ψ_*. On the other hand, the error in the dephasing also decreases with a decrease of Ψ_*. This can be illustrated using the results presented in Fig. 4.5. In addition to the oscillations in the dephasing between the stopping points, there is also a clear downwards shift introduced by changing the size of the timestep during the sub-cycling procedure. This trend leads to an error of roughly 8% at the end of the run for $a_0 = 25$. By reducing Ψ_* from 0.05 to 0.025 and holding other parameters fixed, we have reduced the dephasing error to less than 2%. Therefore, the value of the critical rotation angle Ψ_* must be carefully chosen such that the desired precision is achieved without sacrificing the efficiency.

4.7 Discussion

We have revisited the classic test problem of a single electron irradiated by a high-intensity plane electromagnetic wave to examine the performance of a particle-in-cell code. We found that the numerical accuracy consistently deteriorates with increasing wave amplitude for a fixed timestep. We have separately examined the accuracy of the standard Boris particle pusher and found that the particle pusher introduces significant errors while integrating the

electron motion in the vicinities of stopping points. Field amplitude scans reveal that the deviation of the dephasing rate from unity increases with a_0 regardless of the timestep. The errors in the energy gain have a threshold behavior with increasing a_0 caused by increased error in the dephasing rate and the threshold amplitude scales inversely proportional to Δt.

Based on these observations, we have derived a convenient criterion for the timestep used in the particle pusher

$$c\Delta t/\lambda = 1/a_0. \tag{4.39}$$

Our analysis shows that the stopping points are more prone to numerical errors than other parts of the electron trajectory. Numerical errors from the integration of the electron equation of motion near a stopping point lead to considerable error in the dephasing rate. The error in the momentum gain is relatively small at this stage; however, the error in the dephasing rate affects the subsequent electron acceleration by the wave causing considerable error in the maximum electron energy gain.

We have developed an efficient algorithm that allows us to reduce the numerical errors generated by the particle pusher. The algorithm uses the derived criterion to adaptively decrease the timestep to ensure that the criterion is always satisfied. We have demonstrated that this adaptive sub-cycling actually becomes more efficient at higher wave amplitudes, so that a significant improvement of the numerical results can be achieved using only a modest increase in the total number of timesteps.

In our analysis, we have used a standard Boris pusher to calculate the electron dynamics, since this is the integrator implemented in some of the PIC codes frequently used to model laser-plasma interactions. It has been pointed out that the Boris pusher might lead to errors when calculating orbits of relativistic electrons [79]. This can be important on those segments of the electron trajectory where the electron is moving forward with a high γ-factor and the electric and magnetic field contributions in the equation of motion almost cancel each other out. The Boris pusher does not correctly cancel the electric and magnetic field contributions in the case of a relativistic electron, which can lead to a spurious force

[79]. The spurious force and the resulting errors can be eliminated by using the Vay particle pusher [79] instead of the Boris pusher. In the regime considered in this chapter, the relative role of these errors is, however, not as significant as the role of the errors from integrating the electron equation of motion near the stopping points. This is evident from the dramatic improvement that we have achieved by implementing the sub-cycling algorithm while still using the Boris pusher.

Our discussion has so far been focused on the particle pusher as the main source of numerical errors. The degradation in numerical accuracy observed in PIC simulations under these conditions appears to be primarily from the particle pusher, rather than the field advance. However, another potential source of errors is the numerical dispersion produced by the field solver. It is well known that the frequency ω of a wave with wave-length λ is less than $\omega_* \equiv 2\pi c/\lambda$

$$\frac{\omega - \omega_*}{\omega_*} \approx -\frac{\pi^2}{6}\left(\frac{\Delta x}{\lambda}\right)^2 \left[1 - \left(\frac{c\Delta t}{\Delta x}\right)^2\right]. \tag{4.40}$$

This error can be greatly reduced by keeping the ratio $c\Delta t/\Delta x$ close to unity. The corresponding discussion can be found in Ref. [4].

The errors from the particle pusher that we have examined here should be particularly critical when simulating electron acceleration in an underdense plasma. In a two- and three-dimensional set-up, only a small group of electrons are accelerated directly by the laser pulse. Our approach to adaptive sub-cycling would be well suited in this case to improve the accuracy of the numerical results. Our algorithm would automatically single out energetic electrons accelerated by a high-amplitude field, leaving the timestep for the other electrons unchanged. In order to implement the adaptive sub-cycling in a given particle-in-cell code, one has to orbit-average the current density of the sub-cycled electrons in a way similar to those discussed in Refs. [81] and [82]. The orbit-averaged current can then be directly used in the field solver to calculate the fields using the global timestep.

Finally, it is worth emphasizing that the primary role of the proposed algorithm is to ensure that the multi-scale electron dynamics that takes place in the presence of a wave with

a large amplitude a_0 is recovered in a simulation by resolving the fundamental time-scale of the electron motion given by Eq. 4.39. If for given simulation parameters the criterion Eq. 4.39 is not satisfied, then significant errors near stopping points are unavoidable regardless of the numerical scheme. These errors can lead to significant errors in electron energy gain even when the total energy in the system may appear well conserved due to the use of an energy-conserving scheme. In fact, we have also observed the effect reported in Sec. 4.3 using the energy-conserving particle advance in the PIC code LSP [83]. This is the reason why adaptive particle orbit integration was introduced in an implicit energy-conserving scheme described in Ref. [84]. These general considerations also indicate that the proposed algorithm should be applied regardless of the plasma density whenever the time-scale set by a conventional PIC code is not sufficient to resolve the time-scale given by Eq. 4.39. The impact of the discussed errors in the case of a dense plasma still remains to be evaluated and only then can it be determined whether they are significant enough or can be ignored.

Chapter 5
Liquid Crystal Film Development

5.1 Motivation

[2]Ultra-intense laser technology improvements are allowing new, high-power laser facilities to achieve progressively higher repetition rates, soon to exceed 1 Hz with petawatt power[85]. Increased shot rates are necessary to probe new physics regimes [86] and also promise higher flux for experiments such as ion acceleration, neutron radiography, and energetic beam generation [87, 50, 88], and related applications like proton cancer therapy [89], but only if the problems of target insertion and pulse contrast enhancement at higher repetition rates can be solved. Many approaches originally developed for single-shot lasers will not work in this regime. Presented here is a method of inserting low-Z targets at sustained, moderate repetition rates in the form of freely suspended films made of the commonly available liquid crystal, 8CB [90]. The film thickness can be tuned over three orders of magnitude to access multiple experimental and optical application regimes. The basic approach described is also scalable to much higher repetition rates. The development of liquid crystal targets and the devices described in this chapter have taken several years and are the result of a collaborative effort; details on the development of the first liquid crystal targets can be found in Ref. [91], on the moderate-repetition rate target inserter in Ref. [6], and ongoing progress on a high-repetition rate device was discussed in Refs. [92] and [93].

A successful insertion mechanism for ultra-intense laser experiments and applications

[2]Much of this chapter is reprinted with permission from P. L. Poole, C. Willis, G. E. Cochran, R. T. Hanna, C. D. Andereck, and D. W. Schumacher, Applied Physics Letters, vol.109, 151109 (2016). Copyright 2016, American Institute of Physics [6].

must meet multiple requirements. First, targets must be thin to enable efficient laser interaction, e.g. 10 nm to above 1 μm for fundamental ion acceleration experiments [89]; changing thickness to optimize these interactions with the current norm of pre-manufactured, fixed thickness targets is cumbersome for single-shot experiments and impossible at repetition rate. Second, ultra-high intensities above 10^{20} W/cm^2 require few μm – accurate target alignment methods that currently impede moderate repetition rate operation. Third, targets must have sufficiently large extent to minimize plasma damage to the supporting structures. Finally, the target expense must be low to enable practical, sustained runs at moderate repetition rates. Other requirements, for example involving debris management, may arise beyond this minimum set.

Several current methods satisfy some of these requirements. Gas and liquid sprays allow for kHz repetition rate shots at mJ pulse energies [94, 95], but are non-ideal for some applications due to their dispersed nature [94] and spherical droplet expansion reducing ion energy and yield if ions are desired [95]. High rate liquid jets of cryogenic hydrogen [96] and water [97] currently are cumbersome to install and have relatively high vapor pressure near the target that disrupts ultra-intense laser propagation, respectively. A third technique passes a ribbon target between two motors [98]; despite enabling shot rates near 1 Hz, a several μm thick tape is required to survive laser interaction, and currently the motors cause positional jitter of tens of μm. While improvement of these technologies continues, currently none are feasible for moderate repetition rate, PW-class laser experiments using ultra-thin targets such as are needed for fundamental laser interaction studies or investigation the full range of ion acceleration mechanisms.

Laser pulse contrast enhancement also presents difficulties at moderate repetition rate – shots on the order of 1/min. Laser interactions can be critically affected by blow-off plasma and target expansion arising from poor intensity contrast [55]. This arises due to undesired, intense light arriving ahead of the short pulse. Such light is often referred to as “pre-pulse” and the resulting plasma, “pre-plasma”. This is often resolved with a plasma mirror device, typically anti-reflection (AR) coated fused silica, which initially transmits pre-pulse light before the main pulse leading edge forms a highly reflective plasma

surface. Locally the AR coating is destroyed on shot, and the mirror must be moved to an undamaged region. At moderate repetition rate, this is acceptable, but for high repetition rate ($\geq$ 1 Hz) this becomes cumbersome and a design which can be scaled to higher rates is needed. Additionally, laser interactions may benefit [99] from polarizations other than that easily generated from modern high intensity systems. Sufficiently large aperture zero-order waveplates are expensive and difficult to obtain, especially since they must be thin enough (sub-μm) to prevent nonlinear phase accumulation (B-integral) which otherwise degrades a short pulse focus.

A thin, tunable thickness medium provides a solution to these issues–optimizing ion acceleration from thickness-dependent processes; enhancing pulse contrast by selecting the appropriate thickness for interferometric prepulse rejection; and polarization adjustment with minimal pulse degradation using a zero-order waveplate film. Liquid crystal membranes preserve planar geometry while adding the considerable benefit of on-demand thickness variation between a few nm and several tens of μm [90], a range not possible with any other target material. Very low vapor pressure allows formation at typical experimental vacuum levels and low volume per film renders them ideal for long-term moderate repetition rate use. A device has been developed that forms such films under vacuum with the temperature and volume control necessary for thickness selection. The design passively maintains excellent alignment even for tight focus geometries, and has been used to demonstrate rapid, thin film target insertion and high power optics formation.

5.2 In-situ Film Formation Control

5.2.1 The Liquid Crystal 8CB

Liquid crystals exhibit mesophases incorporating features of conventional solid and liquid phases and characterized by degrees of molecular structure, with transitions between phases controlled by material temperature (thermotropic) or concentration in a solution (lytropic) [100]. The thermotropic liquid crystal 4'-octyl-4-cyanobiphenyl (8CB), shown in Fig. 5.1, is composed of two benzene rings and a long hydrocarbon tail, with $\rho \sim 1$ g/cm^3. 8CB has

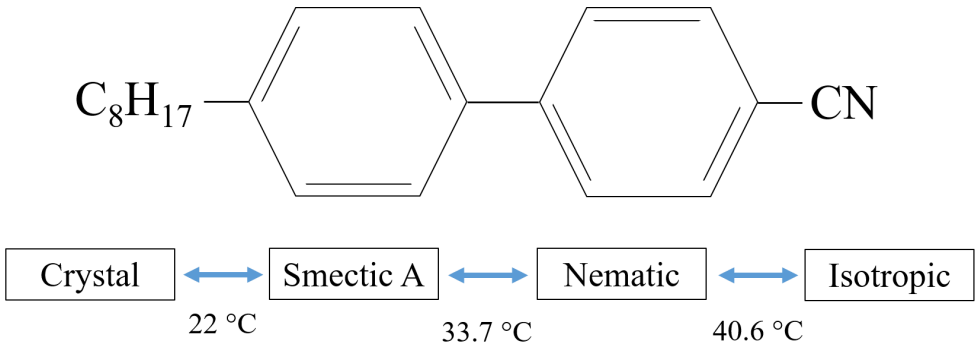

Figure 5.1: The liquid crystal 8CB ($C_{21}H_{25}N$). The transition from crystal to smectic A phase takes place at 22 °C; from smectic A to nematic at 33.7 °C; and from nematic to isotropic at 40.6 °C.

two phases between its crystal and isotropic states: smectic A[3], which has positional and orientational ordering of its molecules, and nematic, which only has orientational order. The smectic A phase, in which 8CB forms two molecule layers 2.9 nm thick, is utilized here for its molecular layering that allows thickness control and sufficient surface tension for freely suspended film formation [90]. 8CB has the further advantages of a convenient smectic phase near room temperature and low cost, making it an excellent choice for high-repetition rate laser systems which plan to shoot in excess of twenty thousand times per day.

5.2.2 Moderate Repetition Rate Target Insertion

Previous experiments using these targets were single-shot, where films were formed manually in individual copper frames before being transferred to the vacuum chamber for pumping, alignment, and the laser shot. Repetition-rated operation necessitates in-vacuum film formation, and so the Linear Slide Target Inserter (LSTI) shown in Fig. 5.2(a) was designed to be installed in-situ.

The LSTI consists of a wiper that moves vertically over a single aperture within a copper

[3]Smectic liquid crystal phases are defined in reference to the angle that the orientation of molecules in a layer makes with the plane defined by the layer. In a smectic A phase, this angle is 90°.

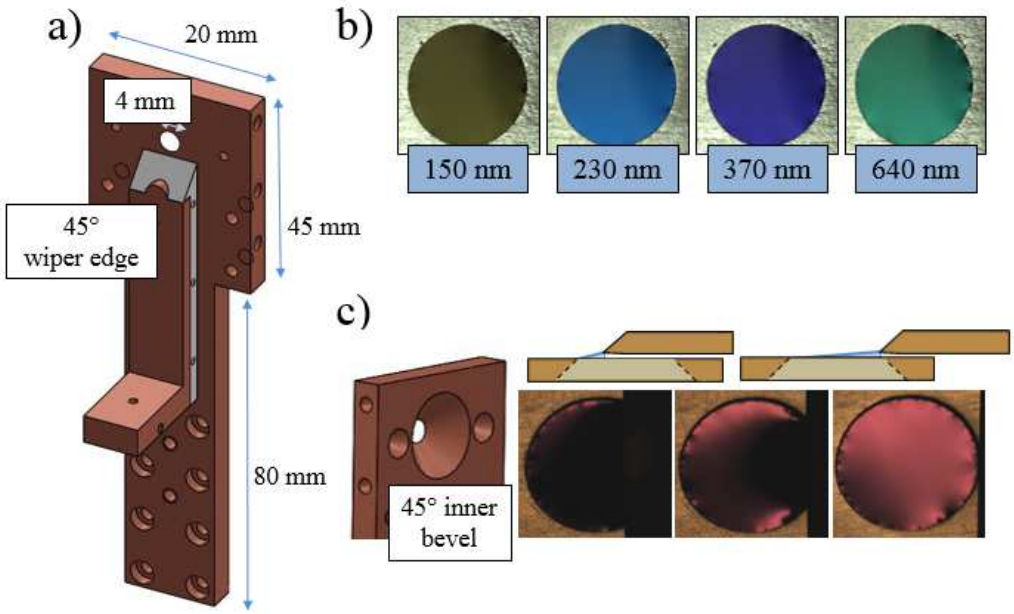

Figure 5.2: (a) Isometric view of Linear Slide Target Inserter (LSTI) frame and wiper, including a 4 mm aperture for film formation and side clearance holes for temperature monitoring and control. (b) Four films demonstrating thickness control. (c) Aperture bevel causes films to form within 2 μm of the same location each time. Here the wiper (moving left to right) moves slightly above the aperture, pulling the film upward as it forms. Figure reprinted from [6].

frame, guided by a thermoplastic polymer bridge (not shown to reveal detail) fitted with spring-loaded plungers to vary the force pressing the wiper down. Aperture diameters from 1 mm to over 11 mm are used for various applications and to prevent plasma damage to the edge. Surface smoothness is critical to thickness control, so the copper frame is polished to a mirror finish and the wiper is fitted with a Teflon bottom to prevent scratching. Temperature regulation is necessary for precise thickness control [90] and is achieved by water cooling the frame.

A liquid crystal charge is initially applied between the LSTI wiper and frame. A single sub-μm thick film requires volume on the order of 100 nL, challenging to dispense alone. Instead 1-10 μL or more is applied to act as a reservoir, and other formation parameters are varied to control thickness. In this way one application of liquid crystal can provide hundreds or thousands of films before the reservoir must be recharged, enabling prolonged target formation. Proper control of temperature, volume, and LSTI surface polish results in films of uniform thickness that are extremely smooth across their entire area, as shown in Fig. 5.2(b). Film thickness is monitored by a commercial white light spectral reflectance device relayed from outside the target chamber [90].

Of note is the LSTI formation plane repeatability. Figure 5.2(c) shows the 45° bevel behind the frame aperture. The smectic phase surface tension moves a forming film to the front bevel edge, resulting in formation to within 2 μm of the same position each time as measured with a μm resolution confocal target positioner [101]. Film formation is illustrated in Fig. 5.2(c): films begin stretched out of plane between the wiper and aperture edge, causing film curvature which appears dark in this image. As the wiper proceeds through the down-stroke the film lowers into the aperture plane. Targets form well within even small Rayleigh ranges ($F/2$), eliminating the significant problem of repeated target alignment at repetition rate.

Although temperature, applied volume, and surface polish all affect film formation, for practical, long-term film repeatability, wiper speed is the quickest and most convenient thickness-tuning variable. For example, while the volume applied sets an upper thickness limit and in general a higher temperature results in thicker films, sub-100 nm films can still

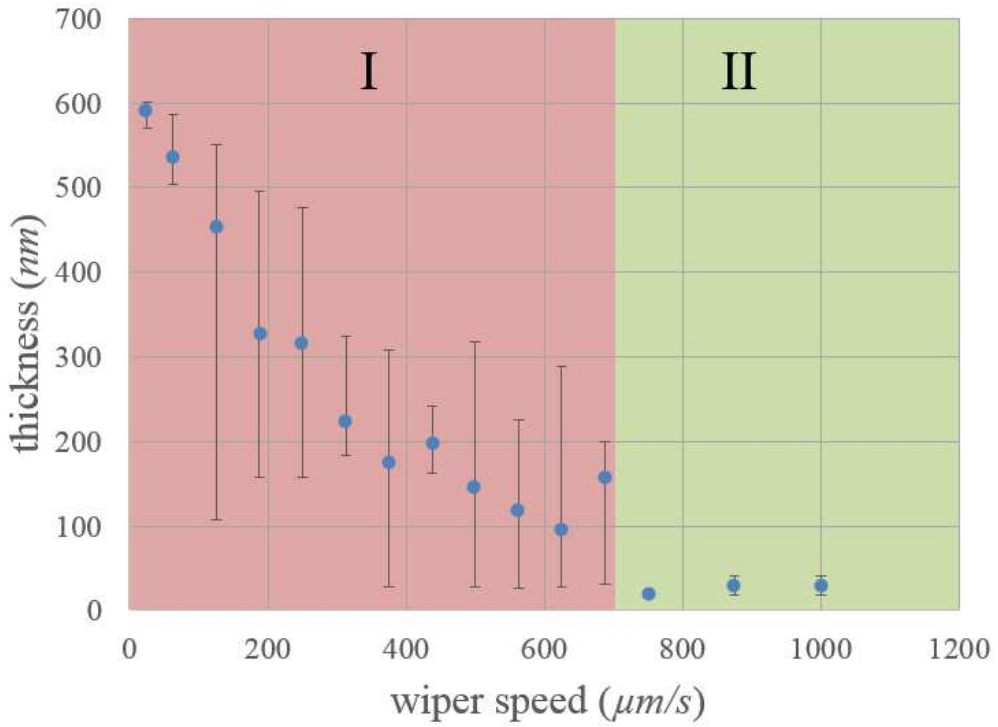

Figure 5.3: Film thickness control via wiper speed. Vertical bars show the range of thickness formed over five draws at each speed, while dots indicate the average of those films. Average thickness increases as the wiper speed decreases, but speeds in the right shaded area, Region II, form films consistently at sub-100 nm thicknesses. Figure reprinted from [6].

be produced under the conditions of large volume and high temperature with a sufficiently fast wiper speed. The effect can be seen in Fig. 5.3, where two observed regions of film formation have been highlighted. The vertical bars indicate the range of film thicknesses produced at the given wiper speed, while the circles show the average of these thicknesses. Region II, at the fastest speeds, produces sub-100 nm films with precision within 10 nm each time–this is ideal for applications where a consistent, thin target is desired, as is the case of some ion acceleration mechanisms.

Film thickness increases with decreasing wiper speed, but Region I has less precision due chiefly to the difficulty of controlling film volume on the necessary 100 nL level: slower speeds allow more time for volume flow from the meniscus to the forming film. While thickness scans are a typical tool for many experiments, in some a specific thickness is

required for each shot. This requirement merely extends the time between shots and can be achieved in one of two ways: one approach is to apply exactly the correct volume from a precision syringe pump through a wiper hole designed for this purpose. A second approach, and the one used here, is to start with a thicker film and reshape it with additional wiper draws.

Wiping from further above the film aperture brings additional liquid crystal from the reservoir, preferentially accessing the thicker section of a given wiper speed range. Then redrawing at a slightly higher speed (typically a few μm/s increase) effectively wipes away some smectic layers to reduce film thickness. Several redraws may be required depending on the desired accuracy–however, the rapid LSTI draws allow for multiple iterations even on shot/minute systems. Finally, smectic phase stability combined with low vapor pressure enables films formed by the LSTI to maintain their thickness nearly indefinitely, making them ideal as well for laser systems with low repetition rates of several shots per hour or day.

5.3 High Repetition Rate Devices

Laser facilities are currently under construction with repetition rates of up to 10 Hz, which will require rapid target insertion, as well as plasma mirrors. The spinning disk inserter, or SDI (shown in concept in Fig. 5.4(a)), is being developed to provide targets and optics for these new systems. By increasing the number of holes which pass a stationary wiper, the repetition rate can be increased without a one-to-one increase in the speed with which the wiper passes the aperture, so that the film formation success rate is higher. It is vital for a plasma mirror to be of good quality to preserve the mode of the reflected beam; using an absorbent wiper to form films decreases the amount of excess liquid crystal around the aperture, dramatically improving film flatness (Fig. 5.4(b)). Currently, this device is capable of forming at 3 Hz, and has been operated for up to 22 hours continuously, forming more than 200,000 films.

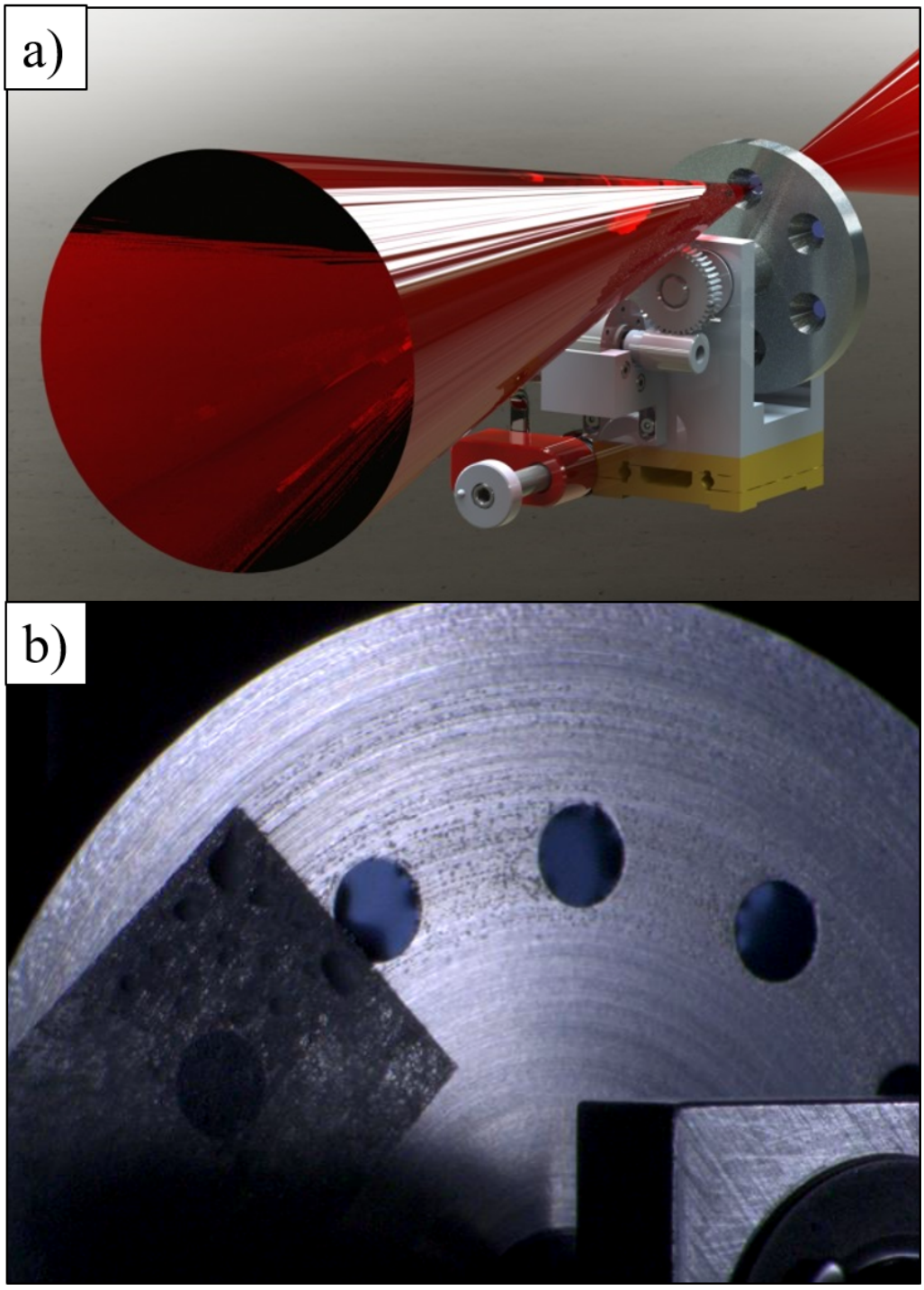

Figure 5.4: (a) The spinning disk target inserter concept. An incoming laser passes through an aperture holding a film, which is formed and characterized at other positions on the disk. Photo credit: R.J. Hanna. (b) SDI in operation using an absorbent wiper (gray). Photo credit: Anthony Zingale.

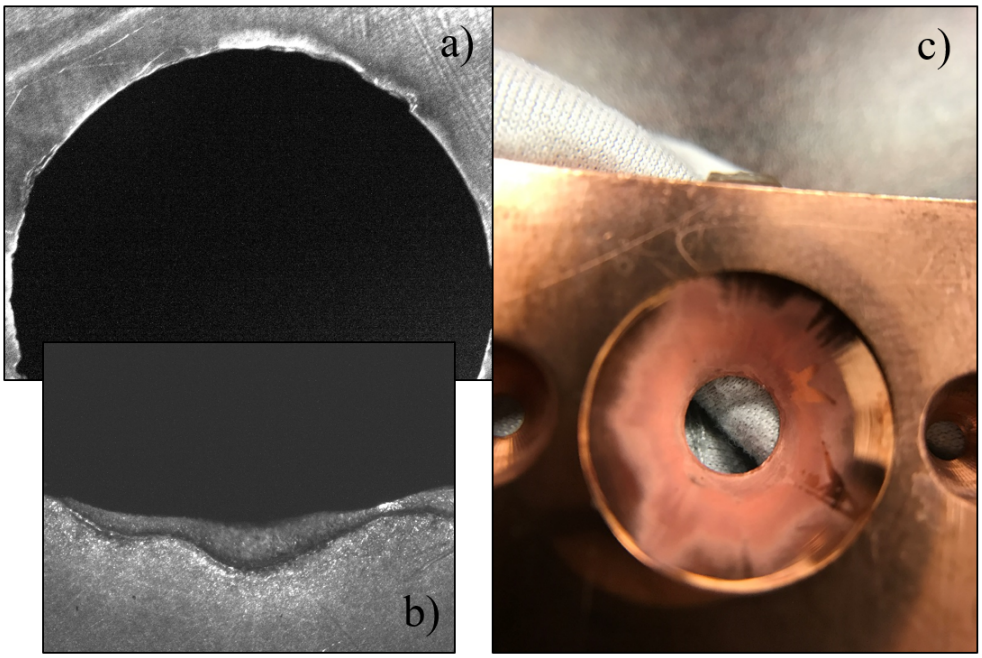

Figure 5.5: (a) Microscope image of laser-induced damage to edges of LSTI aperture. (b) Higher magnification of part of the previous image; there are two levels of edge visible, so that films cannot easily adhere to one plane and are more likely to break. (c) Accumulated aluminum debris on rear side of aperture, which contributed to aperture degradation.

5.3.1 Device Longevity in Operation

High repetition rate lasers will likely produce great amounts of debris, and it is not clear what degree of damage this will do to chamber optics. The 4 mm aperture LSTI was subject to more than 500 shots from lasers with energies up to 10 J and tight foci, with no effect on film formation. In contrast, just a few 110 J shots from the Texas Petawatt laser produced substantial damage on the aperture edges shown in Fig. 5.5, although the $\sim 20\mu$m laser focus was positioned at the center. One possible explanation is uncharacterized energy in the wings of the pulse, but it may also be that the amount of plasma produced in these shots ate away at the edges of the aperture, preventing films from being formed. A larger 11 mm device suffered much less damage – this may be a solution for yet-unforeseen problems at lasers which can produced more plasma per minute.

5.4 Liquid Crystal Waveplates

Freely suspended liquid crystal films can also be used as waveplates due to their uniaxial birefringence. The 8CB molecular arrangement results in efficient polarization rotation for light incident off normal incidence. On-demand thickness tuning allows different polarization effects to be chosen with the same setup. To demonstrate this an alignment laser was oriented through crossed cube polarizers with a LSTI placed in between, as shown in Fig. 5.6(a). The results are shown in Fig. 5.6(b), where the amount of light transmitting through the film and both polarizers is shown as a function of film thickness. For the 632 nm laser incident on the film at 58°, quarter wave rotation was observed at 4.5 μm, and half wave at 9 μm. At Brewster's angle for an 800 nm central wavelength, a 5.5 μm film is required for quarter wave rotation.

Critically, these films are true zero-order waveplates with the first quarter wave rotation occurring for films on the order of a few microns, in contrast to much thicker compound zero-order waveplates. This is necessary for short pulse polarization rotation, since even short propagation distances through media will cause nonlinear phase accumulation from the intense light that will degrade the focused laser mode. Another unusual and helpful aspect is that, unlike traditional waveplates, the films must be operated off-normal incidence to achieve birefringence, which means potentially damaging back-reflections are of no concern. The exact angle is not critical so they are easy to align. The LSTI used for this test had a 4 mm aperture, but others have been developed to accommodate larger beam sizes, up to 50 mm currently (Fig. 5.7). The ionization threshold of 8CB is relatively low compared to other materials used for optics, roughly 10^{11} W/cm^2 for a 30 fs pulse. A 1 J pulse of this duration could pass through the film without creating a plasma if expanded to a diameter of 25 cm – this is the target size for a zero-order liquid crystal waveplate.

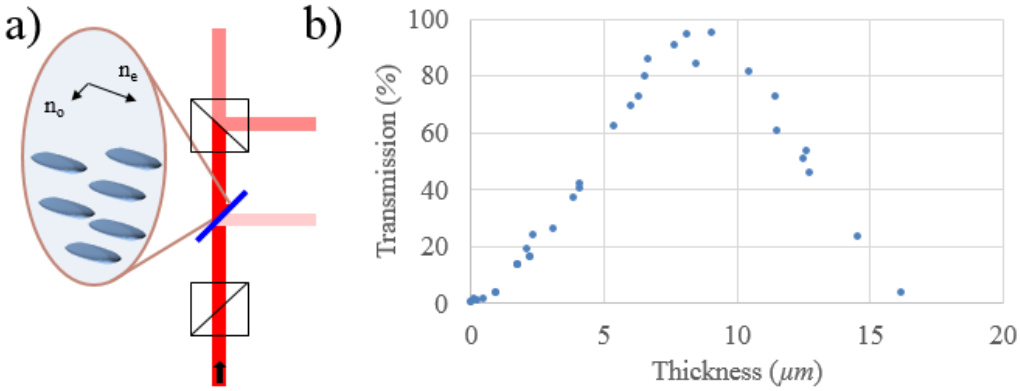

Figure 5.6: (a) Schematic of LSTI device placed between crossed polarizers. Uniaxially birefringent 8CB rotates the phase of light transmitting a film at non-normal incidence. (b) Light transmitted through these optics versus film thickness, showing quarter and half wave rotation. The laser emitted 632 nm light incident at 58°. Figure reprinted from [6].

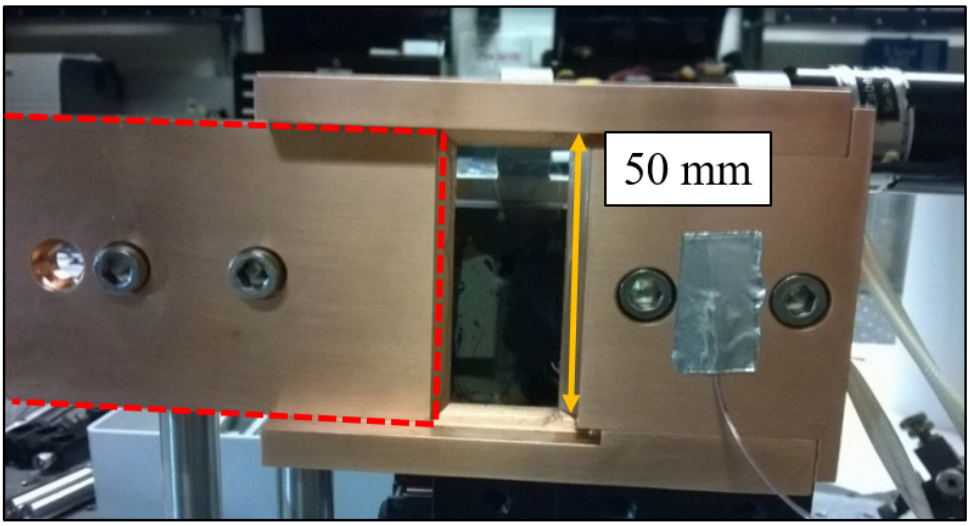

Figure 5.7: A chariot-and-rail film formation device. The piece outlined in red dashed lines is stationary, while the slide moves to the right, forming a large area film (50 mm height pictured). A thermocouple is affixed to monitor frame temperature.

Chapter 6
Modeling Contrast-Enhancing Plasma Mirrors

6.1 The Need for Contrast Enhancement

[4]Laser facilities with intensities and peak powers exceeding 10^{20}W/cm^2 and 1 PW are now available at laboratories around the world, with several new facilities under construction that will reach 10^{22} W/cm^2 and 10 PW. These intensities exceed the ionization thresholds of all materials ($\sim 10^{13}$ W/cm^2) by many orders of magnitude and therefore place strict requirements on laser intensity contrast for performing well-controlled studies. Many experiments using these lasers employ contrast enhancing plasma mirrors [102] to achieve this, allowing experiments using ultrathin targets [103] and prepulse-sensitive front surface structures. In addition to studies which characterize the plasma mirror efficiency [104, 105], efforts are underway to develop focusing plasma mirrors which increase the on-target intensity [106, 107, 108], and repetition-rate technologies that can keep up with the shot rates of new facilities [8, 109].

Ultra-intense pulse generation and amplification naturally produce several forms of prepulses ranging from ns to fs timescales prior to the main pulse. Pre-pulse light can originate as amplified spontaneous emission from high gain amplifiers, scattered reflections in multipass amplifiers or retro-reflecting optical paths, imperfect phase correction in grating compressors, and the early ramp up to peak intensity will generally occur on a timescale

[4]Much of this chapter is reprinted with permission from P. L. Poole, A. Krygier, G. E. Cochran, P. S. Foster, G. G. Scott, L. A. Wilson, J. Bailey, N. Bourgeois, C. Hernandez-Gomez, D. Neely, P. P. Rajeev, R. R. Freeman and D. W. Schumacher, Scientific Reports, vol.6, 32041 (2016) [8].

longer than the width of the main pulse itself. Though this light may be significantly less intense than the main pulse – 10^{-10} contrast or better is possible in systems designed with pulse cleaning mechanisms – pre-plasma formation sufficient to influence experimental results is commonplace. Simply assessing whether a prepulse is sufficient to modify a target is challenging due to the large dynamic range (9 orders for a peak intensity of $\sim 10^{22}$ W/cm^2) in question, and the timescales over which a measurement needs to be performed – tens of ns.

Minimizing pre-plasma is critically important for solid target experiments in many cases as hydrodynamic expansion ruins the initially sharp interface. Pre-plasma formation and related target expansion is known to impact hot electron generation [110] and the ability to control electron acceleration using recently demonstrated structured targets [111, 112] as well as the optimization of sub-micron thick target-based ion acceleration [113, 114, 55] and high-harmonic generation [112].

Figure 6.1 shows an example of laser contrast from the Scarlet laser [7] measured out to 175 ps preceeding the main pulse using a Sequoia third-order cross correlator. A scattered light prepulse is visible at -165 ps at $10^{-7.5}$ orders of magnitude, while the laser pedestal or "skirt" exceedes 10^{-9} at 25 ps. Scarlet's peak intensity on-target is 8×10^{21} W/cm^2, so either of these features will ionize a target. Laser prepulses on the ns scale have a greater effect on target evolution due to the greater time for hydrodynamic evolution, and are typically measured with an oscilloscope and fast diode, which are limited to $6-8$ orders of magnitude in dynamic range without using plasma switches or similar technique to block the main pulse. The time window between ~ 1 ns and ~ 250 ps before the main pulse is particularly difficult to characterize.

Several techniques have been developed to achieve contrast improvement, often requiring significant laser architecture overhaul making them difficult to implement on an existing facility. These include using low-gain optical parametric amplification in the laser front-end [115], using a third order process like cross polarized wave generation (XPW) [116] for pre-pulse reduction before amplification, or the installation of fast Pockels cells and spatial filters to reduce early and incoherent pre-pulses [7].

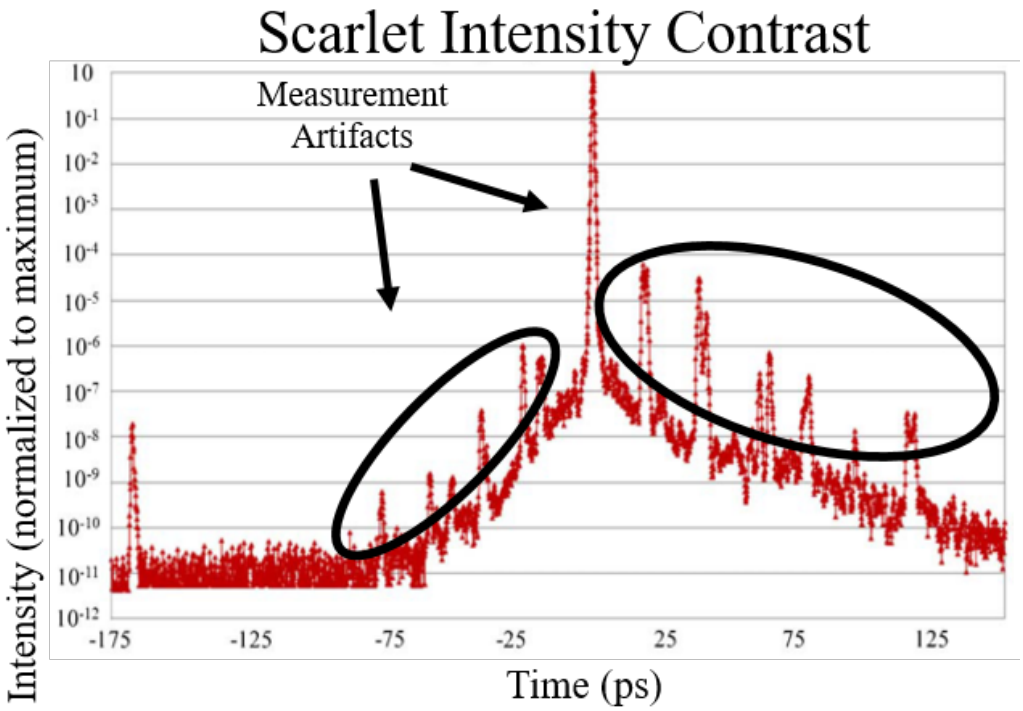

Figure 6.1: Sequoia third-order cross-correlator scan of Scarlet prepulse after cross polarized wave generation (XPW) contrast enhancement and partial amplification, where negative time values indicate light arriving prior to the main pulse. Features circled in black are known measurement artifacts. Modified from [7].

A simple and commonly used approach is the plasma mirror, schematically shown in Fig. 6.2, typically an anti-reflection (AR) coated fused silica substrate [117, 102, 118, 104, 119, 120, 121, 105]. The AR coating is critical for good pre-pulse rejection with the resulting low-field reflectance primarily determining the maximum achievable contrast enhancement. For a properly focused pulse, the preplasma will remain below the ionization threshold, but the main pulse will generate a highly reflective plasma surface with its main peak leading edge, creating an ultra-fast temporal filter that enhances intensity contrast by roughly two orders of magnitude at the cost of perhaps $\sim 25\%$ of the incident energy. This has the advantage of not requiring changes to laser architecture. However, each shot damages the affected region so the plasma mirror must be rastered to a clean area or replaced; the requisite alignment and cost remain obstacles to prolonged or high repetition rate pulse cleaning despite much progress on plasma mirror technique [102, 105, 122]. As laser facilities reach higher native repetition rates, they become limited by the ability to place a fresh plasma mirror in the way of the beam. A possible alternative is the liquid jet plasma mirror [121], but it has not yet demonstrated appropriate low-field reflectance due to the lack of an AR coating. Also, such jets currently have the downside of producing a high vapor pressure that will degrade a high intensity short pulse.

Another application for high-repetition rate plasma mirrors is beam redirection for staged electron acceleration. Electrons can be accelerated to progressively higher energies by interaction with a series of laser pulses,but these staged beams need to be switched in and out of the line of acceleration in order to optimize each stage and protect downstream apparatus [123]. Currently this has been done with a VHS tape based plasma mirror, which spools the tape between two motors [109]; however, the jitter in a spooled tape design can cause undesirable variations in reflected laser pointing and intensity An additional consideration is the 15 μm thickness of the tape, which increases the divergence of the electron beam passing through it – a thinner target would reduce this.

The following sections discuss the solution we developed, the liquid crystal plasma mirror (LCPM). Section 6.2 will overview a proof-of-principle experiment testing LCPMs, and PIC simulations developed to include the physics needed to model them will be covered in Sec.

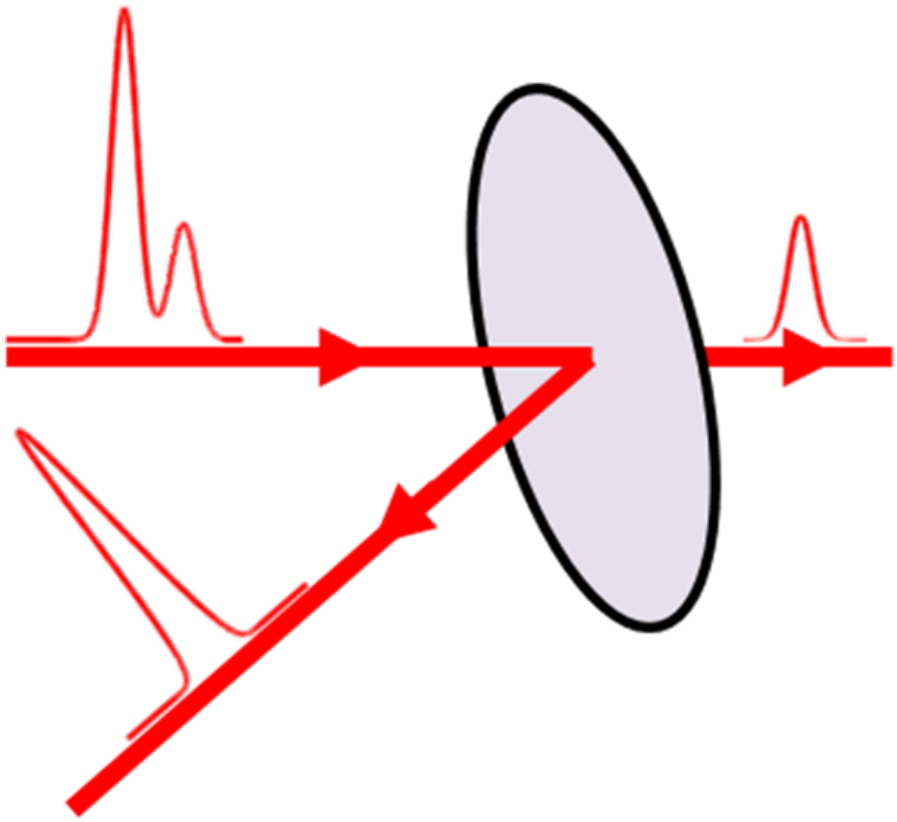

Figure 6.2: Schematic of pulse-cleaning plasma mirror operation. A high intensity main pulse, preceded in time by a lower intensity prepulse, is incident on an anti-reflection coated dielectric. This optic is placed at the appropriate distance with respect to the focusing geometry of the incoming beam so that the prepulse is below the ionization threshold and transmits. The leading edge of the main pulse ionizes the surface when it arrives, creating a plasma which reflects it.

6.3.

6.2 Experimental Implementation with Liquid Crystals

An efficient plasma mirror will transmit as much prepulse as possible, with minimal losses once the plasma mirror ionizes and reflects the main pulse. The maximum possible contrast enhancement is often characterized by R_{high}/R_{low}, the ratio of high field reflectivity to low field reflectivity. The actual contrast enhancement depends on the structure of the prepulse itself. For conventional plasma mirrors, this is typically between two and three

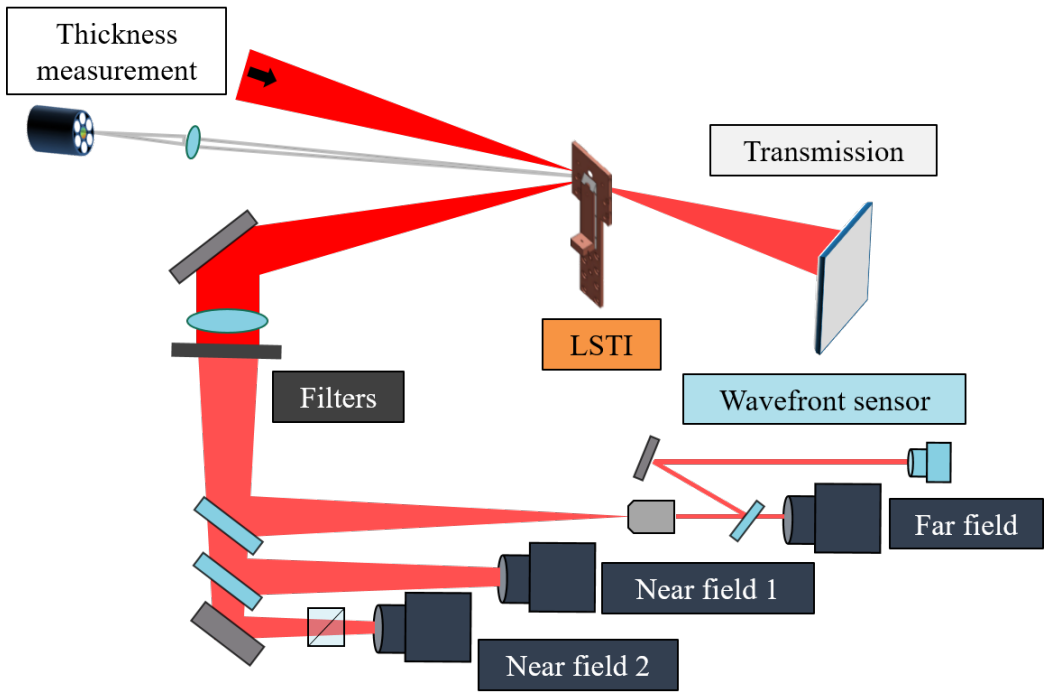

Figure 6.3: Experimental setup used to test liquid crystal plasma mirrors (LCPM) at the Astra laser facility. Amount of transmitted light and reflected near- and far-field were collected from plasma mirrors as a function of incident intensity, as well as the thickness of the liquid crystal film used. Described in more detail in the text. Figure reprinted from [8].

orders of magnitude. In order to evaluate LCPM efficiency, both the low field and high field reflectivity were measured.

6.2.1 Low Field Characterization

Liquid crystal films can be optimized for plasma mirror use by selecting the thickness that minimizes low-field reflectance for a given laser wavelength and incidence angle. The low-field reflectance of a thin film etalon is

$$R = 1 - \frac{1}{1 + F sin^2\left(\Delta/2\right)}, \text{ for } \Delta = \frac{4\pi}{\lambda} nd\cos\left(\theta_t\right), \tag{6.1}$$

where F is the Fresnel reflection coefficient, λ is the laser wavelength, n is the index of refraction, d is the film thickness, and θ_t is the light angle after first surface transmission.

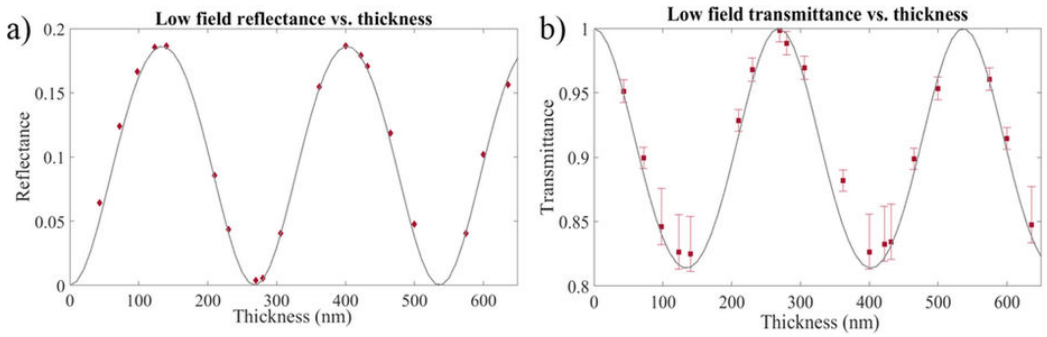

Figure 6.4: Low field reflectance (a) and transmittance (b) as a function of film thickness. Red points are experimental data, mapped over a black curve plotting Eq. 6.1 (a) and 1 minus that quantity (b). Figure reprinted from [8].

We used the liquid crystal 8CB ($C_{21}H_{25}N$) whose molecules are uniaxial with the crystal axis pointing along the film normal, so S and P polarized light will experience different reflection coefficients and indices of refraction ($n_e = 1.73$ and $n_o = 1.53$ for 8CB at $28°C$ [124]) and as such require slightly different optimal thicknesses for pre-pulse rejection.

A series of shots were taken with S-polarized light and relatively low intensity ($I = 10^{11}\text{W/cm}^2$) to measure the liquid crystal reflectance below the ionization threshold. The vacuum chamber setup with diagnostics can be seen in Fig. 6.3. Figure 6.4 shows the low-field reflectance as a function of liquid crystal thickness plotted over the curve given by Eq. 6.1. Error bars (smaller than the data point for the reflectance graph) come primarily from inconsistencies in the camera filtering used on the measurements. For the parameters used here the ideal film thickness is 270 nm which corresponds to $< 0.2\%$ reflected light– this is similar to typical results on ion beam sputter-coated slides and superior to those coated with vapor deposition [125]. Of note is the low reflectance also possible with < 30 nm films–while tuning to precisely 270 $\pm$10 nm takes several wipes with the current linear sliding target inserter (LSTI) film formation device [6], the properties of liquid crystal cause them to preferentially form films of < 30 nm thickness when the wiper speed is above a certain value. This means that rapid low reflectance films are readily available with the current technology, and more robust pre-pulse reduction can be achieved with longer film thickness adjustments.

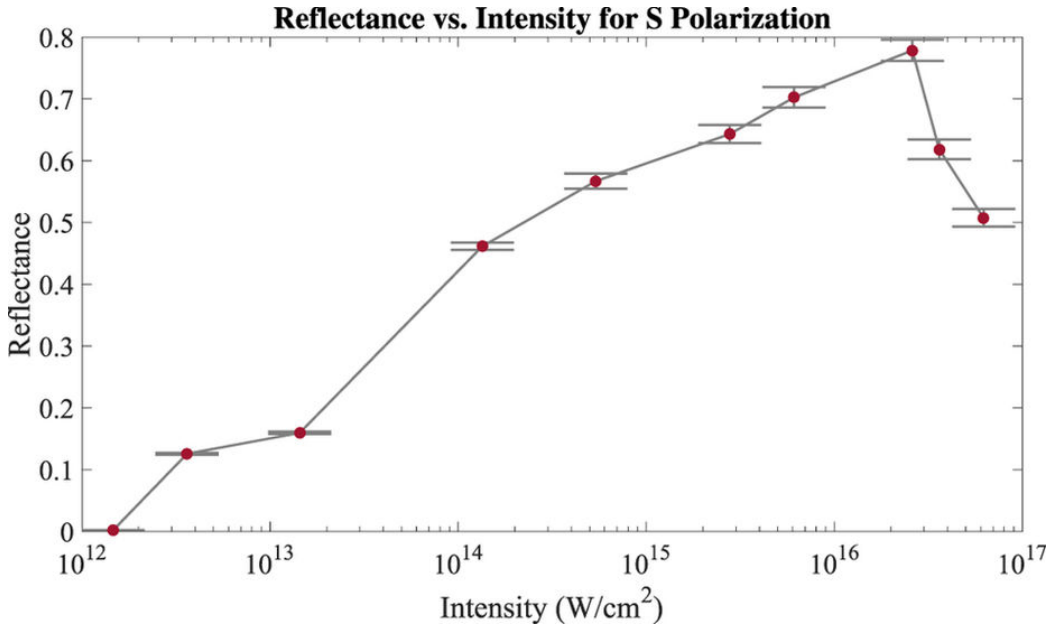

Figure 6.5: Integrated reflectance as a function of laser intensity for s-polarized light. The maximum reflectance – 0.75 – occurs at $I = 2 \times 10^{16}$ W/cm^2. Figure reprinted from [8].

6.2.2 High Field Characterization

The plasma mirror reflectance testing was performed on the Astra laser [126] at the Central Laser Facility, which is a 0.6 J, 0.1 Hz titanium:sapphire based system with 40 fs pulse duration. The 100 mm FWHM diameter beam was focused by an $F/7$ off axis parabola onto the LSTI-formed liquid crystal film, where the position could be varied to adjust the incident intensity. The laser wavelength was centered on 800 nm, and the angle of incidence onto the liquid crystal film was 15°, so the optimum thickness for pre-pulse rejection based on the angle-dependent index of refraction was 270 nm. A ground glass scatter screen was placed behind the LSTI to intercept transmitted light, observed with a 12-bit Andor CCD camera.

Reflectance of S polarized light at a range of intensities is shown in Fig. 6.5. Here the error bars result from uncertainties in the filters used in the various cameras, each of which was calibrated with spectrophotometry measurements after the experiment. Maximum reflectance occurs near intensities of 1×10^{16}W/cm^2, similar to other materials [102, 122]. The

Table 6.1: LCPM PIC simulation parameters. λ is the laser wavelength, τ the FWHM pulse duration, ϕ the beam waist, θ_i the incidence angle, T_e the electron temperature, ρ the species density, n the index of refraction, and Δx and Δz the cell sizes.

Laser		Target		Numerics	
I_0 (W/cm^2)	$5 \times 10^{12-16}$	d(nm)	270	explicit, absorbing BCs	
λ (nm)	800	T_e (eV)	1	$\Delta x \times \Delta z$ (nm)	2.5 × 3
τ (fs)	60	ρ_H (/cm^3)	5.35×10^{22}	particles/cell	10
$\phi(\mu m)$	1.2	ρ_C (/cm^3)	4.33×10^{22}	Courant ratio	0.75
θ_i	16°	n	1.53	dim.	2D3V
pol.	S (Y-dir)	vac. gap (μm)	4	Spitz. rate (Hz)	$0.5\text{-}2 \times 10^{16}$

S polarized reflectance is 75% for the optimum incident intensity, comparable to conventional fused silica plasma mirrors.

The actual contrast enhancement from a dielectric plasma mirror depends on the specific nature of the laser pre-pulse and the resulting plasma dynamics. However, as is commonly done, we can estimate the enhancement by taking the ratio of the peak high field reflectance to the low field (non-ionizing) reflectance. The resulting ratio for a single liquid crystal plasma mirror exceeds 350. Thus, a dual plasma mirror system would in principle yield a contrast enhancement exceeding five orders of magnitude while still retaining >50% transmission of the incident laser energy. Additionally, unlike conventional systems, liquid crystal plasma mirror operation can be continued indefinitely and at low cost using a LSTI or similar device with occasional reservoir resupply.

6.3 Particle-In-Cell Modeling of LCPMs

6.3.1 PIC Platform Development for LCPMs

Particle-in-cell (PIC) simulations are commonly used to analyze and optimize plasma mirror operation for high harmonic generation from metals [119, 127, 128, 129] and have played a critical role in the development of that field. PIC simulations have not played an equivalent role in the study of plasma mirror operation for pulse cleaning from dielectric plasma mirrors (DPMs), however, due to the unique challenges involved; several simplifying assumptions typically made to arrive at interpretable results with reasonable computational cost for the

former case would invalidate a simulation for the latter. In particular, the initial state of the dielectric substrate, photoionization, and collisions within the resulting plasma play a crucial role.

PIC simulations using metal substrates as targets or plasma mirrors are typically initialized as a singly or multiply ionized plasma to mimic the properties of the conductor and because the substrate is expected to be rapidly heated by the laser pulse. Doing this for a DPM would begin the simulation with the plasma mirror in its "on" (highly reflective) state, completely omitting the pulse cleaning operation. Instead, DPMs must be modeled using neutral particles which can subsequently be photoionized [130]. Further, the basic PIC algorithm is fundamental and emergent properties such as reflectivity (or thermal conductivity, resistivity, etc.) cannot simply be set at some value. A proper treatment of the low-field response requires modeling the dielectric response of this neutral system. The impinging light must reflect (with appropriate phase shifts), refract, and transmit so that the etalon response is correctly modeled: at the proper thickness for minimum etalon reflection, the multiple reflections from the front and back surfaces of the film must destructively interfere. Next, as the intensity increases, the neutral particles must ionize to produce the plasma that will cause DPM reflection once the density is high enough, approximately at the critical density $n_c = 1.75 \times 10^{21}/\text{cm}^3$ for 800nm light. The central, most intense region of the laser beam will reach this threshold first with the spatial wings reflecting later or not at all and this can affect the outgoing spatial mode and so must also be modeled. Sufficient intensity for the spatial mode wings to reach critical density can cause the significantly higher intensity central region to form a highly overdense plasma which will affect the subsequent laser-plasma interaction. Finally, the primary loss mechanism is via absorption in the evolving plasma. Although the transmitted light contains the pre-pulse, the total energy of the pre-pulse is generally quite small. A variety of absorption mechanisms such as inverse-Bremsstrahlung or Brunel heating can be at play, depending on how long the pulse is and the specific plasma conditions that arise [131]. Collisions within the plasma must be modeled for some of these mechanisms as they cause the electrons to dephase from the driving laser field and to heat the growing plasma. In summary, from before the onset

of significant ionization to well above the threshold for turning the DPM on, a simulation must correctly treat five orders of magnitude variation in intensity or more.

PIC simulations of LCPMs are presented in the following sections that, to our knowledge for the first time, correctly capture a plasma mirror as a dielectric, as a growing plasma, and in its reflective state. This work was done using the code LSP [57]. These simulations begin with 8CB represented as relatively cold neutral atoms (1 eV) which are ionized by a laser matching the parameters of Astra and varying in intensity between 2×10^{12}W/cm^2 and 5×10^{16}W/cm^2. Detailed simulation parameters are listed in Table 6.1.

This discussion will focus on the novel aspects of this simulation framework necessary for capturing the physics relevant to plasma mirror operation. The low field behavior, i.e. the interaction of the leading edge of the pulse with the dielectric, is crucial to determining the efficacy of contrast enhancement. In addition to starting with neutral atoms, a dielectric model was implemented (Sec. 6.3.2). These simulations were performed in 2D3V, which affects the spatial intensity distribution with respect to what would be found experiment - an approximation to correct this is discussed in Sec. 6.3.3. Next, the ionization model used will determine when the plasma mirror turns on, and thus the degree of contrast enhancement. Determining and implementing the correct ionization model is addressed in Sec. 6.3.4. Finally, collisional losses are important to include in this model, but ideal plasma collision rates are not well suited for these plasma conditions - some possible improvements are discussed in Sec. 6.3.5).

6.3.2 Low Field Behavior

The low field reflectivity of a plasma mirror is vital to model correctly, as otherwise the degree of transmission of the laser's leading edge will not be captured. LSP incorporates a spatially varying dielectric model which was used to overlay the LCPM region with an $n = 1.53$ block to properly model the thin film reflection characteristics. Figure 6.6(a) shows this model interacting with the laser electric field at the time the peak of the pulse reaches the target without any atoms present to ionize; the light is predominantly transmitted. In Fig. 6.6(b), the laser is shown at the same point in time, having reflected from a plasma

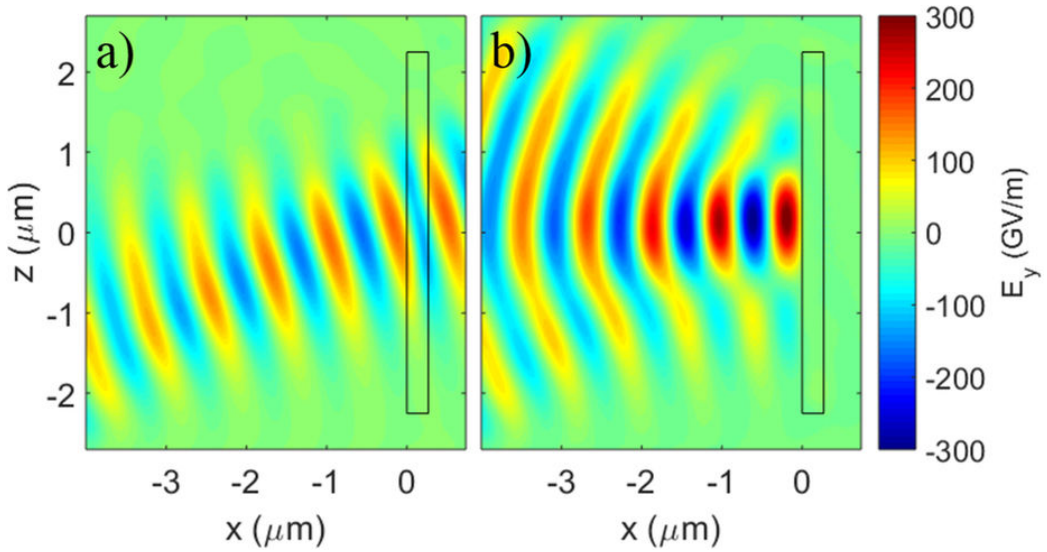

Figure 6.6: (a) The simulation target thickness is tuned for Fresnel anti-reflection in the low-field limit for the index of refraction of the liquid crystal 8CB, using LSPs dielectric model. The electric field at the time of the peak of the pulse in the polarization direction is plotted as the laser refracts in the target (black rectangle). (b) The same grid area is initially populated with neutral particles which ionize, exhibiting high-field plasma reflectivity. The laser pulse at the same time in this case is now predominantly reflected. Figure reprinted from [8].

generated when neutral atoms were introduced and ionized. The amount of reflected light was determined by measuring the field flux normal to the laser outlet boundary. For a target thickness of 270 nm, the low-field reflectance in the simulation was observed to be 0.2%, in agreement with experiment.

6.3.3 Dimensionality

These simulations were performed in 2D3V due to the wide range of simulation options which were investigated, and the large number of different laser intensities that had to be tested to validate the simulation against the experimental data. While 2D simulations can provide valuable qualitative insight in many cases, they often fall short when quantitative agreement is desired. Here, the intensity falloff of the laser beam in the simulation's virtual dimension (the dimension normal to the 2D grid) is neglected by a 2D simulation,

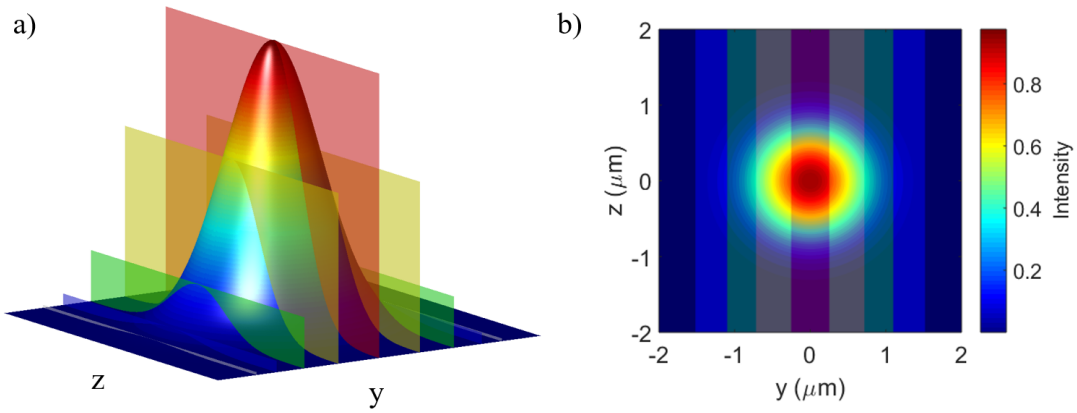

Figure 6.7: Representation of the correction method for simulation dimensionality. (a) An intensity distribution with Y and Z dependence is not well approximated by any one 2D line beam (colored slices). (b) Topdown view of intensity distribution, showing the individual 2D3V simulation slices which contribute to the full beam schematically. In practice, simulations were used at varying intensity to construct the reflectivity contributions at 14 intensity slices. In this depiction, X is the propagation direction of the laser.

overestimating the reflectivity in these regions.

A 3D approximation was achieved by treating each 2D3V simulation as a slice of the 3D pulse profile (Fig. 6.7(a) and (b)) and several such runs were summed over, weighted by their fractional contribution to the total pulse energy. This took into account the shape of the beam in three dimensions, integrating out to 20 times the beam waist in the full dimension. The equation used to find the 3D reflectivity was

$$R_{3D} = \frac{\sum_n R_{2D,n} \int_{y_{n-1}}^{y_n} I(y)dy}{\sum(I(y))}, \tag{6.2}$$

for the 2D simulation reflectivities $R_{2D,n}$ and spatial intensity distributions $I(y)$. The Y dimension of the beam, taken from $0 - 5\omega_0$, is divided into sections based on the number of simulations, so that $y_n = 5\omega_0/14 \times n$ for $n = 0$ to 14. Without this 3D correction, the simulation results would have been too high by about 5% at the highest intensities and more at lower intensities, indicating 3D effects are also significant.

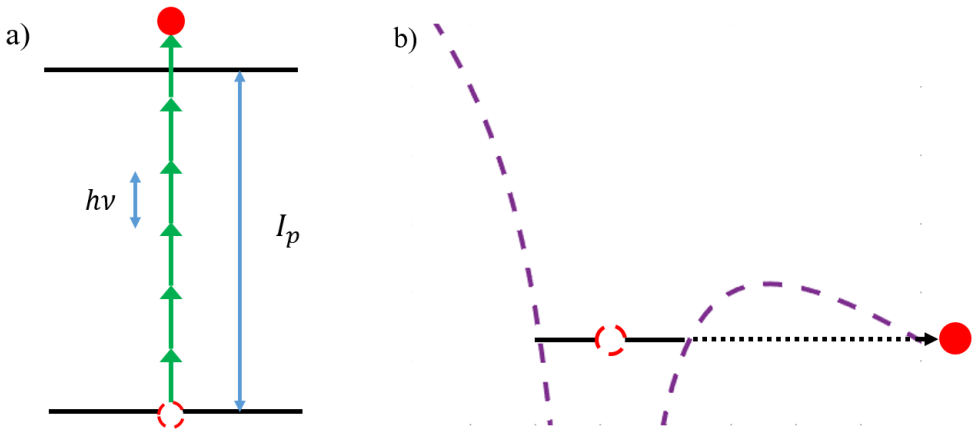

Figure 6.8: (a) Multiphoton ionization cartoon. The electron (red) is promoted from its groundstate to the continuum over ionization potential I_p by N photons whose collective energy is enough to overcome the potential well. (b) Tunneling ionization cartoon. An atom's potential well (purple) is deformed by the presence of an external electric field. For sufficient depression, the electron (red) has a significant probability of tunneling through the well.

6.3.4 Ionization Model

The ionization mechanism by which an LCPM transitions from transparent dielectric to reflecting plasma, and at what time this happens with respect to the rising edge of the pulse, are critical for correctly modeling not only the reflected energy typically measured, but aspects such as pulse shortening that are more difficult to capture. Two limiting cases for possible photoionization mechanisms are multiphoton ionization (MPI) and tunneling ionization. Figure 6.8 shows the processes by which ionization takes place in these models. In MPI, the ionization potential of an electron is overcome by several photons imparting their energy to the electron, allowing it to escape into the continuum, if the photon density is sufficient. The MPI ionization rate can be approximated as [132]

$$\Gamma_{N_{MPI}} = \sigma_{N_{MPI}} I_L^{N_{MPI}}, \tag{6.3}$$

where $\Gamma_{N_{MPI}}$ is the rate of electron ionization, which requires $N_{MPI} = int(I_p/(h\nu))$ photons, I_L is the incident laser intensity, and $\sigma_{N_{MPI}}$ is a coefficient.

Table 6.2: Relevant ion/molecular charge states for 8CB. Ionization potentials are given, as well as appearance intensities for that charge state, Keldysh parameter at appearance intensity, and number of photons required for MPI with 800 nm light. Ionization potentials taken from [23, 24].

Species	I_p (eV)	I_{app} (W/cm^2)	$\gamma(I_{app})$	N_{MPI} (800 nm)
C^{1+}	11.26	6.4 $\times 10^{13}$	1.2	8
C^{2+}	24.38	3.5 $\times 10^{14}$	0.8	16
H^+	13.6	1.4 $\times 10^{14}$	0.9	9
$C_6H_6^+$	9.24	2.9 $\times 10^{13}$	1.6	6

Tunneling ionization takes place when the electric field of the laser deforms the atom's potential well, allowing an electron to tunnel through the depressed potential with some finite probability. For hydrogen-like ions, the rate of tunneling ionization can be expressed as [133]

$$\Gamma_{tunnel} \propto \frac{(I_p)^{5/2}}{I_L^{1/2}} e^{-2/3(I_p)^{3/2}/{I_L}^{1/2}}. \tag{6.4}$$

More elaborate formulations such as the Ammosov-Delone-Krainov (ADK) model [134] take into account more complex ions.

In the limit where the height of the barrier drops below the ionization potential, the probability of ionization goes to 1 – this is known as barrier suppression ionization (BSI). The appearance intensity at which BSI takes place can be estimated as follows [135]:

$$I_{app} = \frac{c\epsilon_o(4\pi\epsilon_o)^2}{32Z^2e^6} I_p^4, \tag{6.5}$$

where Z is the ion charge state after ionization, I_p is the ionization potential, c is the speed of light, and e the fundamental charge. 8CB is mostly hydrogen and carbon with appearance intensities of 1.4 $\times$ 10^{14} W/cm^2 and 6.4 $\times$ 10^{13} W/cm^2, respectively.

The Keldysh parameter [133], $\gamma = \sqrt{\frac{I_p}{2\Phi}}$ where $\Phi = e^2E^2/(4m\omega^2)$ is the ponderomotive potential, provides a figure-of-merit for which ionization mechanism dominates. Typically it is required that $\gamma \approx 0.5$ or lower for tunneling rates to apply [136].

Since 8CB is predominantly composed of hydrogen and carbon[5], the appearance inten-

[5]The ionization potentials of molecular 8CB are not well known; however, the first ionization level of

sities of the first charge states for these atoms and Keldysh parameters at these intensities determine which ionization model is appropriate for the LCPM turnon. Table 6.2 lists the Keldysh parameters at appearance intensity for C^{1+}, C^{2+}, and H^+ and 800 nm light. For all these charge states, $\gamma \geq 0.8$, suggesting an LCPM composed of these constituents will operate in the MPI regime. This will generally be the case for any dielectric based plasma mirror. Typically intensities up to or above 10^{16} W/cm^2 will be present during the operation of an LCPM, but ionization of hydrogen and carbon will have saturated well before these intensities are reached such that significant tunneling may never occur. Thus, there will be a significantly overdense plasma near the center of the spot with multiple species present whereas underdense plasma with only first stage ionization contributing will be present farther from the central spot.

Tunneling models such as the ADK model will greatly understate the ionization rates in the MPI regime, but use of MPI models in PIC in uncommon for ultraintense laser simulations. To our knowledge, there is not a well established MPI model for these conditions. Accordingly, an MPI model [132] was added to LSP, where the ionization rate $P = (CE)^{2N_{MPI}}$ with an adjustable rate coefficient C, where E is the laser electric field and N_{MPI} is the minimum number of photons required for photoionization. The MPI coefficient of $C = 1 \times 10^{-9}$ cm/kV was chosen by matching the reflectance at a single data point, the lowest intensity, and then using this for the rest of the intensity curve. Equation 6.3 is based on intensity, not instantaneous electric field, and so the formulation implemented here in LSP will not have the same time dependence within a laser cycle. However, the correct intensity dependence is achieved, which is the relevant physics for this problem.

6.3.5 Low Temperature Collisions

PIC simulations do not represent close-range physics such as particle collisions due to finite cell size or, equivalently, the particle shape, and so when the problem calls for it these effects must be added back in to the basic PIC cycle. These simulations use LSP's implementation

benzene, $C_6H_6^+$, which is present in 8CB, has been measured. Table 6.2 shows that it has an even higher Keldysh parameter at appearance intensity, suggest that 8CB itself would also fall in the MPI regime.

of the Jones scattering model [137], which assumes a scattering "field" calculated from the average velocity and temperature of species (assumed to be Maxwellian), avoiding the need to calculate individual collisions between particles. Particle velocities are then modified by this field according to a collision rate. Most PIC codes which include collision models use the Spitzer collision rate [138], which considers collisions in a hot dilute plasma:

$$\nu_{ei} = 4\sqrt{2\pi}\frac{Z^2}{3\sqrt{m_e}}\left(\frac{e^2}{4\pi\epsilon_0}\right)^2 \frac{n_i \ln\Lambda}{T_e^{1/2}}, \tag{6.6}$$

where n_i is the ion density, Z is the ionization state, T_e is the electron temperature, and Λ is the Coulomb logarithm – $\ln\Lambda$ is commonly taken to be 16. This is valid in the case of a hot dilute plasma, where there are many particles in the Debye sphere. In the conditions needed to model the transition from neutral atoms to ionization in 8CB, it is necessary to have an electron density up to $n_e = 3.3\times10^{23}/\mathrm{cm}^3$, at a temperature initially < 10 eV to avoid ionization before the laser arrives. Temperatures under 225 eV at this density result in fewer than 10 electrons per Debye sphere, while temperatures under 1035 eV have fewer than 100 particles. In the low temperature limit, the Spitzer rate is inaccurate – if the standard $\ln\Lambda = 16$ assumption is used, the rate continues to increase as temperature drops, and other forms of $\ln\Lambda$ cause the collision rate to turn negative under a certain temperature. The simplest way to avoid this is by capping the collision rate at some value ν_{max}, coarsely mimicking the the saturation of the rate that actually takes place. Above a transition temperature T_0, the normal Spitzer model is used, and below T_0 the collision frequency is constant at ν_{max} (Eq. 6.7).

$$\nu_{ei}[T_e] = \begin{cases} \nu Spitzer[T_e] & T_e > T_0 \\ \nu_{max} & T_e \leq T_0 \end{cases} \tag{6.7}$$

In this work, different values of ν_{max} were tested for their effects on low-intensity reflectivity. As Fig. 6.9 shows, below a laser intensity of 10^{14} W/cm^2, the reflectivity was nearly constant for a given ν_{max}, with little effect on the reflectivity behavior above 10^{15} W/cm^2. For this work, $\nu_{max} = 5\times10^{15}$ Hz, corresponding to $T_0 \simeq 696$ eV, or roughly 55 electrons per Debye sphere. This is well resolved by the timestep chosen for the simulation, but acts

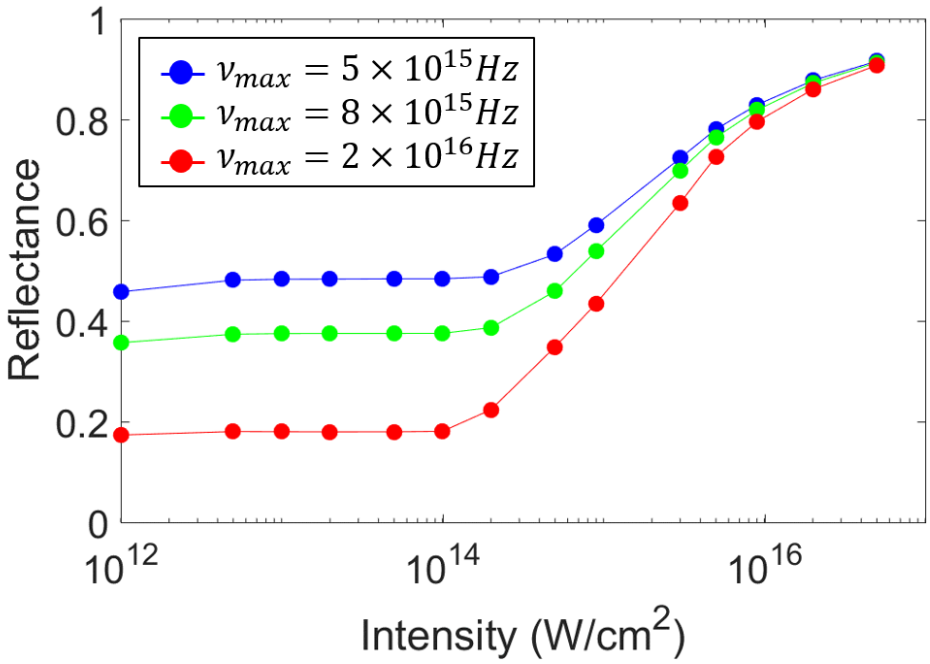

Figure 6.9: Effect of varying collision rate cap ν_{max} on reflectance as a function of intensity. In the low field limit ($I < 10^{15}$ W/cm^2), the reflectance is constant for a given ν_{max}, and increases as ν_{max} decreases. At higher intensities, the difference as a function of ν_{max} becomes negligible. Simulation parameters follow Table 6.1.

mainly as a tuning parameter here, chosen in concert with the MPI coefficient to give the best match to experiment. Two physically motivated possibilities for ν_{max} are discussed below, and will be investigated in future work.

Alternate Collision Rate Caps

When Debye shielding is no longer a valid model, a more useful scale length is the inter-particle spacing. This can be used as a surrogate for the average mean free path between particle collisions – for electron-ion collisions, this is $\lambda_{mfp} \sim (n_i)^{-1/3}$. The average time an electron takes to travel λ_{mfp} is $\tau_{mfp} = \lambda_{mfp}/v_{th}$, where $v_{th} = \sqrt{3k_B T_e/m_e}$. Using this approximation, $\nu_{max} = 1/\tau_{mfp}$, which is $\sim 3 \times 10^{15}$ Hz for LCPM temperature and density. For $n_i = 5.5 \times 10^{22}/\text{cm}^3$, $T_0 \sim 1035$ eV.

As the plasma temperature goes to 0, degeneracy determines the characteristic (Fermi) energy of the electrons $E_F = \hbar^2/(2m_e)\left(3\pi^2 n_e\right)^{2/3}$. Setting $T_0/(m_e c^2) \sim E_F$ yields a much higher collision rate cap – this is the approach used in Ref. [139]. In this model, $T_0 \sim 18$ eV for $n_e = 3.3 \times 10^{23}/\text{cm}^3$, with $\nu_{max} = 6.5 \times 10^{16}$ Hz. This approximation would require a much smaller simulation timestep.

6.3.6 Results

Figure 6.11 shows the experimental S polarization data along with three simulation curves using different models. Collisionality and the choice of ionization model are seen to have a large effect on the simulation results, illustrating the importance of these models. The ADK tunneling model (green squares) drastically underestimates the onset of plasma mirror reflection, as expected. It does better at high intensities, but this is because it eventually saturates the ionization of hydrogen and carbon, even if not at the correct intensities. Using an MPI ionization model with $C = 1 \times 10^{-9}$ cm/kV and collisions with $\nu_{max} = 5 \times 10^{15}$ Hz yields in an excellent match to experiment (black diamonds vs. red triangles) over three orders of magnitude in intensity. The importance of modeling a collisional plasma can be seen by turning the collisional model off. These results (blue diamonds) overestimate the reflectance by 25% or more, indicating the degree of loss due to excitation of the temporally

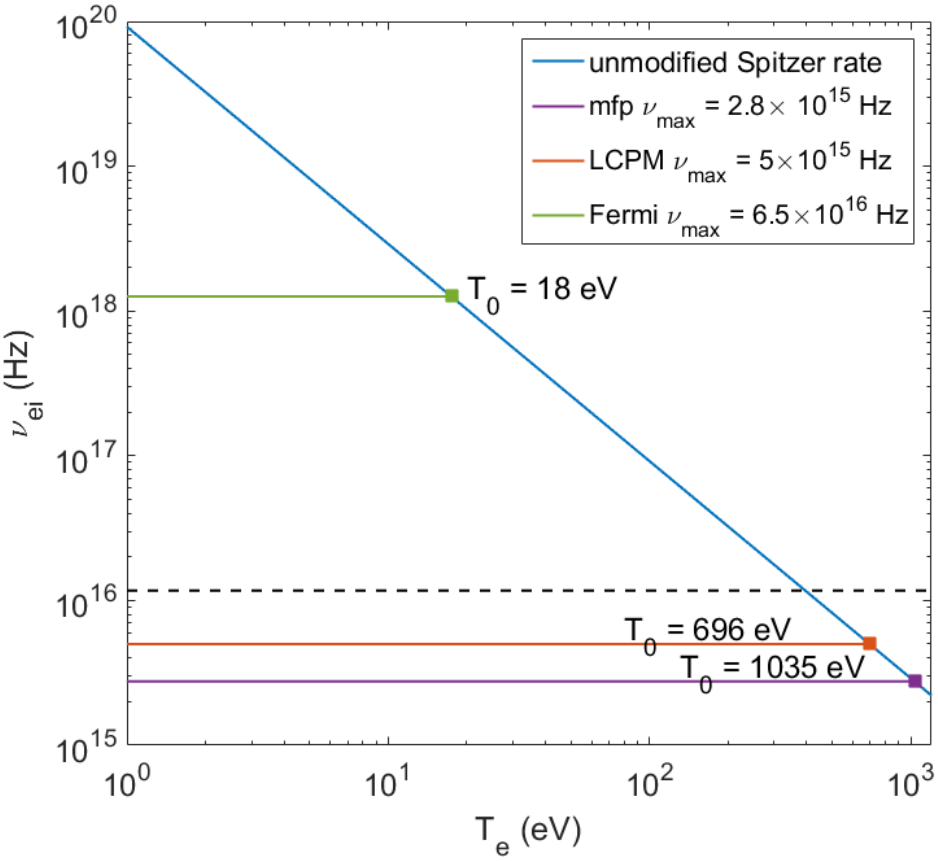

Figure 6.10: Spitzer collision rate (blue) as a function of plasma temperature T_e, and potential cutoff temperatures and maximum collision frequencies to address its low temperature shortcomings. Mean free path based ν_{max} (purple), Fermi energy based ν_{max} (green), and $\nu_{max} = 5 \times 10^{15}$ Hz (orange), the value used for the LCPM simulations. Frequencies above the dashed line cannot be resolved by the simulation timestep used here.

and spatially varying plasma layer.

The rapid decrease in reflectivity beginning at 5×10^{16} W/cm^2 is a interesting feature. Similar trends as a function of laser intensity have been observed in other experiments measuring energy absorption [35, 102]. In some experiments, the rollover intensity is $\sim 10^{18}$ W/cm^2, which points toward a relativistic source for the reflectivity change, but the reflectivity drop occurs at about an order of magnitude too low with LCPMs for this to contribute.

A few non-relativistic mechanisms could be responsible for this rollover. Inverse bremstrahlung (IB) absorption, where an electron absorbs a photon during a collision with an ion, can take place in preplasma up to the critical density and has been shown [140] to have an absorption coefficient $\eta_{IB} = 1 - \exp(-32/15\nu_{ei}(n_{cr}L_n/c))$, where L_n is the preplasma scalelength. η_{IB} is large for laser intensities up to 10^{17} W/cm^2, for low temperature plasmas, and for large L_n [141]. Another potential contributing mechanism is sheath-transit absorption (STA) [142], more commonly known as the anomalous skin effect (ASE) [143] and sheath inverse bremsstrahlung (SIB) [144], its two limiting cases. When $v_{th}/\nu_{ei} > \delta_s$, the plasma skin depth, electrons can travel out of the skin depth, carrying laser energy away into the plasma bulk. STA is an important process for steep plasma gradients [131]. It is difficult to be certain which of these mechanisms is more likely to have been responsible since preplasma was not measured in the LCPM experiment, but it seems probable that the L_n was small – the laser was defocused for this experiment, and any prepulses likely transmitted through the target without ionizing.

Whether STA or IB is responsible, a recent paper by Kemp and Divol [145] may shed light on why these simulations did not follow the experimental trend in reflectivity above $\sim 5 \times 10^{16}$ W/cm^2. In that work, it was shown to be necessary to resolve δ_s with 5-50 cells per skin depth in order to capture how laser energy is transmitted from the skin depth into the bulk of the target, where $\delta_s/\Delta x = 3.7$ for the LCPM simulations. Another potential source of error is under-resolving the Debye length. During one of these simulations, the density can reach several hundred times critical density and temperatures as high as 100 eV. Although the simulation was numerically stable to Debye heating effects, absorption

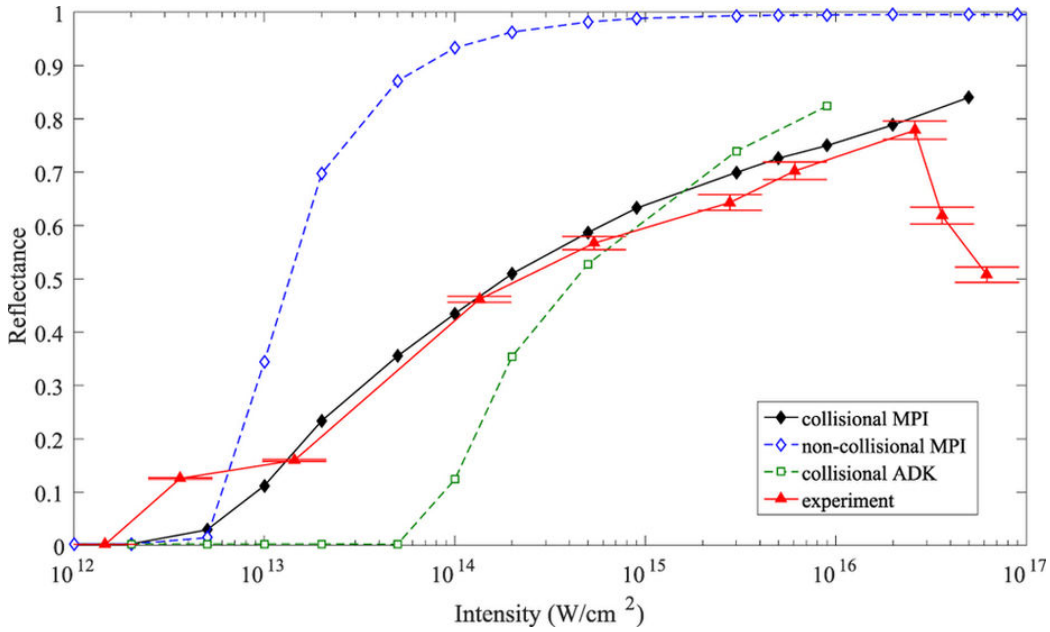

Figure 6.11: S polarization reflectance curves obtained from LSP PIC simulations. An MPI model is required to capture plasma mirror turn-on and a collisional plasma must be modeled to include plasma losses (black compared to green curves). The experimental results are reproduced for comparison (red). Figure reprinted from [8].

processes may require that this length is resolved. However, over the orders of magnitude responsible for plasma mirror agreement, the agreement between simulation and experiment is of a level rarely reached in this field.

6.4 Future Work

The framework developed here for modeling plasma mirror behavior may prove useful for designing better plasma mirrors, as well as for determining the temporal profile of the laser pulse that hits a target. Two effects of particular importance are pulse shortening and the quality of the reflected laser mode, which may mar the laser focal spot – a technique has been developed [146] to use electric field point probes to reconstruct the far field intensity distribution using the Fresnel propagator, although this may require a larger grid in order to allow the incident and reflected beams to be spatially separated. An initial qualitative analysis of pulse shortening has been performed in 2D for $I = 5 \times 10^{15}$ W/cm^2, shown in

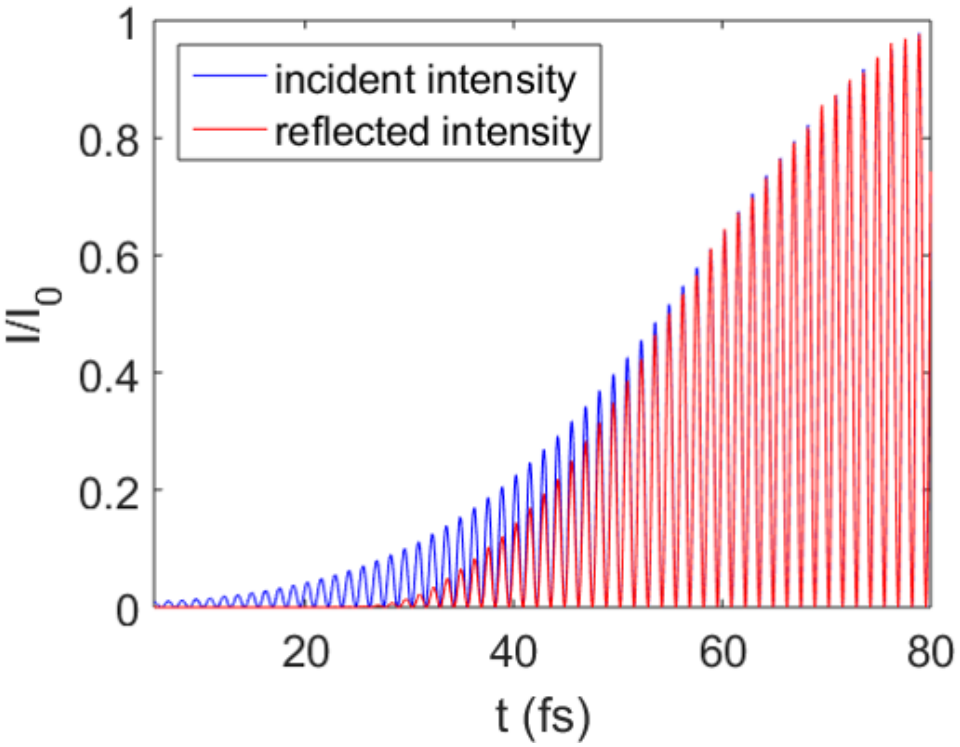

Figure 6.12: Pulse shortening after plasma mirror. Reflected pulse (red) has a 30 fs shorter rising edge than the incident pulse (blue).

Fig. 6.12. The reflected intensity, as measured by point field probes centered in the beam's k-vector, is greatly reduced in the first 30 fs of the rising edge of the beam when compared to the incident pulse. Implementing alternate pulse shapes which more closely resemble the laser pedestal, while computationally intensive, will be a key test of the validity of this simulation technique.

Chapter 7
Solid Target Ion Acceleration at Oblique Ultrashort Laser Incidence

7.1 Introduction

[6] The acceleration of protons from solid targets using high power lasers to greater than 1 MeV was first reported in 2000 [147, 148, 149]. Over the next two decades, efforts to improve peak proton energy, yield, and ion beam divergence have revealed a number of underlying acceleration mechanisms [150, 151] in addition to the sheath acceleration which was first observed [149, 152]. Detailed surveys of the history of this field can be found in Refs. [153, 87, 154], which also discuss the variety of applications which can be enabled by laser-accelerated ions.

The realization of proposed ion beam applications such as neutron radiography and hadron therapy faces two critical challenges. From a practical perspective, one needs the ability to produce sufficient ion flux through efficient procedures – rapid target insertion, laser operation, and optimized on-line diagnostics. More fundamentally, a thorough understanding of the underlying processes that govern ion acceleration in order to better control aspects such as kinetic energy, particle number, and beam profile is required. For this, increases in laser energy and power have not yielded ion energies necessary to achieve ap-

[6] Much of this chapter is reprinted with permission from P. L. Poole, L. Obst, G. E. Cochran, J. Metzkes, H.-P. Schlenvoigt, I. Principe, T. Kluge, T. Cowan, U. Schramm, and D. W. Schumacher, New Journal of Physics, vol.20, 013019 (2018) [22].

plications like cancer therapy due in part to poor scaling with laser intensity and also to stringent requirements on laser parameters like pulse contrast, which measures the intensity of unwanted but often unavoidable pre-pulse light preceding the main beam relative to that of the peak pulse. While several mechanisms have been identified for ion acceleration [149, 152, 155, 156, 151] and multiple reviews have been done to accumulate experiment, simulation, and model descriptions of these [153, 87], the optimization of a given mechanism for an application on any particular facility remains difficult. We performed an experiment that varied the target thickness over two orders of magnitude so that, according to current understanding, two or more of these mechanisms should have made a significant contribution to the measured ion energies. Moreover, the experiment was performed at a large angle of incidence, 45° with respect to the target normal. This introduced two natural directions, target normal and laser axis, and ion spectra were measured in both directions to better distinguish between mechanisms. We found that target normal behavior was seen for all thicknesses; a result that requires explanation.

Figure 7.1 shows a survey of target thickness scans reported in the literature, separated by angle of incidence and laser pulse duration. Lasers at normal incidence (triangles) generally produce higher peak proton energies than those at oblique incidence (circles), and lasers with $\tau > 500$ fs (hollow symbols) generally outperform those with $\tau < 100$ fs. Many of the scans shown here follow a similar pattern, where an optimum target thickness exists at which the highest peak proton energy is achieved, and below which the energy typically drops monotonically. The range, granularity, and minimum value of target thicknesses in this type of experiment can be limited by a number of factors, including target cost, difficulty in manufacturing, and slow alignment speeds. Additionally, it is at times difficult to repeat target thicknesses, meaning observed trends can be highly suspectible to shot-to-shot variation. Using liquid crystal targets and the 1 Hz repetition rate DRACO laser [13], an impressive 450 shots were collected in 5 days [22], in the first experiment to span the few nm to few μm range with a single target material. This allowed the investigation of different laser contrasts and diagnostics, and produced a data set from which average peak proton energies could be extracted at a number of target thicknesses (solid black stars).

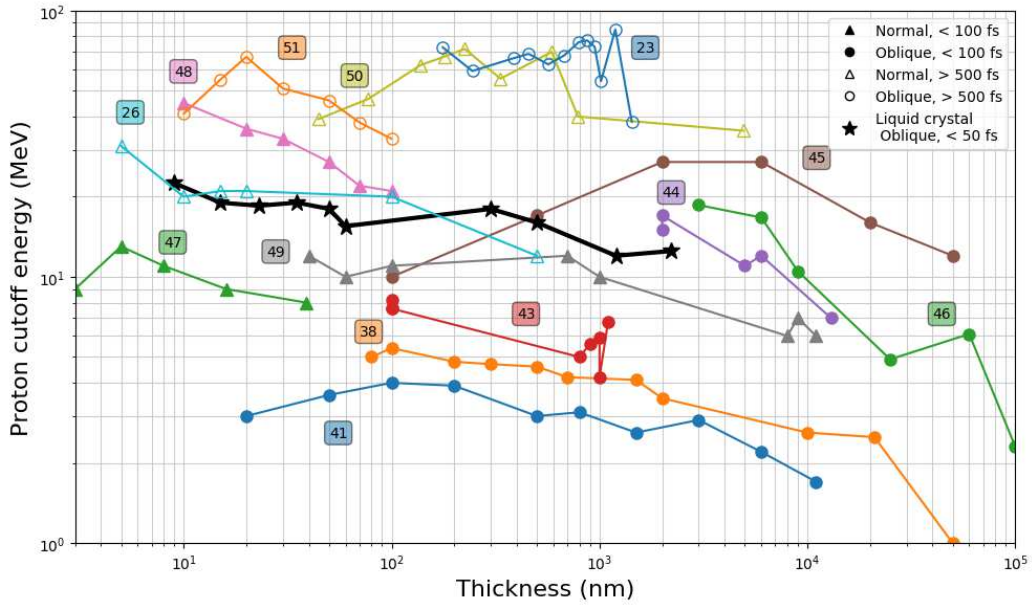

Figure 7.1: Proton energy target thickness scans reported in the literature, separated by incident laser energy. Data represented by circles are near 45° incidence ([9] (averaged data), [10], [11], [12], [13], [14], [15] (22°)) and triangles indicate normal or near-normal (< 10°) incidence interactions ([16], [17], [18], [19], [20] (averaged data), [21]). Filled data points are from pulses of 50 fs duration or less, while open points indicate greater than 500 fs. The averaged results from this experiment are shown as black stars; this is the first dataset to span the full range from few nm to few μm with a single target material. Figure reprinted from [22].

This experiment, and the ion acceleration mechanisms which are responsible for its results, will be the focus of this chapter.

7.2 Overview of Ion Acceleration Mechanisms

7.2.1 Target Normal Sheath Acceleration

Target Normal Sheath Acceleration [149, 152], or TNSA, is the most-studied and most robust method of laser ion acceleration using solid targets. In TNSA, fast electrons are generated in the front-side pre-plasma and propagate through the target. The highest energy electrons are able to escape from the target, which then acquires a positive charge, creating a strong sheath field at the target surface that will cause slower electrons to be accelerated

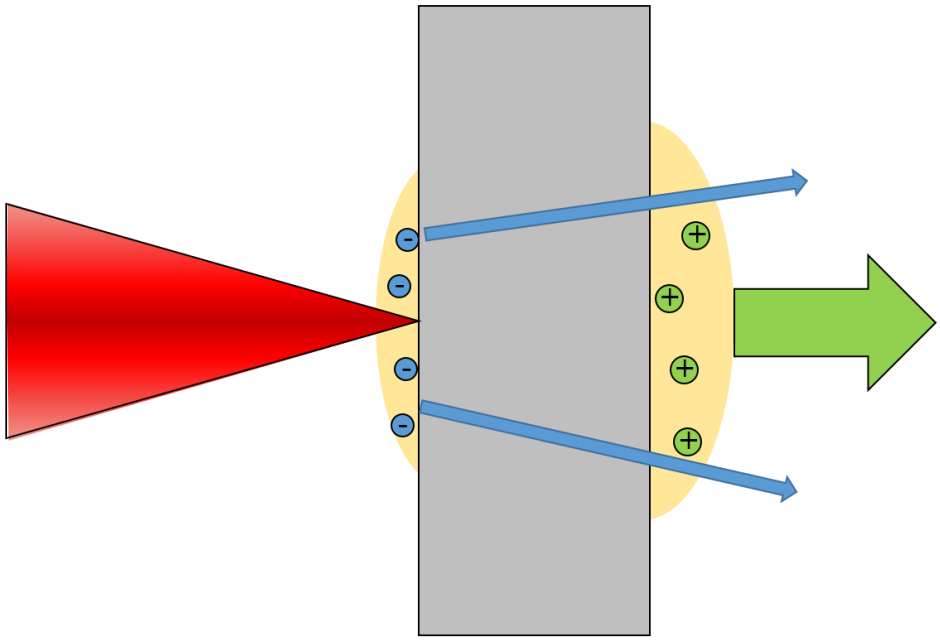

Figure 7.2: Cartoon of target normal sheath acceleration. An incoming laser accelerates hot electrons at the front surface, which propagate through the target. The electrons in the target are heated, and create a strong sheath field on both sides of the target, which accelerates surface ions.

back toward the target and continue to oscillate (or "reflux") about the remaining ion population as its distribution evolves. These electrons then expand due to their own pressure. The separation between these charged species results in a large (MV/μm) quasi-static electric field oriented along the target normal direction. Atoms in the rear surface layer are thereby ionized and accelerated to energies $\sim$10s of MeV/nucleon. The discussion of this mechanism will follow the treatments in [153] and [87].

The magnitude of the accelerating sheath field can be estimated by $E_s \sim T_{hot}/e\lambda_D$, assuming a sharp plasma/vacuum interface at the target rear surface, where T_{hot} is the characteristic temperature of hot electrons accelerated by the laser at the front surface. Determining the hot electron density n_{hot} is more difficult – assuming the energy flux lost from the laser is converted into hot electrons traveling at c, one can write $\eta_{hot} I \simeq n_{hot} c T_{hot}$, where η_{hot} is the conversion efficiency, typically between 10 and 40 percent.

T_{hot} scales with laser intensity, increasing the strength of the sheath field and peak energy of accelerated ions. T_{hot} can be estimated as roughly the cycle-averaged laser oscillation energy $m_e c^2(\langle\gamma\rangle - 1) = m_e c^2(\sqrt{1 + a_0^2/2} - 1)$. In the context of hot electron generation, this is referred to as the Wilks scaling [157, 87], and can be written as

$$T_{Wilks} = 0.51 MeV \left(\left(1 + \frac{I_{18}\lambda_{\mu m}^2}{1.38} \right)^{1/2} - 1 \right). \tag{7.1}$$

For $I = 10^{21}$ W/cm^2 and 1 μm light, $T_{Wilks} = 13.2$MeV, $n_{hot} = 1.6{\times}10^{21}$/cm^3, and $\lambda_D = 0.7\mu$m, yielding a sheath field magnitude $E_s = 19.4$ MV/μm.

Ions at the target rear surface are accelerated in this field. Assuming that the sheath field can evolve, and that the electrons and ions can be treated as isothermal fluids [158], the maximum ion energy attained via TNSA can be estimated by

$$E_{max} = 2T_{hot} \left[\ln\left(t_p + \sqrt{t_p^2 + 1} \right) \right]^2, \tag{7.2}$$

where the normalized acceleration time $t_p \simeq 0.43\omega_{pi}\tau_{acc}$, and the ion plasma frequency $\omega_{pi} = \sqrt{n_{hot} Z e^2 / M_i \epsilon_0}$ for an ion of charge Z and mass M_i. As above, the number density of hot electrons $n_{hot} \simeq \eta_{hot} I / c T_{hot}$ (more sophisticated models take into account the angular

divergence of hot electrons within the target, which increase the transverse extent of the rear sheath field). Fuchs et al. [159] have found by fitting to experimental data that $\tau_{acc} \simeq 1.3\tau_{FWHM}$. Using these parameters and T_{Wilks}, a 1 μm laser with $I = 1{\times}10^{21}$ W/cm^2, $\tau_{FWHM} = 30$ fs, and $\eta_{hot} = 30\%$ is predicted to produce TNSA protons with energies up to 38 MeV. A laser with a 500 fs pulse duration, but the same parameters otherwise, can produce proton energies of 410 MeV according to this model. Increasing the number of hot electrons or T_{hot} will improve ion yield and/or peak energy; much effort has been devoted to optimizing front surface structures to increase the conversion of laser energy into hot electrons and protons [160, 161, 162].

TNSA can benefit from pre-pulses – the resulting target pre-plasma is abundant with electrons available for laser acceleration, yielding a larger rear-surface sheath field–but will suffer if the target is sufficiently deformed by these early pulses or if the pre-pulse scale length becomes too long [163, 87, 55]. Because of this TNSA is typically maximized for targets robust enough to withstand initial interaction with the laser pre-pulse and main pulse rising edge, typically above several hundred nm. TNSA is nevertheless observed on both short and long pulse systems: current experimental benchmarks for TNSA include 40 MeV protons for ultra-short pulse interaction [164] and 85 MeV for longer pulse lasers [9], both achieved with ~ 1 μm thick foils.

7.2.2 Radiation Pressure Acceleration

Other ion acceleration mechanisms can arise for thinner targets (thicknesses down to a few nm have been explored, as in this work). Experiments in this regime typically require intensity contrasts superior to 10^{-10}:1 for times at least one picosecond before the main pulse arrives to preserve target integrity. Targets can also undergo Radiation Pressure Acceleration [155], where the target receives momentum from the laser. In the simplest picture, the radiation pressure due to an incident light wave can be written as $P_{rad} = (1 + R)I/c$, with reflectivity R ≤ 1. As with TNSA, the laser pushes on the ions indirectly through the electrons, since the larger mass of the ions makes them respond more slowly to the laser interaction. However, with TNSA the laser interaction is localized at the front

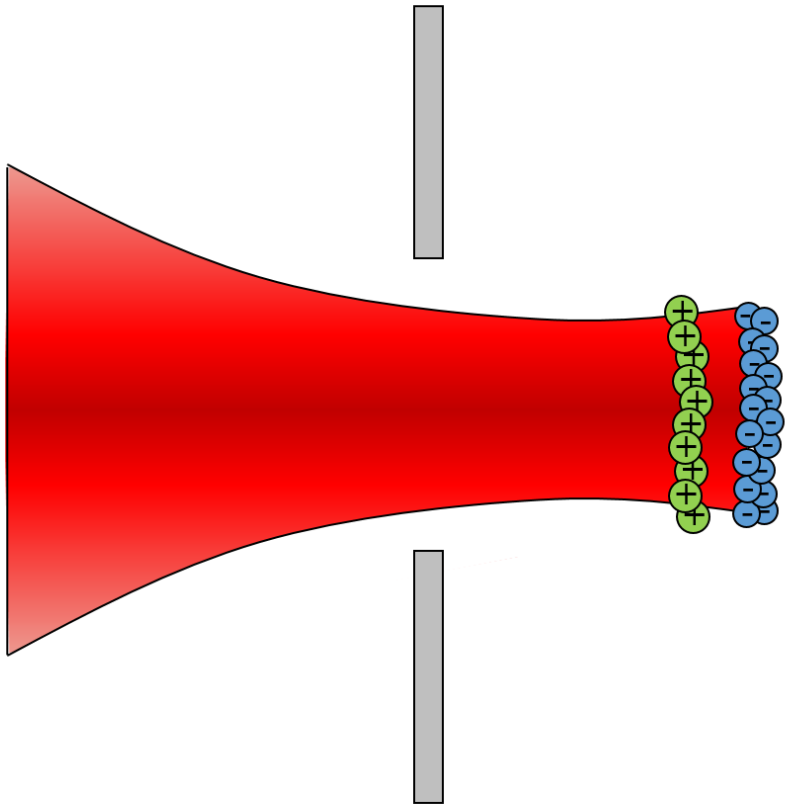

Figure 7.3: Cartoon of light sail RPA. The laser-driven ion front has reached the rear of target and caused the focal spot area to separate from the bulk of the target, allowing it to be driven in front of the laser as it propagates.

surface of the target whereas the electrons accelerate the ions on the back surface. In RPA, there is no such division. (There is front surface TNSA, as well, but there is still a division between the laser-plasma interaction heating the electron and the acceleration process from the hot electron population.) For thin enough targets, RPA can be more effective than TNSA – at the time of this writing, the highest peak proton energy is 94 MeV with a 90 nm target, accelerated through RPA [165]. Two limiting cases have been defined for RPA [87] for very thick and very thin targets.

In the case of a very thick target, a laser pushes against the surface, driving a deformation into the plasma – this is referred to as hole boring radiation pressure acceleration (HB-RPA). The velocity of this deformation, the hole boring ion velocity v_{HB}, can be estimated [157, 166] by applying a momentum flow conservation argument to the laser and ions, such that

$$v_{HB} = \frac{c\sqrt{\Pi}}{1+2\sqrt{\Pi}}, \Pi = \frac{I}{m_i n_i c^3}. \tag{7.3}$$

In the lab frame, the maximum energy of ions traveling in this front is

$$E_{max} = 2m_p c^2 \Pi / \left(1+2\sqrt{\Pi}\right), \tag{7.4}$$

and so $E_{max} \propto I^{1/2}$.

For very thin targets on the order of the laser skin depth, the RPA interaction must be approached differently. If the hole boring ion front reaches the target rear surface before the laser pulse ends [167], the laser can punch through the target, continually accelerating electrons and ions. This is called light-sail RPA (LS-RPA). In this limit, the energy of accelerated ions can be estimated as

$$E_{LS} = 2\pi \frac{Z}{A}\frac{m_e}{m_p}\frac{a_0^2 \tau}{\zeta}, \tag{7.5}$$

where the surface density $\zeta = \pi(n_e/n_c)(d/\lambda)$.

In both HB- and LS-RPA, the accelerated ion spectrum is largely monoenergetic, though recent work has suggested that this can only be expected for a normally incident laser, and

so spectral shape cannot be used as an indication of underlying mechanism for oblique incidence [168].

7.2.3 Relativistic Transparency

Equation 7.5 suggests that RPA-LS energies will continue to increase as the laser intensity does. However, the laser itself can spoil the target opacity that RPA-LS relies on. The laser will penetrate up to the density at which $\omega_L = \omega_p$ – at ultrahigh laser intensities, electrons become relativistically massive ($m_{rel,e} = \langle\gamma\rangle m_e$) and ω_p is reduced, so now transparency occurs when $\omega_L = \omega_p/\sqrt{\langle\gamma\rangle}$. Alternately, the target can also become transparent if it is compressed so that its new thickness d is less than the laser's relativistic skin depth $\delta s, rel \sim c\sqrt{\langle\gamma\rangle}/\omega_p$, taking into account the compressed target's increased electron density. Which of these occurs first depends on the initial target parameters. By considering the dynamics of an infinitesimally thin foil, it has been shown [150] that if the surface density of the target $\zeta \leq a_0$, relativistic transparency will take place and shut off RPA. For an 800 nm 30 fs laser with $I = 1 \times 10^{21}$ W/cm^2, this suggests that the minimum target thickness at which transparency effects can be avoided is d (nm) $\simeq 10^{25}/n_e(/\text{cm}^3)$. Relativistic transparency can occur at different points during the laser pulse [169].

Upon initiation of transparency, a number of effects which enhance ion energy can take place. A laser transmitting through the target can expel some or all of the electrons in its wake, leaving the ions to be violently repelled in a Coulomb explosion [170, 171]. Breakout afterburner [172] or the relativistic plasma aperture [173] also have been demonstrated to enhance laser-axis accelerated ions after the onset of transparency for longer pulses.

7.2.4 Determining Dominant Mechanisms

The scaling laws presented give some indication of whether a laser-target interaction is TNSA or RPA dominant, but in practice parameters such as electron density when the peak of the laser pulse hits or peak intensity are difficult to measure. Accelerated ion directionality is much easier to determine, and has been used as an indicator of underlying mechanism by separating laser axis and target normal ion acceleration directions. In a

number of papers [174, 9, 175, 58], ions directed along the target normal have been described as TNSA, and RPA ions are expected to appear along the direction of pulse propagation [12, 175]. The DRACO experiment described in the following sections used an oblique laser incidence angle to determine where the transition between these signatures occurred.

7.3 DRACO Experimental Setup

The experiment was performed on the DRACO laser facility at HZDR, which before a 2018 upgrade was a 3.5 J, 30 fs, 10 Hz Titanium:sapphire based system capable of intensities exceeding $1{\times}10^{21}$ W/cm^2 in a 3 μm diameter FWHM focal spot. Figure 7.4 shows a simplified schematic of the primary diagnostic setup, which included an optional single plasma mirror for pulse contrast enhancement. Contrast measurements with and without a plasma mirror are shown in Fig. 7.5. The optics design focused light onto and then recollected it from the plasma mirror with off-axis parabolas which allowed the setup to be bypassed if desired by moving an additional mirror into the beam-path. The entire plasma mirror optics path had an energy throughput of 80%, resulting in energies between 2.55 - 2.75 J on target. Near-field measurements after plasma mirror reflection were monitored on each shot and did not reveal modulations that would suggest a reduction in final focal spot quality. The plasma mirror substrate had dimensions of 50 mm $\times$ 95 mm which allowed about 450 few mm spots to be used before it needed to be replaced. The DRACO contrast as measured by a third-order cross-correlator was improved by nearly 3 orders of magnitude when the plasma mirror was in use, allowing comparison between moderate and high contrast shots to investigate the effects of target pre-expansion. The performance of this plasma mirror system was unusual and at the high end of reported performance for such systems [176].

Liquid crystal films were formed within a Linear Slide Target Inserter device, or LSTI [6]. The 4 mm diameter circular aperture was oriented at 45° with respect to the incoming laser axis. 10 μL of the liquid crystal 4-cyano-4'-octylbiphenyl (8CB) was applied to the wiper, which allowed several dozen films to be formed before the chamber needed to be

opened for new liquid crystal application. A cooled water line pumped by a small chiller unit was installed through the chamber wall to maintain the LSTI frame at the desired temperature for film control, typically around 28.0 °C. Film thicknesses were measured on-demand by white light interferometry, which was relayed from outside the chamber. The LSTI design utilizes the same liquid crystal mesophase surface tension that enables freely suspended film formation to draw films at the front aperture edge within 2 μm of the same position each time, which eliminates the need for target alignment after it is performed on the first film. This alignment, performed with a scattered light imaging system, was verified by observing the accelerated proton energy with on-shot diagnostics as the target was shifted along the incoming laser axis. All data shown here was taken at best focus.

Ions accelerated from the target rear side were captured by two diagnostics: Thomson parabola spectrometers (TPS), on laser axis and target normal, and radiochromic film (RCF) stacks on some shots centered on target normal. A schematic of TPS operation is shown in Fig. 7.6. Charged particles enter a small pinhole, typically a few hundred microns in diameter, and are deflected by parallel electric and magnetic fields and form parabolic traces for each charge-to-mass ratio. Neutrons and x-rays, unaffected by these fields, provide a reference neutral point from which ion deflections distances, and thus energies, can be calculated. Electrons are steered away from the diagnostic plane. In this case, the parabolic traces were incident on a microchannel plate (MCP). This diagnostic provides high resolution energy and species information at one specific angle. The TPS used in this experiment had an energy resolution of 0.5-1 MeV from 0 to 30 MeV.

The TPS were supplemented by an RCF stack on some shots (example given in Fig. 7.10). RCF darkens when exposed to radiation, and gives an indication of spatial ion distributions as well as coarse spectral information. Ion species cannot be distinguished when analyzing RCF, so stacks are often wrapped in a filter layer to block heavy ions. The liquid crystal targets used are composed of hydrogen and carbon, and the 25 μm aluminum filter layer used could block up to 27 MeV carbon ions. In this experiment, RCF stacks were used predominantly to examine proton spatial distributions. Located 55 mm behind the target, these captured an angle of $\pm 22.5^\circ$ centered around the target normal direction,

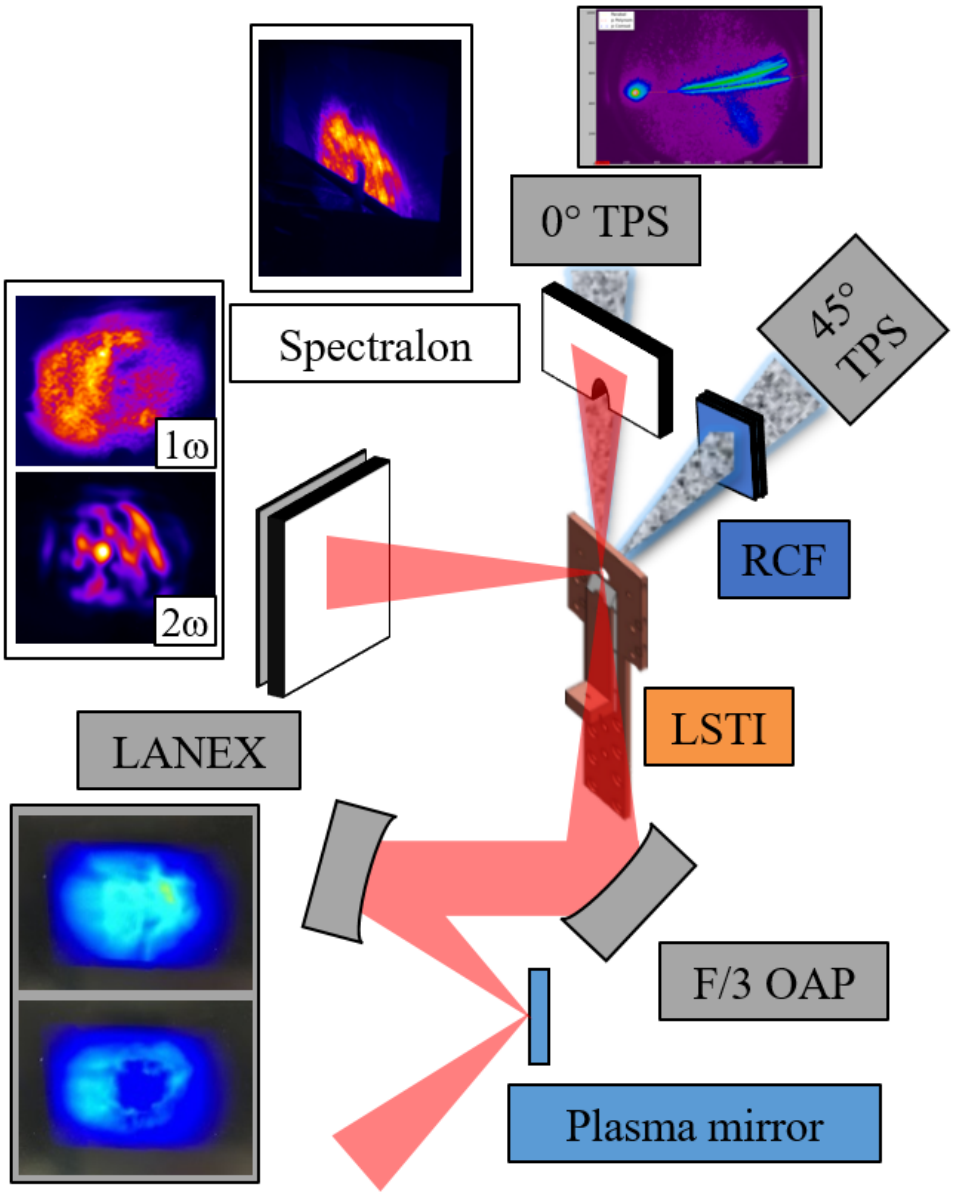

Figure 7.4: Experimental setup at the DRACO laser facility. Laser (red) was reflected from a contrast-enhancing plasma mirror and focused onto the target film formed in the LSTI. Ions emitted on laser axis (0°) and target normal (45°) were observed using Thomson parabola spectrometers (TPS) and radiochromic film stacks (RCF), discussed in more detail in the text. Transmitted light was measured on a Spectralon scatter screen. Reflected light in 1ω and 2ω were imaged from a Macor scatter screen - electrons in this direction were also observed on a LANEX screen. Figure reprinted from [22].

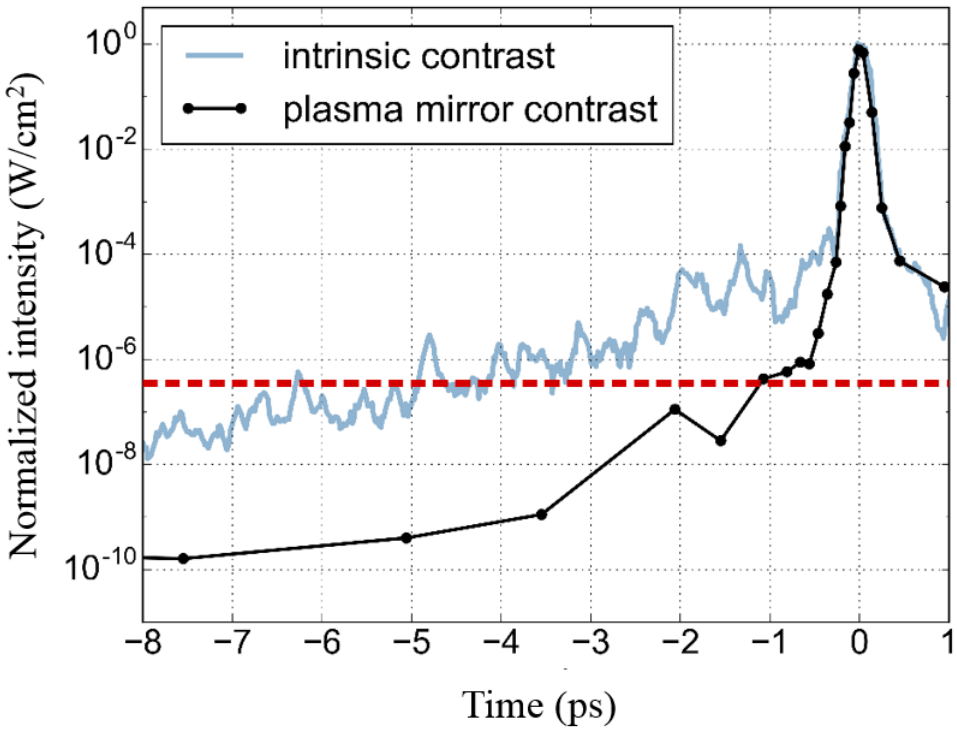

Figure 7.5: Contrast improvement through use of a single anti-reflection coated dielectic plasma mirror. DRACO intrinsic contrast (blue), is improved by ~ 3 orders of magnitude (black dots), on the picosecond level. Figure reprinted from [22].

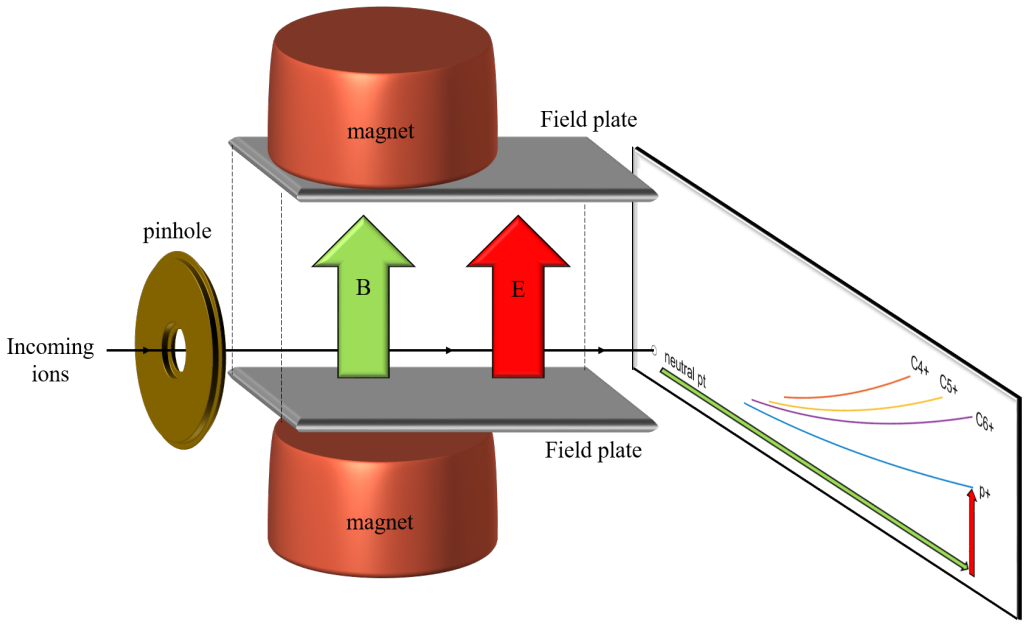

Figure 7.6: Schematic of a Thomson parabola spectrometer (TPS). Incoming ions pass through a pinhole and parallel electric and magnetic fields, and are deflected differing amounts depending on their energies and charge-to-mass ratios. Neutrons and photons are unaffected, and create a neutral reference point on the screen.

with a small aperture to allow ion signal to reach the TPS.

Additional diagnostics were implemented to investigate the reflected and transmitted light upon interaction with the optical quality target surface. This would not only reveal the onset of transparency effects and allow their interaction with ion acceleration to be observed, but also would allow target morphology conditions to be determined at the time of laser interaction. The interplay between ion energy and laser transmission is fundamental to ultrathin target studies, and so it was critical to also have a measure of transmitted laser light on every shot. A piece of Spectralon (Lambertian Scatterer) was used to collect the transmitted beam mode, was absolutely calibrated to 100% transmission when a target was absent. A ceramic (MACOR) screen served the same purpose for the reflected light. Two cameras filtered for 1ω and 2ω observed scattered light imaged from the ceramic screen along the same line of sight by using a dichroic mirror. A final diagnostic was a sheet of LANEX, which fluoresces upon impact by energetic electrons, to reveal the spatial distribution of

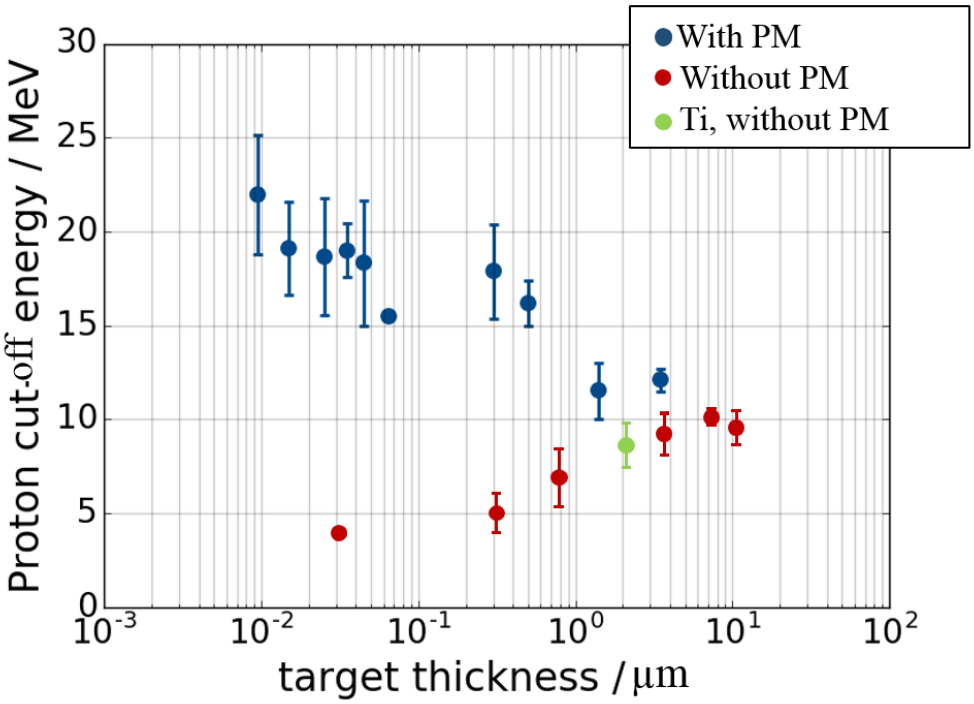

Figure 7.7: Peak proton energy in MeV as a function of target thickness in microns. The optimum target thickness without a plasma mirror is $\sim$ 900 nm and 10 MeV (red points). With a plasma mirror (blue points), proton energies increase monotonically as target thickness is decreased - no optimum thickness is seen. Points represent average maximum proton energy seen at this target thickness, while bars indicate broadest range of energies seen at that thickness over the course of the run - variability increased as target thickness decreased. Figure credit: Patrick Poole.

target front-surface electrons ejected in the reflection direction. On some shots a rough electron energy spectrum was obtained using transmission through a wedged aluminum piece in front of the screen.

7.4 Key Experimental Results

7.4.1 Effects of Prepulse

The central experimental result is shown in Fig. 7.7: maximum proton cutoff energy recorded on the target normal Thomson parabola spectrometer for film thicknesses ranging

from > 1 μm to 10 nm. Without a plasma mirror, DRACO's moderate 10^{-7} contrast produced a typical maximum proton energy trend with target thickness as measured by the TPS, shown in Fig. 7.7. The "optimum thickness" at which the maximum proton energy of 10 MeV was observed, was approximately 900 nm. As target thickness was decreased from this point, maximum proton energy decreased monotonically. When the plasma mirror was employed to improve the laser contrast to $\sim 10^{-10}$, the proton maximum energy was instead seen to monotonically increase with target thickness, and no optimum thickness was observed - a peak proton energy of 26 MeV was recorded for a target thickness of 6 nm (not pictured). This is an interesting result, particularly in light of the fact that the target thickness is less than the laser skin depth.

The high proton energy achieved for ultra-thin targets suggests a high contrast laser interaction, where the target surfaces remain intact before the main pulse arrives. This is supported by observations of the specular-directed optical emission during laser interaction recorded with both 1ω and 2ω filters. Here we expand the measurement of previous target emission studies [122, 177] by always using peak laser intensity but with deliberate pulse contrast differences: Figure 7.8 shows representative images of the moderate (no plasma mirror, left) and high contrast laser reflection (right). High contrast results in significantly enhanced reflected light levels and a better-defined spatial mode. Under this condition of unperturbed target surface at the initiation of high intensity laser interaction, 2ω emission becomes visible, with expected spatial modulations due to the strongly intensity-dependent generation process. This improved reflection quality indicates a minimally expanded critical surface in the high contrast case [178] and was observed even for ultra-thin targets.

High contrast interaction is further corroborated by the LANEX diagnostic observing electrons ejected in the laser reflection direction during target interaction. Up to 30 nC sr^{-1} was measured in electron distributions with energies exceeding 9 MeV, obtained by recording the calibrated [179] LANEX fluorescence behind different thicknesses of the Al wedge. This is similar to recent results [180] where electrons ejected in this manner required laser interaction with a sharp density profile originating from high contrast pulse irradiation.

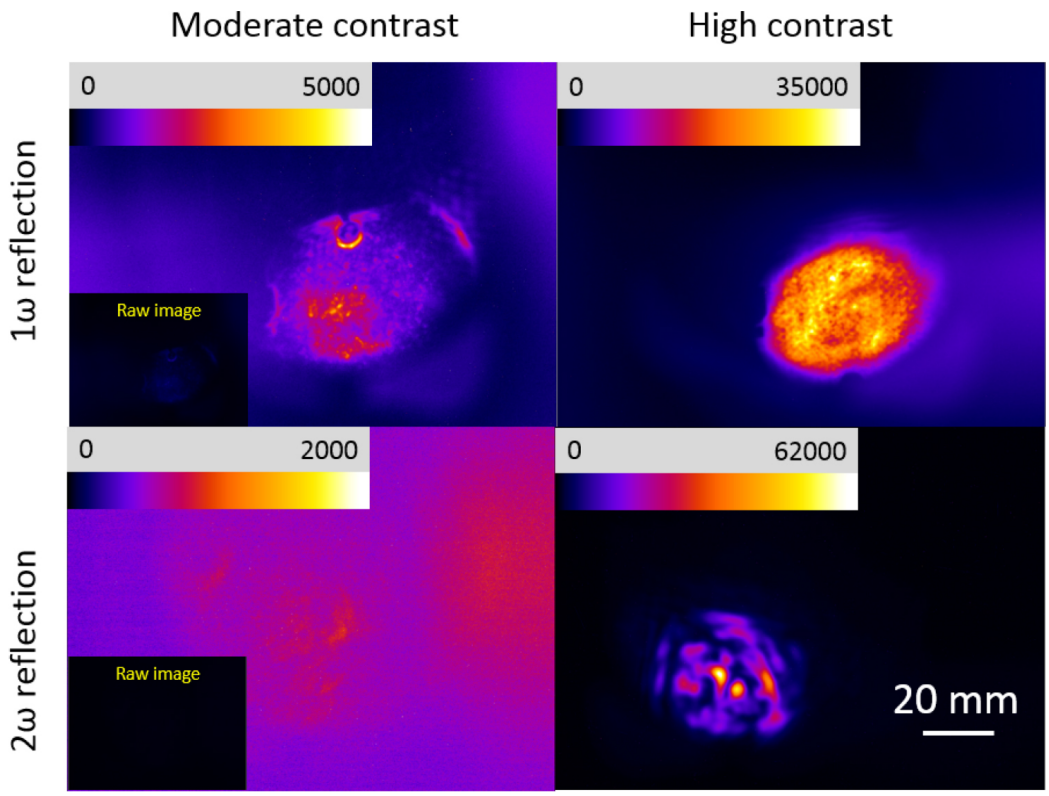

Figure 7.8: 1ω and 2ω reflected modes from moderate and high contrast pulses, showing a significant difference in the target morphology at the time of laser interaction for these cases. The inset in the left hand images shows the moderate contrast reflection raw images (unscaled dynamic range), which reveal significantly less overall reflection compared to high contrast conditions. Figure reprinted from [22].

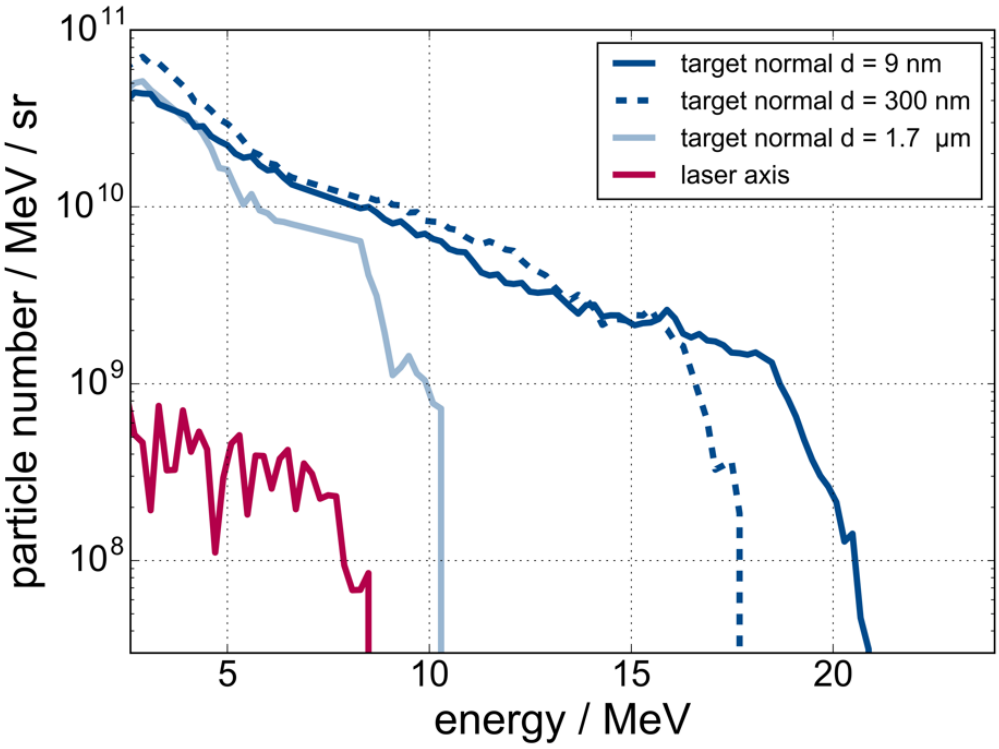

Figure 7.9: Proton spectrum (number/MeV/steradian) as a function of energy (MeV) observed on a Thomson parabola spectrometer in the target normal direction for a 9 nm target (solid dark blue), 300 nm target (dashed dark blue), and 1.7 μm target (solid light blue). The averaged proton signal on laser axis, on the few shots where it was observed, is plotted in red. Figure reprinted from [22].

7.4.2 Ion Directionality

Figure 7.9 shows target normal ion energy traces for various thickness targets (blue lines) for comparison to an average of those laser axis ion spectra observed (red). While all targets have similar spectral shape at low proton energies, the thinnest targets also exhibit increased high energy component suggesting a greater hot electron population. The majority of shots ($\geq$90%) at high contrast showed no laser axis ion signal for any thickness, and when present the laser axis energy cutoff and yield were always significantly lower than that observed along target normal for the same shot.

The target normal spatial distribution of proton emission, shown for various thicknesses

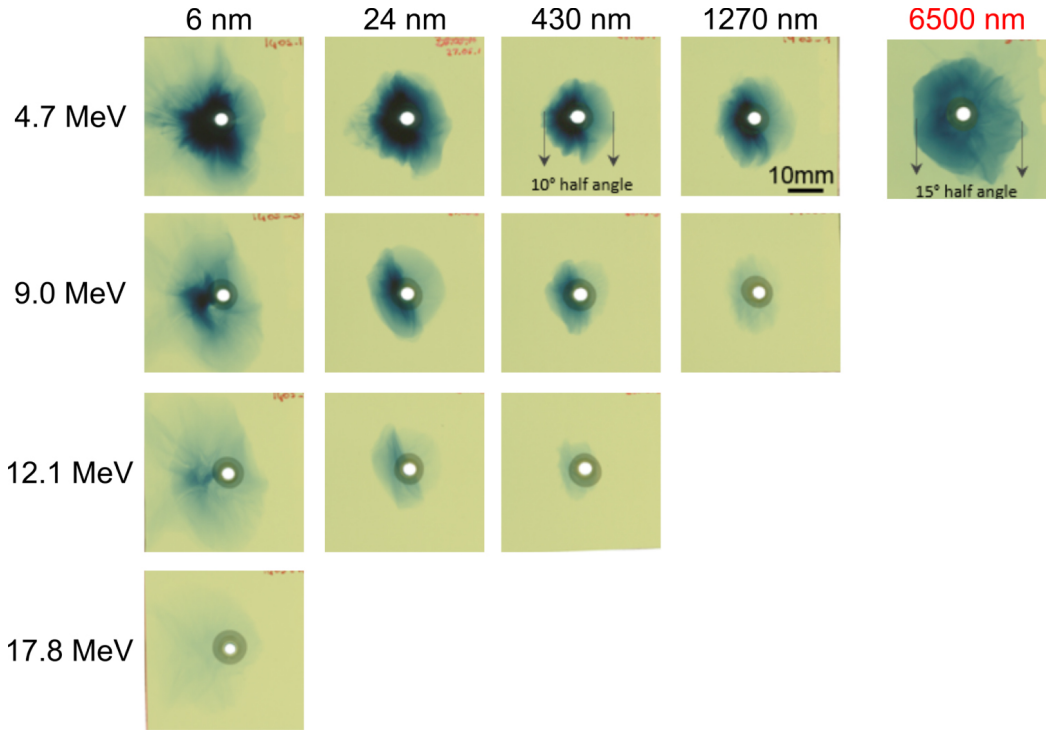

Figure 7.10: Sample layers from RCF stacks irradiated by target layers of different thicknesses. Five shots are shown: from left to right, 6 nm, 24 nm, 430 nm, and 1270 nm shot in high contrast mode, and 6500 nm, shot in moderate contrast mode. From top to bottom, layers corresponding to proton energies of 4.7 MeV, 9.0 MeV, 12.1 MeV, and 17.8 MeV are shown, stopping at the last layer at which signal was observed for each target. The hole in the center of each film allows line of sight for the target normal TPS. Figure reprinted from [22].

in Fig. 7.10, was of consistently small divergence ($\leq 10^{\circ}$) at low and high energy for all thicknesses. This was true even for ultra-thin targets near the transparency threshold with the exception of radial streaking in the low energy ion signal (as in the 4.7 MeV, 6 nm sheet in Fig. 7.10). For comparison, the rightmost film is one layer from a moderate contrast, 6500 nm target result, demonstrating significantly larger beam divergence. The energy spectra, spatial distribution, and directionality of the acceleration ions suggests TNSA as the dominant mechanism for low and high contrast shots for thicknesses from 40 nm and above.

7.4.3 Transmitted Light

Additional characteristics were observed for ultra-thin targets in the relativistic transparency regime. This state was verified in several ways, but most directly by measuring the laser pulse transmitted through the target. These values are shown in Fig. 7.11 as a function of film thickness. Thicknesses above 40 nm exhibit a nearly constant average of $\sim 5\%$ transmission, but those below show both increased average transmission as well as greater shot-to-shot fluctuation.

There is a similar increase in maximum proton energy fluctuations for these ultra-thin targets. Near 10 nm target thickness proton energies ranged from 18 to 25 MeV (see Fig. 7.7) – despite this the average maximum energy was higher for these thinnest targets. A third observation from the transparency regime was a radial streak pattern outside the primary proton spatial structure visible in the lowest energy RCF layers, as in the top left stack of Fig. 7.10. These thinnest targets still showed a high quality reflection during laser interaction, so this burst proton pattern is suspected to originate not from target expansion via pre-pulse but rather from late-time TNSA fields still accelerating particles as the target volume expands after laser interaction.

Although fluctuations in the transmitted light, maximum proton energy, and low-energy spatial distribution were observed for ultra-thin target interaction, none of these effects are seen to correlate strongly with each other, nor with other measured values such as the quality of the reflected or transmitted modes. Additionally, the proton energy only weakly

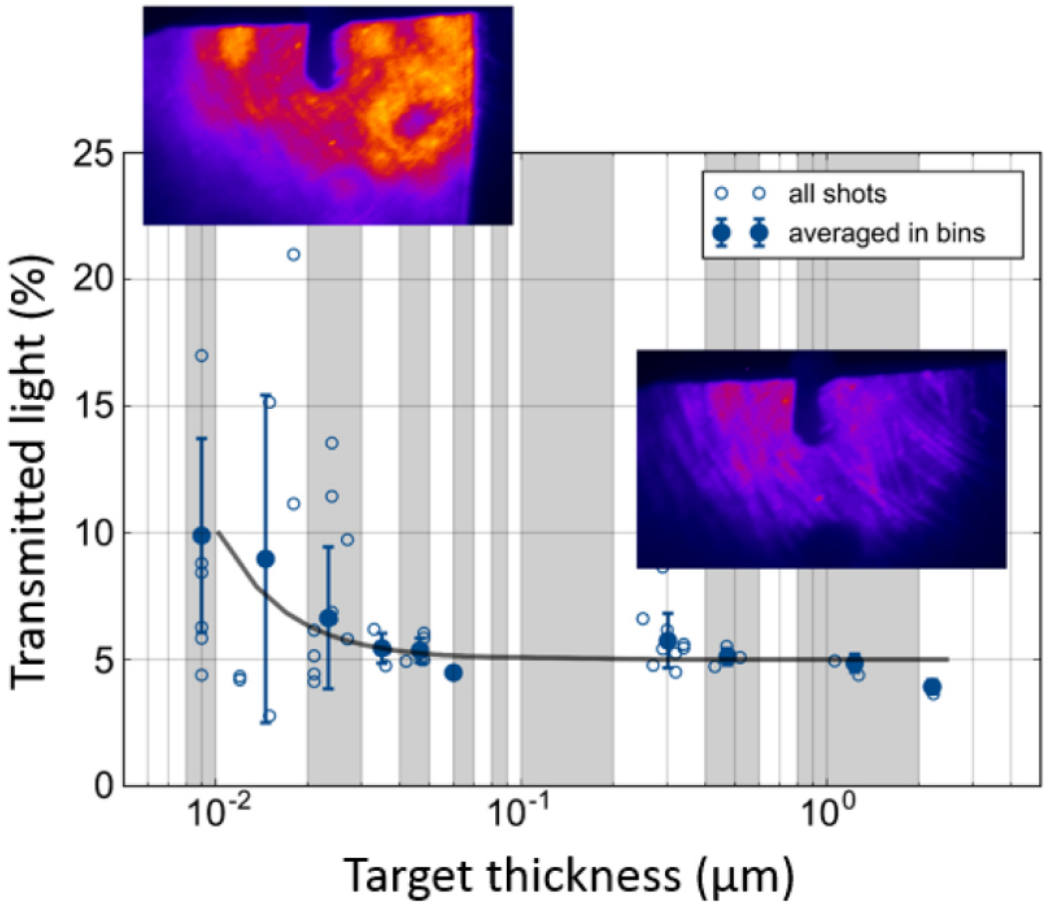

Figure 7.11: Transmitted light measurements with respect to target thickness collected by imaging scatter from a spectralon sheet, absolutely calibrated to shots with no target present. Dark circles are transmission averages over thickness bins indicated by the shaded regions, and the curve is present to guide the eye. Transparency increases significantly near 40 nm. Figure reprinted from [22].

correlates with the ±2% laser energy fluctuations on target.

7.5 Conclusions

In high contrast mode, essentially no laser axis signal was seen at any target thickness – in the literature, this is a clear indication of TNSA. The ion spectral shapes are also TNSA-like, with reasonable agreement in predicted peak ion energies. The ion directionality does not change even in cases of significant laser transmission. What caused this experiment to pass directly from the TNSA regime to that of transparency without ever seeing RPA, which is expected to dominate between the two? This question, and its unexpected answer – that RPA was indeed present, but produced the same experimental signatures as TNSA – were investigated through PIC simulations presented in the following chapter.

Chapter 8
Distinguishing Ion Acceleration Mechanisms Through PIC Simulations

8.1 Introduction

The ion energy and angular signatures obtained in the DRACO experiment are commonly understood to be signifiers of TNSA, but these occurred at target thicknesses well below where RPA is expected to dominate, and even where the target thickness is less than a skin depth and significant amounts of transmitted light are detected. These facts seem to be in contradiction and could not be resolved based on the available experimental data set. To explain this, and to identify which acceleration mechanisms were taking place in the experiment, a series of PIC simulations were run to replicate different target thickness regimes and analyze their behavior. These will be described, and their results discussed, in the following sections.

8.2 Simulation Design

Many of the simulation parameters were set by the laser and target used in the experiment, and are listed in full in Table 8.1. A 30 fs laser with a peak intensity of 4×10^{21} W/cm^2 was incident at 45° on a fully ionized 8CB target. Three target thicknesses were chosen for detailed analysis, 30, 100, and 300 nm. A number of choices were made in designing these runs to balance simulation accuracy and feasibility, which will be discussed in the following

Table 8.1: DRACO ion acceleration simulation parameters. I_0 is the peak laser intensity, λ the laser wavelength, τ the FWHM pulse duration, θ_i the laser incidence angle, T_e the electron temperature, n_e the initial electron density, and ρ_H and ρ_C are the initial densities of protons and C_6^+.

Laser		Target	
I_0 (W/cm^2)	4×10^{21}	T_e (keV)	10
$\lambda(\mu$m)	0.8	n_e (/cm^3)	3.3 $\times 10^{23}$
τ (fs)	30	ρ_H (/cm^3)	5.35 $\times 10^{22}$
θ_i	45°	ρ_C (/cm^3)	4.33 $\times 10^{22}$
pol.	P (XZ-dir)	vacuum gap (μm)	1.8

sections.

8.2.1 Testing Short Scalelength Preplasmas

Experimental measurements of reflected laser light in the second harmonic indicated that the plasma mirror used to remove prepulses was effective in minimizing premature target expansion, though it was difficult to say there was no preplasma whatsoever. Characterization of the plasma mirror [176] showed that ionization, and thus expansion, began no earlier than 3 ps before the main pulse reached the target.

Two-dimensional simulation studies with 300 nm targets showed essentially no difference in accelerated proton spectrum at late times between a clean target interface and one with an added exponential preplasma with scalelength $L = 0.1$ μm, and only a small enhancement in peak energy with $L = 0.5$ μm (see Fig. 8.1). Accordingly, for simplicity in simulation design and in analyzing the underlying physics, a clean interface was used in the 3D production simulations. To preserve a steep interface until the rising edge of the laser reached the target, particle motion was artificially suppressed during the laser travel time to the target. Tests were also conducted to determine the effect of different pulse shapes. While the experimental pulse shape was roughly Gaussian, this pulse shape produced target pre-expansion in simulation which made analysis more difficult. Accordingly, a sin-squared pulse shape was used.

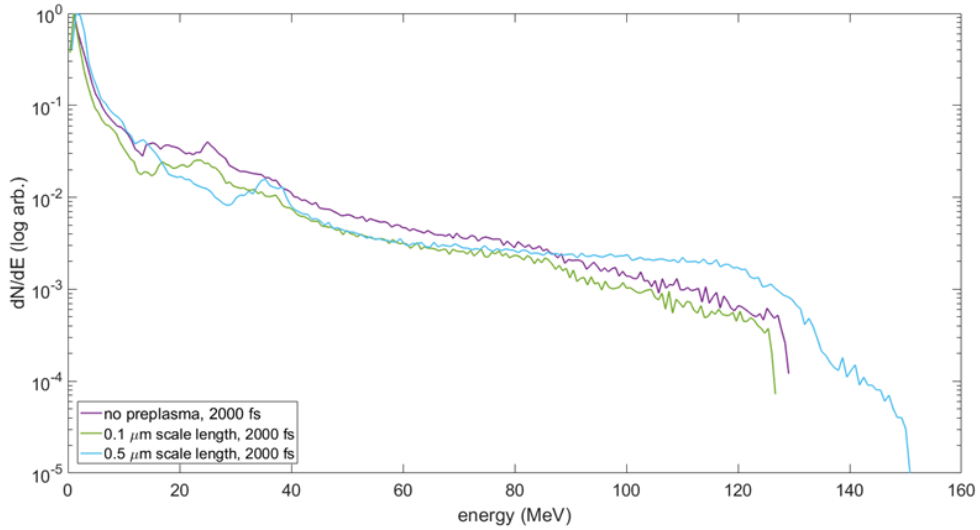

Figure 8.1: Effects of including preplasma in 2D simulations. A laser was incident on a 300 nm target, both following the parameters in Table 8.1, with either a clean front interface (purple), 0.1 μm scalelength preplasma (green), or 0.5 μm scalelength preplasma (blue). Evaluating the spectrum of the accelerated protons (normalized, on a logarithmic scale) shows essentially no difference between a clean interface and 0.1 μm scalelength preplasma, and only a small difference using a 0.5 μm scalelength preplasma.

8.2.2 Physically Accurate Simulation Dimensionality

As discussed in Ch. 3, PIC simulations are frequently performed in lower dimensionalities to conserve computing time or model an otherwise intractable problem. The validity of results obtained this way is highly dependent on the geometry and other aspects of the problem being modeled. 2D3V simulations were investigated as an option for this work, as the time durations and small timesteps necessitated by resolving ultrathin targets are computationally intensive. However, the differences in field falloff and target expansion with number of simulation dimensions were dramatically different in two and three dimensions for this problem, leaving 3D simulations as the only option for quantitative simulation comparison to the experiment results that needed to be explained. An example of this difference is shown in Fig. 8.2; two snapshots of the electric field normal to the target from an $I = 1{\times}10^{21}$ W/cm^2 laser interacting with a 300 nm overdense carbon target centered at $x = 0$. In Fig. 8.2(a) and (b), E_x in a 2D simulation is shown in orange 100 fs and 150 fs into the target evolution, a factor of 40 higher in both cases than the field in the equivalent 3D simulation in blue. The goal of these simulations was to attain as close as possible quantitative agreement with experiment; overly strong accelerating fields will overestimate proton energies, and target transparency will also be mischaracterized in unclear ways. Choosing to run in three dimensions necessitates a few other compromises, which will be discussed in the following sections.

8.2.3 Obtaining Stable Simulations

The constraints applied to these simulations – that they be three dimensional, and run not only for the laser pulse duration but as long as possible after to follow the evolution of the ion distribution – mean that these are prone to numerical instability. Accordingly, the production simulations were run in LSP's implicit mode, which reduces the amount of unphysical energy which accumulates from numerical error. This also allows the Debye length resolution requirement to be neglected, which will be discussed in more detail in the next section. It is important to note, however, that the implicit mode lowers the peak

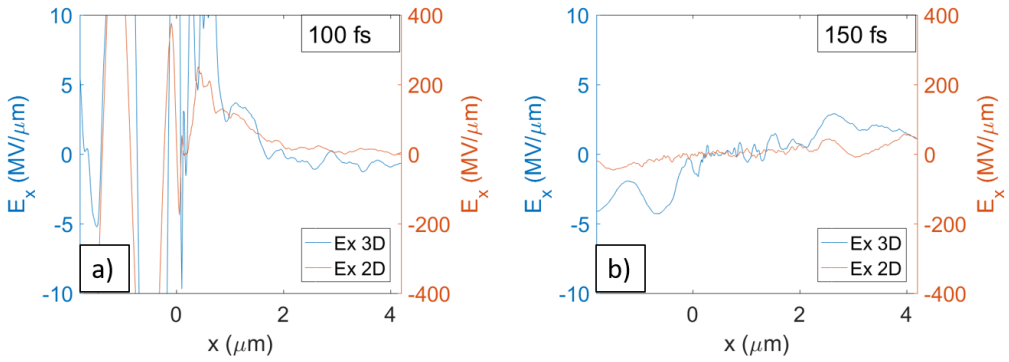

Figure 8.2: Comparison of E_x amplitude between 2D (orange) and 3D (blue) simulations (a) at 100 fs and (b) 150 fs into the target evolution. Note the 2D and 3D results use different scales. At both times, the 2D field strength is $\sim 40\times$ that of the 3D field strength.

Table 8.2: Target thickness-dependent simulation parameters. $\Delta x, y, z$ are cell sizes, ϕ is the beam waist.

Target thickness (nm)	Δx (nm)	$\Delta y, \Delta z$ (nm)	particles/cell	$\phi(\mu$m)
300	15	45	125	1.2
100	5 in target, 15 outside	30	8	1.2
30	1.5 in target, 9 outside	12	8	0.8

energy of accelerated ions (Fig. 8.3). An explicit 2D simulation of a laser interacting with a 300 nm target has a peak accelerated proton energy of nearly 50 MeV (blue), which is reduced to roughly 40 MeV in the equivalent 2D implicit simulation.

8.2.4 Cell Size and Other Resolution Requirements

The target thicknesses of interest for this study compose a wide range of length scales. It has been shown [145] that there are dramatic differences in the amount of laser light absorbed and how it is conveyed to the target bulk as the cell size is reduced to $\delta_s/5$ or even less. For fully ionized 8CB, $\delta_s \sim 10$ nm. However, for the relativistic laser intensities used, it is appropriate to consider the relativistic skin depth $\delta_{s,rel} \sim \langle\gamma\rangle^{1/2} c/\omega_{pe}$; for $I = 4 \times 10^{21}$ W/cm^2, this is more than 50 nm. A more stringent requirement is the number of cells

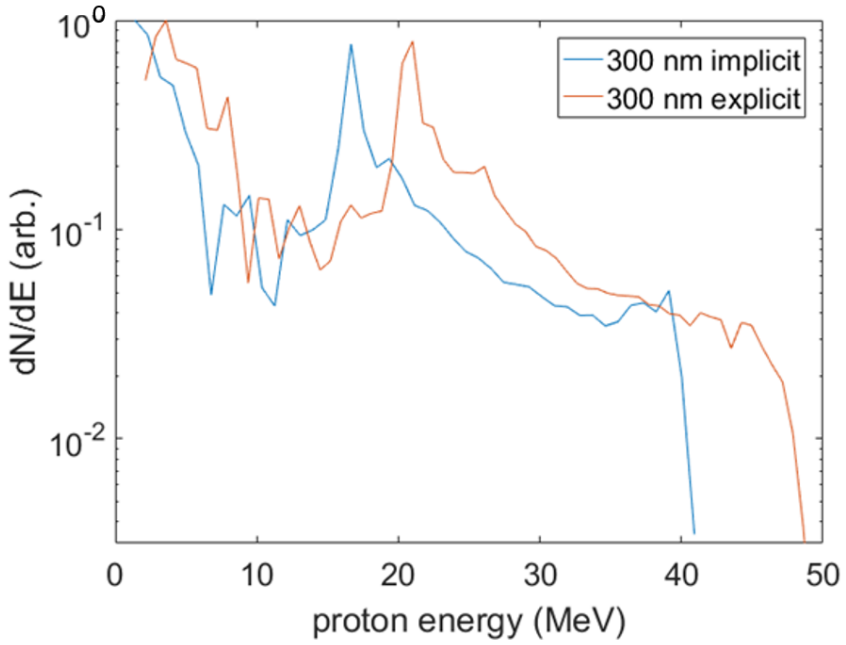

Figure 8.3: Comparison between implicit and explicit simulations. Using the same 2D 300 nm ion acceleration test case as described earlier, accelerated proton spectra on a log scale along target normal are compared for an explicit simulation (orange) and implicit simulation (blue). Running implicitly produces the same spectral shape, with a reduction in peak proton energy of roughly 10 MeV.

comprising each target thickness - as this number is decreased, the evolution of the target density becomes more noisy. The cell sizes chosen in Table 8.2 vary with target thickness to maintain 20 cells per target thickness. For the 100 and 30 nm targets, these small cell sizes cannot be maintained over the large simulation volume, and are expanded outside of the target to a more forgiving value. The laser waist ϕ is smaller than what was used in experiment, again to keep the size of the simulation volume small enough to allow the simulation to be run. Additionally, a small interval between snapshots of field and particle behavior was needed; both of these are recorded every 1 fs to capture dynamics within a laser cycle.

Implicit simulations allow some relaxation of the Debye length resolution requirement, but this may still be necessary in order to model the problem correctly. The question of whether to resolve the Debye length in a simulation of laser-target interaction in order to capture relevant physics has attracted a great deal of interest in the context of ion acceleration. Yin, et al. [172] have argued that one of the necessary components of a simulation of BOA is a well-resolved Debye length. For a plasma with $n_e = 3.3 \times 10^{23}/\text{cm}^3$ and $T_e = 10\text{keV}$, λ_D is 1.3 nm, which would require $\Delta x = 0.5$ nm or less, an expensive cell size. As a surrogate test of what effect resolving the Debye length has, 2D simulations were performed with the same laser interacting with a 300 nm thick target with the same electron density and $T_e = 30$ keV, which has a Debye length of 2.3 nm. Figure 8.4 shows the effects of resolving the Debye length at this temperature - $\Delta x = 15$ nm (in blue) produces an accelerated proton spectrum with a higher slope temperature and nearly a factor of 2 higher maximum energy than resolving the Debye length with $\Delta x = 1$ nm does (in yellow). A 2D run with $\Delta x = 15$ nm and $T_e = 10$ keV (orange), the conditions used in the 300 nm target 3D production run, yield a similar spectrum to the unresolved case - this effect is in the opposite direction than the one from running implicitly, but both are important to consider for the validity of these results.

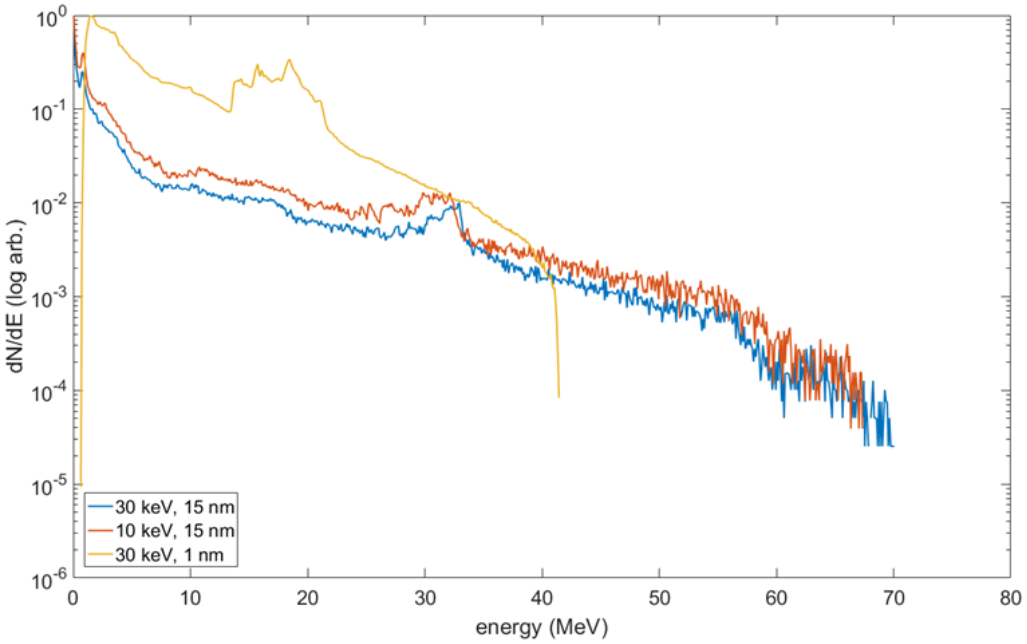

Figure 8.4: Effects of resolving or underesolving the Debye length in simulations. A target temperature $T_e = 30$ keV with $\Delta x = 15$ nm (blue), which underresolves the Debye length, produces a much higher peak proton energy than one at the same T_e with $\Delta x = 1$ nm (yellow), which does resolve the Debye length. Using $\Delta x = 15$ nm and $T_e = 10$ keV (orange) produces a nearly identical spectrum (on a log scale) to that of the higher temperature run, indicating that this difference is due to resolution of relevant scalelengths and not target expansion effects.

8.3 Benchmarking Against Experiment

No simulation can have a perfect match with experimental diagnostics, due to inescapable limitations in simulation volume and resolution. Often, a trend in an observable such as peak proton energy can be used to inform the physics interpretation without matching experimental conditions. However, in this case, it was important to verify that the match to experiment was close enough to lend validity to the interpretation of the simulations. Specifically, the goals were to obtain reasonable quantitative match to ion spectra and peak energies, angular ion distribution, and amount of transmitted light as a function of target thickness.

8.3.1 Ion Energy Trend as a Function of Target Thickness

Firstly, it was important to verify that the proton energy increased as target thickness was decreased. This was assessed using a probe which captured the kinetic energies of all protons to the rear of the target - in Fig 8.5, this is shown on a log scale 50 fs after the peak of the pulse hits the target for a 300 nm (blue), 100 nm (orange), and 30 nm (yellow) target. This time is chosen to compare between target thicknesses as it is the latest point at which the highest energy protons from each target are still within the simulation volume, and is not intended as a perfect surrogate for the time-integrated ion diagnostics used in the experiment. A signal cutoff was chosen of 2.5 orders of magnitude to mimic the dynamic range of the TPS. At this level, the protons accelerated from the 300 nm target reach a peak energy of ~ 16 MeV, while the 100 nm target protons reach ~ 23 MeV and those from the 30 nm target reach ~ 34 MeV. These peak energies follow the trend seen in experiment, and furthermore are in reasonable agreement quantitatively – something that is not typically attained in 2D simulations.

8.3.2 Emitted Ion Direction

To determine the angular trajectories of accelerated protons, an angle in the XZ plane was constructed from the particle's instantaneous momenta p_x and p_z such that $\theta_{xz} =$

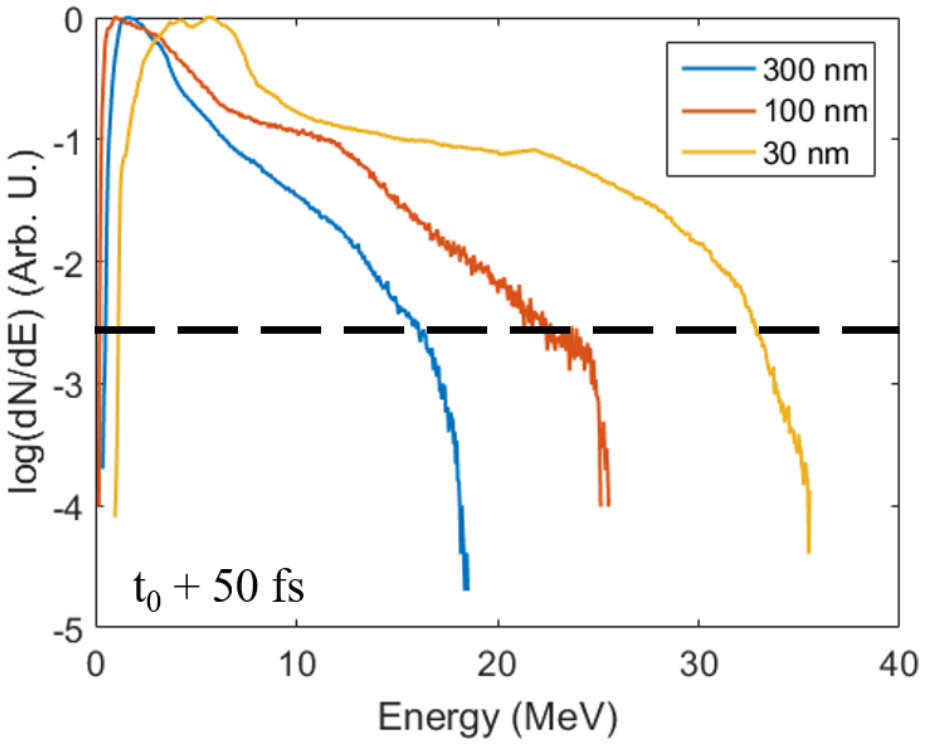

Figure 8.5: Accelerated proton spectra from 3D simulations on a log scale. A 300 nm target (blue) reaches a peak proton energy of $\sim$ 16 MeV; a 100 nm target (orange) reaches a peak proton energy of $\sim$ 23 MeV; and a 30 nm target (yellow) reaches a peak proton energy of $\sim$ 34 MeV. All three target thicknesses produce sptrea with a roughly exponential shape.

$\tan^{-1}(p_z/p_x)$. To focus on the dynamics in the plane of the laser's angle of incidence, only protons which originated within ± 0.3 μm of $y = 0$ were included in this analysis. The protons of the most interest are those that attain high energy, 5 MeV or more. To select only these particles, LSP's particle tracking feature was used, which assigns each macroparticle a unique identifier (x_i, y_i, z_i) which is its initial position in space. Once a simulation has been completed, the particles of interest are found, and their identifiers are selected and followed back through the simulation to reconstruct their behavior as a function of time. The results of this analysis applied to angular trajectory are shown in Fig. 8.7; this technique will be applied to particle energy and initial position in Sec. 8.4. In the 300 nm target, Fig. 8.7(a), the accelerated protons are centered on 5°, roughly target normal, with a fairly narrow spread of $\sim \pm 5°$. Figure 8.7(b) shows the 100 nm target protons centered on the same angle, albeit with a slightly wider $\sim \pm 10°$ spread. The shape described by the expanding protons is different for the 30 nm target (Fig. 8.7(c)), but although the angular spread is large, it is also still roughly centered along the target normal.

8.3.3 Transmitted Light with Target Thickness

Experimentally, the time-integrated amount of transmitted light was the only measure of transparency. The target was observed to be largely opaque down to a thickness of ~ 30 nm, below which the amount of transmitted light increased dramatically. In small simulation volumes like those used here, it can be difficult to separate target-driven fields from those due to the laser. To address this, the time-average of the Poynting vector $\vec{S} = \left(\vec{E} \times \vec{B}\right)/\mu_0$ was calculated to attempt to isolate the laser envelope component. Examples of this are shown for a slice in the XZ plane in Fig. 8.7 – part (a) shows an initially 300 nm thick target which still reflects the vast majority of the laser light, while the 30 nm target in part (b) is transmissive at the same point in time. While not a quantitative measure of agreement with experiment, this is sufficient to show that the target thicknesses we have chosen span the interesting range from opacity to transparency.

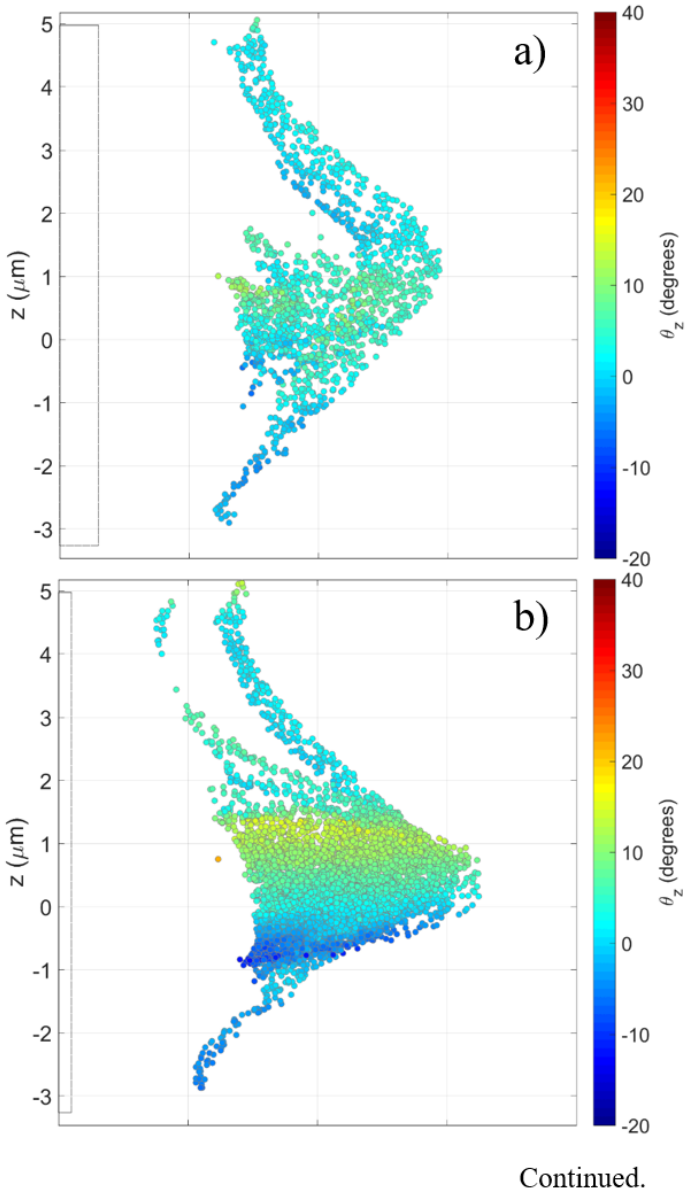

Continued.

Figure 8.6: High energy protons accelerated from 3D laser-target simulations, color-coded by their momenta-derived angular trajectories. Snapshot is taken 50 fs after the peak of the laser pulse reaches the target, and restricted to particles originating within ± 0.3 μm of $y = 0$. (a) Protons accelerated from a 300 nm target are roughly centered on 5°, where 0° is target normal and 45° is laser axis. (b) Protons accelerated from a 100 nm target are also roughly centered on 5°. (c) Protons accelerated from a 30 nm target are also roughly centered on 5°, albeit with a much larger angular spread.

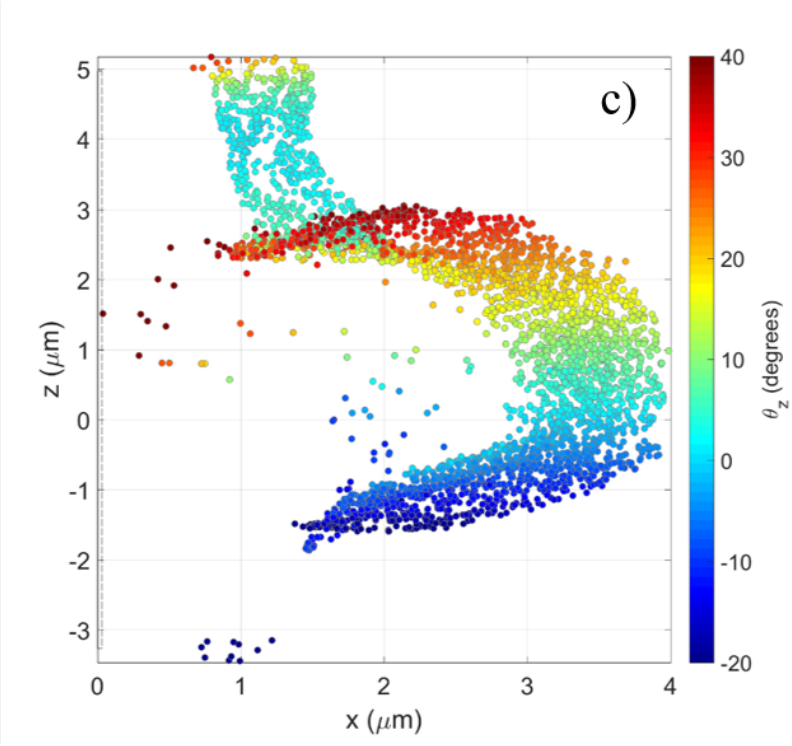

Figure 8.6: Cont.

8.4 High Energy Protons as a Function of Target Thickness

Applying particle tracking to determine the time histories of high energy protons not only reveals their angular trajectories, but their energies and points of origin as well, and this is an illuminating way to determine which acceleration mechanism dominates at different target thicknesses. An example of this is shown in Fig. 8.8. All snapshots are taken using the same sorting mechanism described above, at a point 50 fs after the peak of the laser reaches the target, but here color-coded by particle energy or initial x position. In the top row, protons accelerated from the 300 nm target can be seen to reach a peak energy of ~ 20 MeV (part (a)) – all of the high energy protons in this simulation originate in the front or rear 30 nm of the target (part (b)), with the majority, and highest energy ones, coming from the target rear. This indicates that TNSA is the dominant mechanism at this target thickness.

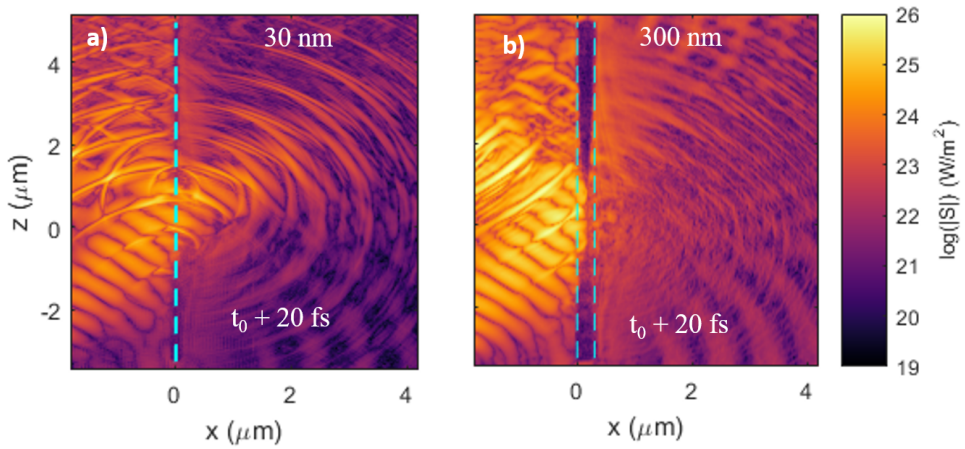

Figure 8.7: (a) Magnitude of the Poynting vector taken at $t_0 + 20$ fs for a 300 nm target(logarithmic scale). The laser has not yet penetrated the target thickness, and is predominantly reflected along the specular direction. Target initial position marked in dashed cyan. (b) Magnitude of the Poynting vector taken at t0 + 20 fs for a 30 nm target (logarithmic scale). The laser has penetrated the target and moved several microns beyond its initial position at this point in time, and laser reflection along the specular direction is minimal. Adapted from [22].

In contrast, the 100 nm target's high energy protons, which reach a higher peak energy of $\sim$ 24 MeV (part (c)), originate throughout the volume of the target. Furthermore, the highest energy protons originate in the *front* 10 nm of the target, and protons which originated between 0 and 90 nm are reflected around $x_i = 90$ nm during their acceleration when compared to their initial positions. Volumetric acceleration and the greatest push being imparted to ions at the front of the target identifies this as RPA. All *experimental* signatures at this target thickness were consistent with TNSA, but these simulations show that these can also be produced through RPA. Bulanov, et al. [168] have also discussed that the characteristic exponential TNSA signature can be produced through RPA at oblique laser incidence – this misidentification may apply to a number of experiments, particularly those with a short pulse.

Finally, in the 30 nm target case, some elements of the acceleration seen in the 100 nm target are present – part (f) shows that the acceleration is also volumetric, and all high

Table 8.3: Energy fraction due to different acceleration mechanisms as a function of target thickness.

Target thickness (nm)	TNSA	RPA	Transparency
300	90%	10%	0%
100	30%	30%	40%
30	0%	0%	100%

energy protons (peak energy now at ~ 32 MeV) are well-mixed with respect to their initial x positions. However, the shape formed by the accelerated protons is qualitatively different than in the two thicker targets (roughly a hemisphere). This is also the first thickness at which a significant portion of the laser pulse is transmitted. The acceleration here is driven by relativistic transparency (possibly Coulomb explosion), which shuts off the initial RPA dynamics.

Using some simple categories to describe these three mechanisms, it is possible to make an estimate of how much energy in high energy protons is due to each mechanism, using the following criteria:

- energy in protons from the rear 10% of the target will be counted as TNSA protons until transparency turns on
- energy in protons from the front 90% of the target will be counted as RPA protons until transparency turns on
- once transparency turns on, all energy gain is counted as transparency-driven.

Applying this, Table 8.3 shows how each of these target's energy in protons can be broken down. Most notably, roughly 40% of the energy imparted to protons from the 100 nm target is due to transparency effects, while all the energy is due to transparency in the 30 nm target simulation. By this analysis method, it is clear there is a transition to RPA for thinner targets as theoretical models would predict, and that the interplay between these effects is complicated to untangle, even in simulations where more information is available.

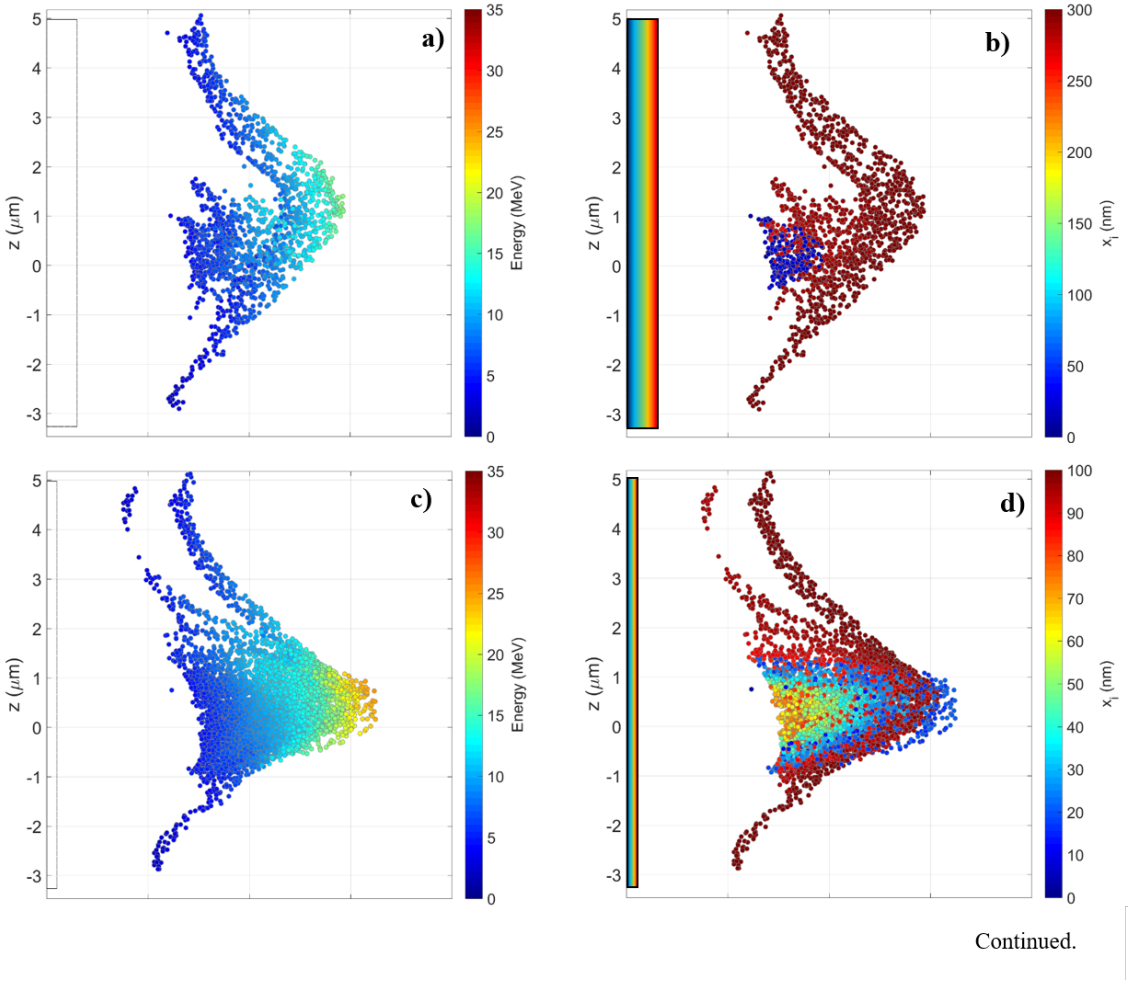

Continued.

Figure 8.8: Analysis of high energy protons within $y_i = \pm 0.3$ μm, shown at $t = t_0 + 50$ fs. (a) Protons from a 300 nm target, colorcoded by energy, with a peak energy of 18 MeV. (b) Protons from a 300 nm target, colorcoded by initial x position; high energy particles originate exclusively in the target front and rear. (c) Protons from a 100 nm target, colorcoded by energy, with a peak energy of 24 MeV. (d) Protons from a 100 nm target, colorcoded by initial x position; high energy particles originate throughout the target volume, with the highest energy protons coming from the front of the target. (e) Protons from a 30 nm target, colorcoded by energy, with a peak energy of 34 MeV. (f) Protons from a 30 nm target, colorcoded by initial x position; high energy particles originate exclusively in the target front and rear and are well mixed.

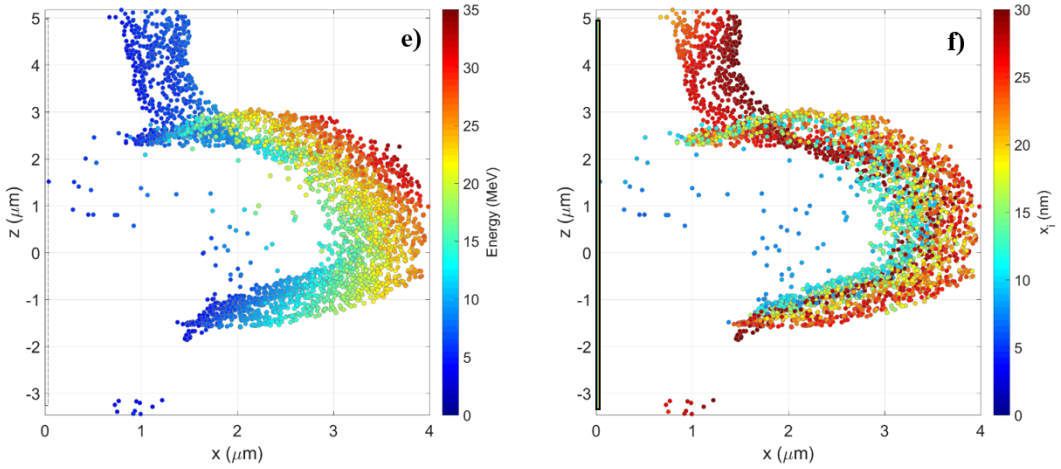

Figure 8.8: Cont.

8.5 Radiation Pressure Description of a Deformable Target

Once RPA is established to be dominant for thinner targets at oblique incidence for these laser and target parameters, it is natural to attempt to extend existing simple RPA models to describe the behavior seen here. In Sec. 8.5.1, an analytical model for the target deformation from radiation pressure is laid out, and it is tested against simulation in Sec. 8.5.2.

8.5.1 Analytical Model for Momentum Transfer at Oblique Incidence

An electromagnetic wave with intensity I transfers its momentum when it hits a surface – at normal incidence, and for a perfect (rigid) reflector, this translates to a radiation pressure $P = 2I/c$. To extend the usual light pressure model to the targets in these simulations, we introduce a deformable target, where the local laser incident angle $\theta_i = \theta_L - \theta_T$ varies with space and time (Fig. 8.9). To begin, we consider the physical meaning of the Maxwell stress tensor $\overleftrightarrow{T}$. T_{ij} is the force per unit area in the ith direction acting on an a surface element oriented normal to the jth direction. To obtain a change in momentum from this, we must

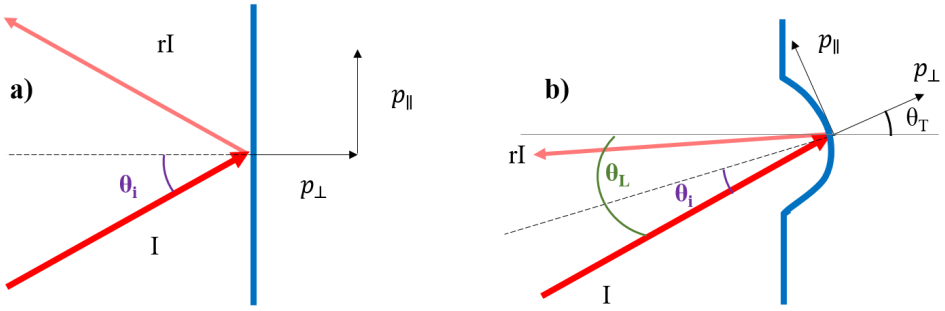

Figure 8.9: Schematic depicting RPA model taking into account a deformable target and oblique laser incidence. (a) The initial state, in which the laser is imperfectly reflected from a flat target, transferring perpendicular and parallel momentum components to the target. (b) A later stage, at which the target was substantially deformed; the transferred momentum can be determined from the laser incident angle and local target normal.

find $d\vec{p}/dt = \left\langle \overleftrightarrow{T} \right\rangle \cdot \vec{dA}$. The definition of the Maxwell stress tensor is given below:

$$T_{ij} = \epsilon_0 \left(E_i E_j - \frac{1}{2}\delta_{ij} E^2 \right) + \frac{1}{\mu_0} \left(B_i B_j - \frac{1}{2}\delta_{ij} B^2 \right). \tag{8.1}$$

To evaluate the elements of this tensor at each point (x_i, z_i) along the surface of the deformed target, we must first rotate into the coordinate system of the incoming laser (Eq. 8.2):

$$\begin{pmatrix} z_L \\ r_L \end{pmatrix} = \begin{pmatrix} cos\theta_i & sin\theta_i \\ -sin\theta_i & cos\theta_i \end{pmatrix} \begin{pmatrix} x_i \\ z_i \end{pmatrix}. \tag{8.2}$$

Any description of the laser electric field could be used here; as LSP uses a Gaussian spatial profile by default, the electric field amplitude for our test case is

$$E(r_L, z_L) = E_0 \frac{\omega_0}{\omega_Z} \exp\left(-\frac{r_L^2}{\omega_L^2} \right) \cos\left(\frac{\pi(t - t_0)}{2a} \right), \tag{8.3}$$

where E_0 is the maximum electric field amplitude, ω_0 is the Gaussian beam waist, and $\omega_L = \omega_0 \sqrt{1 + (z_L/z_R)^2}$ and $z_R = \pi\omega_0^2/\lambda$.

Since the experiment in question was p-polarized, we will do the same with our laser for

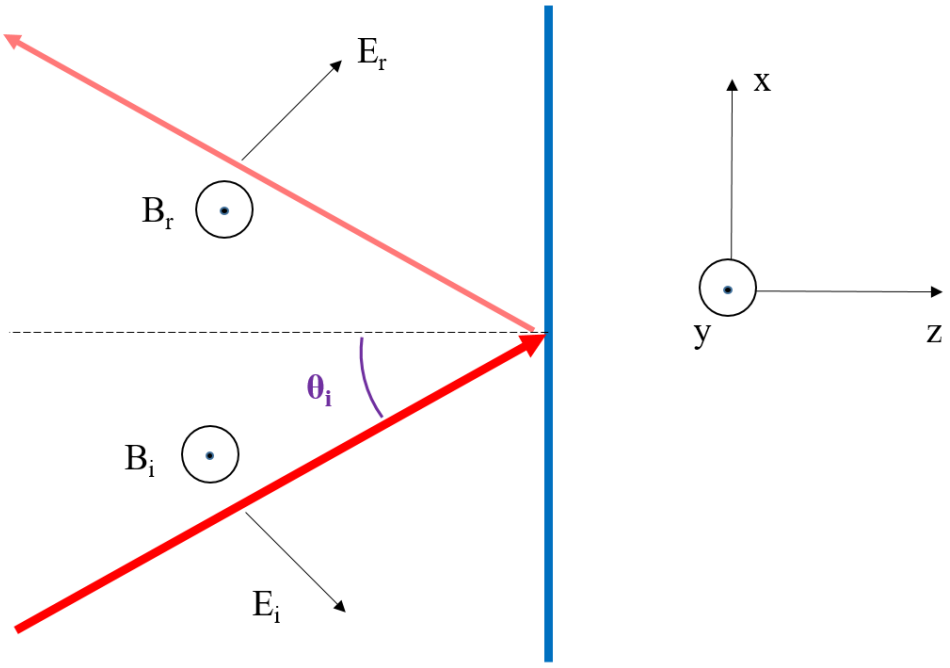

Figure 8.10: Schematic of incoming laser for RPA model derivation in the local target normal frame of reference. An incident p-polarized laser (E in the X and Z directions, B in the Y direction) is reflected from a flat surface with normal vector $-\hat{z}$.

this calculation. Figure 8.10 shows how the directions of E and B are changed on reflection in this case, with the axes defined with respect to the local target normal - we are here restricting ourselves to the plane of polarization. $\overrightarrow{E_i}$ can then be written in those axes as

$$\overrightarrow{E_i} = E(r_L, z_L)\left(-\cos\theta_i \hat{x} + \sin\theta_i \hat{z}\right), \tag{8.4}$$

and $\overrightarrow{E_r}$ as

$$\overrightarrow{E_r} = E(r_L, z_L)\left(r\cos\theta_i \hat{x} + r\sin\theta_i \hat{z}\right), \tag{8.5}$$

where $r < 1$. The magnetic field does not change orientation on reflection, so $\overrightarrow{B_i}$ and

$\overrightarrow{B_r}$ can be written

$$\overrightarrow{B_i} = \frac{E(r_L, z_L)}{c}\hat{y}, \overrightarrow{B_r} = \frac{rE(r_L, z_L)}{c}\hat{y} \tag{8.6}$$

and finally

$$\begin{aligned} \vec{E} = E(r_L, z_L)\left(-\cos\theta_i(1-r)\hat{x} + \sin\theta_i(1+r)\hat{z}\right), \\ \vec{B} = \frac{E(r_L, z_L)}{c}(1+r)\hat{y}. \end{aligned} \tag{8.7}$$

It can be seen from Fig. 8.10 that the surface element $\overrightarrow{dA} = -dA\hat{z}$, so we need only calculate T_{xz}, T_{yz}, and T_{zz}. Due to the directions of the components, T_{yz} vanishes, and we are left with

$$\begin{aligned} T_{xz} = -\epsilon_0 E(r_L, z_L)^2(1-r^2)\cos\theta_i \sin\theta_i, \\ T_{zz} = -\epsilon_0 E(r_L, z_L)^2(1+r^2)\cos^2\theta_i. \end{aligned} \tag{8.8}$$

Finally, using the definition of intensity, taking the cycle average of $E(r_L, z_L)$, and defining $r^2 = R$, we obtain

$$\begin{aligned} \frac{dp_z}{dt} = -\langle T_{zz}\rangle dA = \frac{(1+R)I(r_L, z_L)}{c}\cos^2\theta_i dA, \\ \frac{dp_x}{dt} = -\langle T_{xz}\rangle dA = \frac{(1-R)I(r_L, z_L)}{c} cos\theta_i \sin\theta_i dA. \end{aligned} \tag{8.9}$$

As a sanity check, let us return to the familiar case of normal incidence and perfect reflection, $R = 1$ – we regain $dp_z/dt = 2I/c$, as expected.

8.5.2 Testing Radiation Deformation Model Against Simulation

Now that these expressions have been obtained as a function of $I(r_L, z_L)$, they can be discretized and implemented numerically to compare to the deformation of the target observed in simulations. The assumptions used, in brief, are that

- the entire areal mass of the target is contained in an infinitesimal membrane;

- up until the time of target transparency, R is equal to the time-integrated value obtained from the PIC simulation;
- and after the time of transparency, no further momentum is transferred to the target.

To test this model, a 2D3V simulation was run with the same laser at normal and 45° incidence, but using a target 100 nm thick composed solely of protons and electrons to avoid effects from having ion species with different masses. The position of the protons on a linear scale is shown in Fig. 8.11, overlaid with the position of target curvature predicted using the radiation deformation model for 0° in part (a) and 45° in part (b). The agreement at both angles of incidence is quite good, especially for such a simple model. This strongly suggests that radiation pressure is the dominant acceleration mechanism in this regime.

8.6 Conclusions

3D PIC simulations are necessary to model the expansion of ultrathin targets irradiated at oblique incidence due to their complex geometry. This dimensionality, combined with careful choice of resolution and other parameters, allow atypically good agreement between simulations and proton peak energy, proton angular trajectory, and amount of transmitted light at a range of target thicknesses. Since the simulation set is demonstrably a reasonable match to experimental conditions, it can be used to determine aspects of the acceleration physics that were not apparent from the data. The expected TNSA for thick targets is surpassed by RPA for thinner targets, and by relativistic transparency effects for the thinnest, despite maintaining a target normal acceleration direction for both non-TNSA mechanisms. This is revealed by analyzing the initial positions of protons which attain high energy in each target. The deformation of the target surface can be attributed to RPA, for which a simple analytical model has been developed.

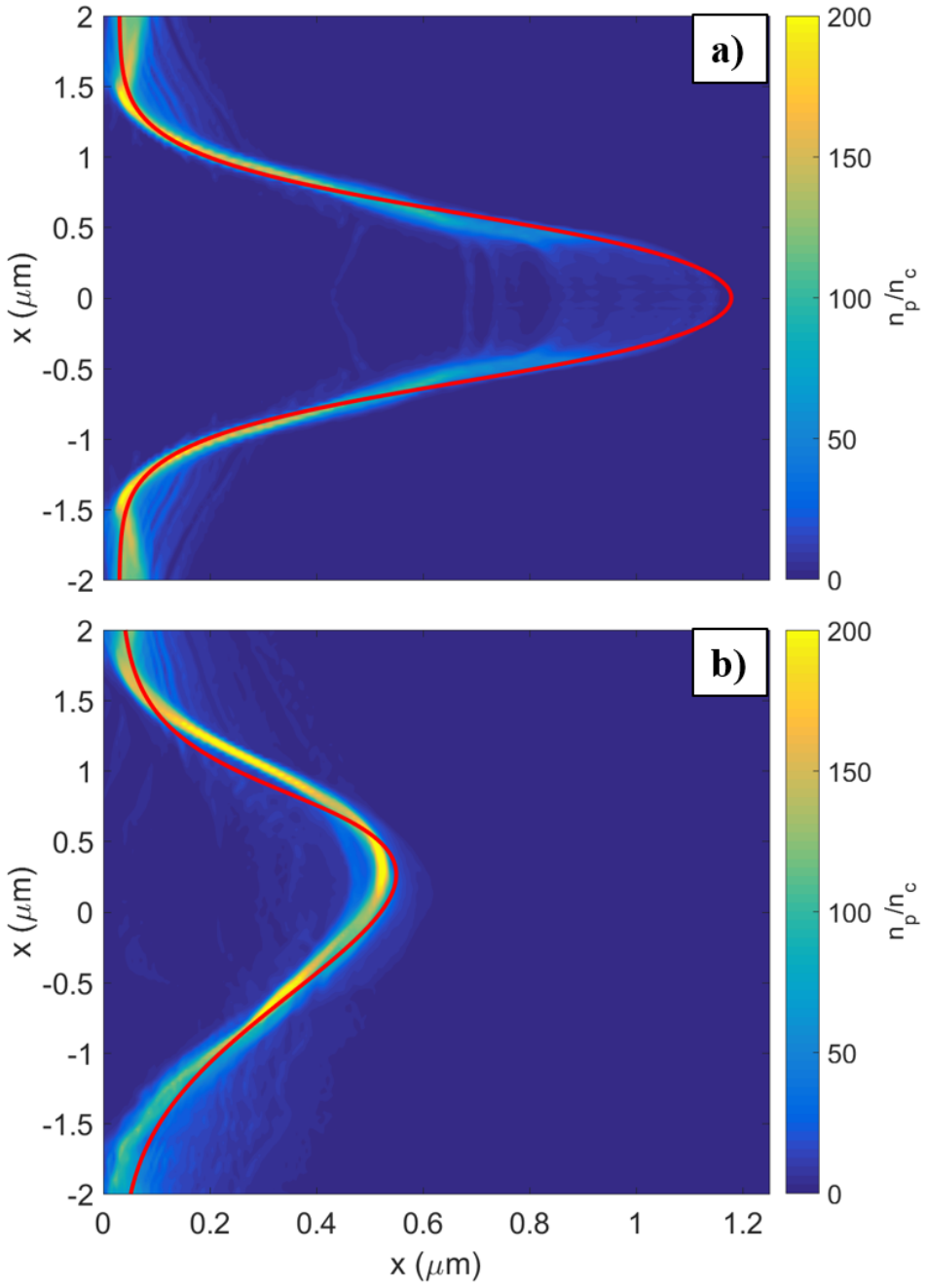

Figure 8.11: Testing deformable target RPA model against 2D simulations using a 100 nm fully ionized hydrogen target. (a) Deformation from a normally incident laser at $t = t_0 + 35$ fs; colored contour indicates proton density, normalized with respect to n_c, with overlaid red outline of deformable target RPA model prediction. (b) Deformation from a 45° incident laser at $t = t_0 + 35$ fs; colored contour indicates proton density, normalized with respect to n_c, with overlaid red outline of deformable target RPA model prediction.

Chapter 9
Conclusions

As discussed in Chapter 1, the generation of secondary radiation in general, and laser ion acceleration in particular, is a prominent aspect of the relativistic laser-plasma interaction. One thing that distinguishes the plasma state from that of solid, liquid, or gas is that increasing amounts of energy can be deposited without additional phase changes. The possibility exists to drive the system to extremes, seemingly without limit, and this is fundamentally interesting. This requires that the energy be deposited rapidly before the target can disassemble, hence the need for ultrafast laser systems. Moreover, ion acceleration is already useful as a probe of the laser plasma interaction, for example, of evolving magnetic fields, and it has the potential to be a competitive source for neutron radiography and cancer therapy. Much of the research in this field focuses on controlling yield, peak energy, and spectrum of accelerated ions through choice of laser intensity and contrast, and target material and thickness. With the possible exception of TNSA, the underlying mechanisms that accelerate ions are not sufficiently well understood, due in part to limits in existing data. Existing lasers are limited in their shot rate, and targets are slow to align and can be expensive to fabricate. As a result, many ion acceleration studies have only 20-30 usable shots, which makes it difficult to assess trends with target thickness or other key factors. Different laser systems with nominally similar pulse characteristics and targets can produce significantly different results because of their pre-pulse, the effect of which is not always well understood.

It is now commonplace for reports of experimental results in the literature to be comple-

mented by PIC simulations as described in Chapter 3, which can give insight into dynamics that are not visible to experimental diagnostics. PIC simulations can also play a key role in the design of experiments by treating several target designs so that the most advantageous can be fabricated. One of the exciting developments underway that might significantly change our understanding of laser based ion acceleration, and high energy density laser-based experiments in general, is the development of high repetition rate petawatt-class lasers with their promise of larger data sets and better statistics. Several ultraintense lasers with repetition rates in excess of 1 Hz are already in operation, with some laser facilities planned to come online within the next few years with shot rates greater than 10 Hz. I have continued the work in high repetition rate plasma mirror and target development begun by past members of my group, as detailed in Chapter 5.

Chapter 4 discusses how an electron accelerated via direct laser acceleration in an ultraintense wave becomes harder to model as the wave intensity increases, due to the difficulty of resolving the stopping points in the electron trajectory. I identified which part of the PIC computation cycle was responsible for this inaccuracy, the Boris pusher, and derived the criterion on the timestep required to correctly resolve electron motion in this regime, $\Delta t \ll T/a_0$, where a_0 is the dimensionless vector potential. An adaptive time step algorithm based on this criterion is also presented which improves the scaling in number of timesteps required to resolve the electron motion by a factor of $1/\sqrt{a_0}$. Direct laser acceleration of electrons in a low density plasma occurs naturally in some laser-plasma interactions, for example those with structured targets; this work will improve the accuracy of simulations of these phenomena.

High pulse contrast is crucial for performing many experiments using high intensity lasers in order to minimize modification of the target surface by pre-pulse. Dielectric plasma mirrors are commonly used to enhance the contrast of laser pulses and their subsequent ion production, but have not been modeled extensively. In Ch. 6, I described my development of a PIC framework using LSP for simulations of dielectric plasma mirrors and demonstrated its use for plasma mirrors made of thin, free-standing liquid crystal films. The simulations include a dielectric model, multiphoton ionization, low temperature modifications to the

collision model, and dimensionality corrections, allowing less expensive simulations to be used. For the first time in the literature, I modeled plasma mirror behavior as a function of laser intensity, with excellent agreement to experiment over three orders of magnitude. In the future, this simulation framework can be used to make predictions of plasma mirror behavior on aspects that are difficult to measure, such as pulse shortening and laser spatial mode degradation at full power.

Results from a high-contrast, ion acceleration experiment I helped conduct were presented in Ch. 7. The Draco laser ($\sim$3 J, 10^{21} W/cm^2) at 45° angle of incidence on liquid crystal targets was used to collect 450 shots in 5 days with each shot having up to 9 diagnostics in use. The data showed predominantly target normal directed ions for all target thicknesses from > 1 μm down to 10 nm, with peak protons energies up to 26 MeV found for the thinnest targets. Target normal ions are often considered to be an indication of the target normal sheath acceleration (TNSA) mechanism, but the TNSA-like signal in this experiment persisted down to target thicknesses < 30 nm, well under the predicted theoretical transition to radiation pressure acceleration (RPA) of $\sim$ 130 nm for these conditions. The range of target thicknesses with the same target material was larger in this experiment than in any other at the time it was conducted, so far as we know.

Chapter 8 discussed 3D particle-in-cell simulations I conducted using LSP which reproduce the dominance of target normal acceleration seen in the DRACO experiment.These simulations agree well with experimental peak proton energies, direction of emitted ions, and trends in amount of transmitted light. Tracking individual particles in simulations revealed that target normally directed ions are produced by TNSA for thick targets, but by RPA for thin targets. I derived a simple analytical model for RPA-driven target deformation that agrees well with 2D and 3D simulation results, supporting this conclusion. Using these simulations, the amount of energy in accelerated protons can be broken down into TNSA and RPA contributions. For a 300 nm target, TNSA makes up 90% of this energy with RPA contributing 10%, while in a 100 nm target TNSA and RPA each make up 30%, with the remaining due to relativistic transparency effects. The simulations here show that multiple ion acceleration mechanisms can produce target normally directed ions under these

laser conditions; existing understanding of when TNSA and RPA are dominant may need to be reevaluated. Also, I explored the conditions necessary for performing valid simulations for ultrashort pulses incident on very thin, solid density targets - a key regime for effective ion acceleration. Although 2D3V simulations are still the most commonly performed, simulations in 3D were found to be vital to not exaggerate the strength of the accelerating fields. Cell sizes comparable to the Debye length were also found to be important which is difficult to achieve in this regime. It was found that an initial target temperature could be found that was a reasonable compromise between having sufficiently small cells and avoiding excessive target expansion.

In total, this research has advanced the field of high energy density physics by using a combined computational and experimental approach to study the regime of relativistic laser-plasma interactions. Simulations must necessarily make approximations, either by not treating selected physical processes (eg. different types of collisions, different ionization and recombination processes, cold target condensed matter properties, and more) or compromising on numerical aspects (eg. grid size and temporal extent, resolution in space and time, etc.) There are multiple natural temporal and spatial scales given by the plasma frequency, Debye length, laser period and wavelength, cyclotron frequency, collision rate, and more that might be important for a valid physical representation or for achieving numerical stability. In a similar vein, experiments may not be as well diagnosed as one would like: targets can oxidize or deform after they are prepared or become coated with debris after mounting in the experiment, laser pre-pulse is often not known well, the laser spot size at high power is difficult to measure and low power measurements may not represent actual experimental conditions, beam pointing jitter can result in variation of the spot size on the target when at non-normal incidence, and more. Most experimental diagnostics are time-integrated and their connection to the desired physics can be indirect. The close interplay of numerical modeling and experiment is a necessary outcome of work to overcome these challenges. Experiments are vital to validate the many approximations used in simulations and simulations are equally vital to interpret experiment and to address its sensitivity to error. The work described here has advanced both these aspects. Although specific issues

have been addressed (eg. how best to perform simulations of highly relativistic electron acceleration or how to use the unusual properties of liquid crystals to facilitate ion acceleration experiments), we hope the results will be far-reaching. Higher intensity lasers are coming on-line that will challenge current PIC models, higher repetition rate lasers have also become available which require high repetition rate plasma mirrors and target insertion, there is growing interest in using plasma mirrors for longer pulse lasers which requires better plasma mirror modeling, and ion acceleration is still not sufficiently well understood. This work can benefit each of these issues and likely more.

Bibliography

[1] Shih Helen A., Sherman Janet C., Nachtigall Lisa B., Colvin Mary K., Fullerton Barbara C., Daartz Juliane, Winrich Barbara K., Batchelor Tracy T., Thornton Lauren T., Mancuso Sarah M., Saums Michele K., Oh Kevin S., Curry William T., Loeffler Jay S., and Yeap Beow Y. Proton therapy for low-grade gliomas: Results from a prospective trial. *Cancer*, 121(10):1712–1719, 2015.

[2] Example of neutron vs. x-ray imaging. https://www.psi.ch/niag/what-is-neutron-imaging. Accessed 07/12/2018.

[3] Kane Yee. Numerical solution of initial boundary value problems involving maxwell's equations in isotropic media. *IEEE Transactions on Antennas and Propagation*, 14(3):302–307, May 1966.

[4] Charles K. Birdsall and A. Bruce Langdon. *Plasma physics via computer simulation*. CRC press, 2004.

[5] Alexey V. Arefiev, Ginevra E. Cochran, Douglass W. Schumacher, Alexander P. L. Robinson, and Guangye Chen. Temporal resolution criterion for correctly simulating relativistic electron motion in a high-intensity laser field. *Physics of Plasmas*, 22(1):013103, 2015.

[6] P. L. Poole, C. Willis, G. E. Cochran, R. T. Hanna, C. D. Andereck, and D. W. Schumacher. Moderate repetition rate ultra-intense laser targets and optics using variable thickness liquid crystal films. *Applied Physics Letters*, 109(15), 2016.

[7] P. L. Poole, C. Willis, R. L. Daskalova, K. M. George, S. Feister, S. Jiang, J. Snyder, J. Marketon, D. W. Schumacher, K. U. Akli, L. Van Woerkom, R. R. Freeman, and E. A. Chowdhury. Experimental capabilities of 0.4 PW, 1 shot/min Scarlet laser facility for high energy density science. *Applied Optics*, 55(17):4713–4719, June 2016.

[8] P. L. Poole, A. Krygier, G. E. Cochran, P. S. Foster, G. G. Scott, L. A. Wilson, J. Bailey, N. Bourgeois, C. Hernandez-Gomez, D. Neely, P. P. Rajeev, and D. W. Schumacher. Experiment and simulation of novel liquid crystal plasma mirrors for high contrast, intense laser pulses. *Scientific Reports*, 6:32041, 2016.

[9] F. Wagner, O. Deppert, C. Brabetz, P. Fiala, A. Kleinschmidt, P. Poth, V.A. Schanz, A. Tebartz, B. Zielbauer, M. Roth, T. Stöhlker, and V. Bagnoud. Maximum Proton

Energy above 85 MeV from the Relativistic Interaction of Laser Pulses with Micrometer Thick CH2 Targets. *Physical Review Letters*, 116(20):205002, 2016.

[10] D. Neely, P. Foster, A. Robinson, F. Lindau, O. Lundh, A. Persson, C.-G. Wahlstrm, and P. McKenna. Enhanced proton beams from ultrathin targets driven by high contrast laser pulses. *Applied Physics Letters*, 89(2):021502, 2006.

[11] T. Ceccotti, A. Lévy, H. Popescu, F. Réau, P. D'Oliveira, P. Monot, J. P. Geindre, E. Lefebvre, and Ph Martin. Proton acceleration with high-intensity ultrahigh-contrast laser pulses. *Physical Review Letters*, 99(18):1–4, 2007.

[12] D C Carroll, O Tresca, R Prasad, L Romagnani, P S Foster, P Gallegos, S Ter-Avetisyan, J S Green, M J V Streeter, N Dover, C A J Palmer, C M Brenner, F H Cameron, K E Quinn, J Schreiber, A P L Robinson, T Baeva, M N Quinn, X H Yuan, Z Najmudin, M Zepf, D Neely, M Borghesi, and P McKenna. Carbon ion acceleration from thin foil targets irradiated by ultrahigh-contrast, ultraintense laser pulses. *New Journal of Physics*, 12(4):045020, 2010.

[13] K Zeil, S D Kraft, S Bock, M Bussmann, T E Cowan, T Kluge, J Metzkes, T Richter, R Sauerbrey, and U Schramm. The scaling of proton energies in ultrashort pulse laser plasma acceleration. *New Journal of Physics*, 12(4):045015, 2010.

[14] J. S. Green, A. P. L. Robinson, N. Booth, D. C. Carroll, R. J. Dance, R. J. Gray, D. A. MacLellan, P. McKenna, C. D. Murphy, D. Rusby, and L. Wilson. High efficiency proton beam generation through target thickness control in femtosecond laser-plasma interactions. *Applied Physics Letters*, 104(21):214101, 2014.

[15] A. J. Mackinnon, Y. Sentoku, P. K. Patel, D. W. Price, S. Hatchett, M. H. Key, C. Andersen, R. Snavely, and R. R. Freeman. Enhancement of proton acceleration by hot-electron recirculation in thin foils irradiated by ultraintense laser pulses. *Phys. Rev. Lett.*, 88:215006, May 2002.

[16] N P Dover, C A J Palmer, M J V Streeter, H Ahmed, B Albertazzi, M Borghesi, D C Carroll, J Fuchs, R Heathcote, P Hilz, K F Kakolee, S Kar, R Kodama, A Kon, D A MacLellan, P McKenna, S R Nagel, D Neely, M M Notley, M Nakatsutsumi, R Prasad, G Scott, M Tampo, M Zepf, J Schreiber, and Z Najmudin. Buffered high charge spectrally-peaked proton beams in the relativistic-transparency regime. *New Journal of Physics*, 18(1):013038, 2016.

[17] A. Henig, D. Kiefer, K. Markey, D. C. Gautier, K. A. Flippo, S. Letzring, R. P. Johnson, T. Shimada, L. Yin, B. J. Albright, K. J. Bowers, J. C. Fernández, S. G. Rykovanov, H.-C. Wu, M. Zepf, D. Jung, V. Kh. Liechtenstein, J. Schreiber, D. Habs, and B. M. Hegelich. Enhanced laser-driven ion acceleration in the relativistic transparency regime. *Phys. Rev. Lett.*, 103:045002, Jul 2009.

[18] I Jong Kim, Ki Hong Pae, Chul Min Kim, Hyung Taek Kim, Jae Hee Sung, Seong Ku Lee, Tae Jun Yu, Il Woo Choi, Chang-Lyoul Lee, Kee Hwan Nam, Peter V. Nickles, Tae Moon Jeong, and Jongmin Lee. Transition of proton energy scaling using an ultrathin target irradiated by linearly polarized femtosecond laser pulses. *Phys. Rev. Lett.*, 111:165003, 2013.

[19] F. Dollar, P. Cummings, V. Chvykov, L. Willingale, M. Vargas, V. Yanovsky, C. Zulick, A. Maksimchuk, A. G. R. Thomas, and K. Krushelnick. Scaling high-order harmonic generation from laser-solid interactions to ultrahigh intensity. *Phys. Rev. Lett.*, 110:175002, Apr 2013.

[20] D Jung, B J Albright, L Yin, D C Gautier, R Shah, S Palaniyappan, S Letzring, B Dromey, H-C Wu, T Shimada, R P Johnson, M Roth, J C Fernandez, D Habs, and B M Hegelich. Beam profiles of proton and carbon ions in the relativistic transparency regime. *New Journal of Physics*, 15(12):123035, 2013.

[21] I. Jong Kim, Ki Hong Pae, Il Woo Choi, Chang-Lyoul Lee, Hyung Taek Kim, Himanshu Singhal, Jae Hee Sung, Seong Ku Lee, Hwang Woon Lee, Peter V. Nickles, Tae Moon Jeong, Chul Min Kim, and Chang Hee Nam. Radiation pressure acceleration of protons to 93mev with circularly polarized petawatt laser pulses. *Physics of Plasmas*, 23(7):070701, 2016.

[22] P L Poole, L Obst, G E Cochran, J Metzkes, H-P Schlenvoigt, I Prencipe, T Kluge, T Cowan, U Schramm, D W Schumacher, and K Zeil. Laser-driven ion acceleration via target normal sheath acceleration in the relativistic transparency regime. *New Journal of Physics*, 20(1):013019, 2018.

[23] J.E. Sansonetti and W.C. Martin. Handbook of Basic Atomic Spectroscopic Data. *Journal of Physical and Chemical Reference Data*, 34(4):1559–2259, 2005.

[24] S.G. Lias. *NIST Chemistry WebBook, NIST Standard Reference Database Number 69*, chapter Ionization Energy Evaluation. National Institute of Standards and Technology, Gaithersburg MD, 20899, 2018.

[25] W.P. Leemans, A.J. Gonsalves, H.-S. Mao, K. Nakamura, C. Benedetti, C.B. Schroeder, Cs. Tóth, J. Daniels, D.E. Mittelberger, S.S. Bulanov, J.-L. Vay, C.G.R. Geddes, and E. Esarey. Multi-gev electron beams from capillary-discharge-guided subpetawatt laser pulses in the self-trapping regime. *Phys. Rev. Lett.*, 113:245002, 2014.

[26] Margaret M. Murnane, Henry C. Kapteyn, Mordecai D. Rosen, and Roger W. Falcone. Ultrafast x-ray pulses from laser-produced plasmas. *Science*, 251(4993):531–536, 1991.

[27] K. W. D. Ledingham, P. McKenna, and R. P. Singhal. Applications for nuclear phenomena generated by ultra-intense lasers. *Science*, 300(5622):1107–1111, 2003.

[28] Hui Chen, S. C. Wilks, J. D. Bonlie, S. N. Chen, K. V. Cone, L. N. Elberson, G. Gregori, D. D. Meyerhofer, J. Myatt, D. F. Price, M. B. Schneider, R. Shepherd, D. C. Stafford, R. Tommasini, R. Van Maren, and P. Beiersdorfer. Making relativistic positrons using ultraintense short pulse lasers. *Physics of Plasmas*, 16(12), 2009.

[29] Teresa Bartal, Mark E. Foord, Claudio Bellei, Michael J. Key, Kirk A. Flippo, Sandrine A. Gaillard, Dustin T. Offerman, Pravesh K. Patel, Leonard C. Jarrott, Drew P. Higginson, Markus Roth, Anke Otten, Dominik Kraus, Richard B. Stephens, Harry S. McLean, Emilio M. Giraldez, Mighsheng S. Wei, Donald C. Gautier, and Farhat N. Beg. Focusing of short-pulse high-intensity laser-accelerated proton beams. *Nat Phys*, 8(2):139–142, 2012.

[30] M Roth, I Alber, V Bagnoud, C R D Brown, R Clarke, H Daido, J Fernandez, K Flippo, S Gaillard, C Gauthier, M Geissel, S Glenzer, G Gregori, M Gnther, K Harres, R Heathcote, A Kritcher, N Kugland, S LePape, B Li, M Makita, J Mithen, C Niemann, F Nrnberg, D Offermann, A Otten, A Pelka, D Riley, G Schaumann, M Schollmeier, J Schtrumpf, M Tampo, A Tauschwitz, and An Tauschwitz. Proton acceleration experiments and warm dense matter research using high power lasers. *Plasma Physics and Controlled Fusion*, 51(12):124039, 2009.

[31] S. V. Bulanov, H. Daido, T. Zh. Esirkepov, V. S. Khoroshkov, J. Koga, K. Nishihara, F. Pegoraro, T. Tajima, and M. Yamagiwa. Feasibility of using laser ion accelerators in proton therapy. *AIP Conference Proceedings*, 740(1):414–429, 2004.

[32] S D Kraft, C Richter, K Zeil, M Baumann, E Beyreuther, S Bock, M Bussmann, T E Cowan, Y Dammene, W Enghardt, U Helbig, L Karsch, T Kluge, L Laschinsky, E Lessmann, J Metzkes, D Naumburger, R Sauerbrey, M. Schrer, M Sobiella, J Woithe, U Schramm, and J Pawelke. Dose-dependent biological damage of tumour cells by laser-accelerated proton beams. *New Journal of Physics*, 12(8):085003, 2010.

[33] A. Yogo, T. Maeda, T. Hori, H. Sakaki, K. Ogura, M. Nishiuchi, A. Sagisaka, H. Kiriyama, H. Okada, S. Kanazawa, T. Shimomura, Y. Nakai, M. Tanoue, F. Sasao, P. R. Bolton, M. Murakami, T. Nomura, S. Kawanishi, and K. Kondo. Measurement of relative biological effectiveness of protons in human cancer cells using a laser-driven quasimonoenergetic proton beamline. *Applied Physics Letters*, 98(5):053701, 2011.

[34] K. Zeil, M. Baumann, E. Beyreuther, T. Burris-Mog, T. E. Cowan, W. Enghardt, L. Karsch, S. D. Kraft, L. Laschinsky, J. Metzkes, D. Naumburger, M. Oppelt, C. Richter, R. Sauerbrey, M. Schürer, U. Schramm, and J. Pawelke. Dose-controlled irradiation of cancer cells with laser-accelerated proton pulses. *Applied Physics B*, 110(4):437–444, 2013.

[35] Y. Ping, R. Shepherd, B. F. Lasinski, M. Tabak, H. Chen, H. K. Chung, K. B. Fournier, S. B. Hansen, A. Kemp, D. A. Liedahl, K. Widmann, S. C. Wilks, W. Rozmus, and M. Sherlock. Absorption of short laser pulses on solid targets in the ultrarelativistic regime. *Phys. Rev. Lett.*, 100:085004, Feb 2008.

[36] K. Krushelnick, A. Ting, C. I. Moore, H. R. Burris, E. Esarey, P. Sprangle, and M. Baine. Plasma channel formation and guiding during high intensity short pulse laser plasma experiments. *Phys. Rev. Lett.*, 78:4047–4050, May 1997.

[37] A. Pukhov and J. Meyer-ter Vehn. Laser hole boring into overdense plasma and relativistic electron currents for fast ignition of icf targets. *Phys. Rev. Lett.*, 79:2686–2689, Oct 1997.

[38] R. Fedosejevs, I. V. Tomov, N. H. Burnett, G. D. Enright, and M. C. Richardson. Self-steepening of the density profile of a co_2-laser-produced plasma. *Phys. Rev. Lett.*, 39:932–935, Oct 1977.

[39] B. Chrisman, Y. Sentoku, and A. J. Kemp. Intensity scaling of hot electron energy coupling in cone-guided fast ignition. *Physics of Plasmas*, 15(5):056309, 2008.

[40] W. L. Kruer and Kent Estabrook. Jb heating by very intense laser light. *The Physics of Fluids*, 28(1):430–432, 1985.

[41] F. Brunel. Not-so-resonant, resonant absorption. *Phys. Rev. Lett.*, 59:52–55, Jul 1987.

[42] Kent Estabrook and W. L. Kruer. Properties of resonantly heated electron distributions. *Phys. Rev. Lett.*, 40:42–45, Jan 1978.

[43] Michael E. Glinsky. Regimes of suprathermal electron transport. *Physics of Plasmas*, 2(7):2796–2806, 1995.

[44] J. Fuchs, C. A. Cecchetti, M. Borghesi, T. Grismayer, E. d'Humières, P. Antici, S. Atzeni, P. Mora, A. Pipahl, L. Romagnani, A. Schiavi, Y. Sentoku, T. Toncian, P. Audebert, and O. Willi. Laser-foil acceleration of high-energy protons in small-scale plasma gradients. *Phys. Rev. Lett.*, 99:015002, Jul 2007.

[45] W. Kruer. *The Physics of Laser Plasma Interactions*. Addison-Wesley, New York, 1988.

[46] Erich S. Weibel. Stable orbits of charged particles in an oscillating electromagnetic field. *Phys. Rev.*, 114:18–21, Apr 1959.

[47] L. Biermann. Uber den ursprung der magnetfelder auf sternen und im interstellaren raum (mit einem anhang von a. schluter). *Zs. Naturforschung*, 5a:65, 1950.

[48] M. D. Perry, D. Pennington, B. C. Stuart, G. Tietbohl, J. A. Britten, C. Brown, S. Herman, B. Golick, M. Kartz, J. Miller, H. T. Powell, M. Vergino, and V. Yanovsky. Petawatt laser pulses. *Opt. Lett.*, 24(3):160–162, Feb 1999.

[49] Ronald L. Bishop and M. James Blackman. Instrumental neutron activation analysis of archaeological ceramics: scale and interpretation. *Accounts of Chemical Research*, 35(8):603–610, 2002. PMID: 12186564.

[50] M. Roth, D. Jung, K. Falk, N. Guler, O. Deppert, M. Devlin, A. Favalli, J. Fernandez, D. Gautier, M. Geissel, R. Haight, C. E. Hamilton, B. M. Hegelich, R. P. Johnson, F. Merrill, G. Schaumann, K. Schoenberg, M. Schollmeier, T. Shimada, T. Taddeucci, J. L. Tybo, F. Wagner, S. A. Wender, C. H. Wilde, and G. A. Wurden. Bright laser-driven neutron source based on the relativistic transparency of solids. *Phys. Rev. Lett.*, 110:044802, Jan 2013.

[51] A. Kleinschmidt, V. Bagnoud, O. Deppert, A. Favalli, S. Frydrych, J. Hornung, D. Jahn, G. Schaumann, A. Tebartz, F. Wagner, G. Wurden, B. Zielbauer, and M. Roth. Intense, directed neutron beams from a laser-driven neutron source at phelix. *Physics of Plasmas*, 25(5):053101, 2018.

[52] Alden Curtis, Chase Calvi, James Tinsley, Reed Hollinger, Vural Kaymak, Alexander Pukhov, Shoujun Wang, Alex Rockwood, Yong Wang, Vyacheslav N. Shlyaptsev, and Jorge J. Rocca. Micro-scale fusion in dense relativistic nanowire array plasmas. *Nature Communications*, 9(1):1077, March 2018.

[53] T. Ditmire, J. Zweiback, V. P. Yanovsky, T. E. Cowan, G. Hays, and K. B. Wharton. Nuclear fusion from explosions of femtosecond laser-heated deuterium clusters. *Nature*, 398:489, April 1999.

[54] P A Norreys, A P Fews, F N Beg, A R Bell, A E Dangor, P Lee, M B Nelson, H Schmidt, M Tatarakis, and M D Cable. Neutron production from picosecond laser irradiation of deuterated targets at intensities of 10^{19} w/cm^2. *Plasma Physics and Controlled Fusion*, 40(2):175, 1998.

[55] M. Schollmeier, A. B. Sefkow, M. Geissel, A. V. Arefiev, K. A. Flippo, S. A. Gaillard, R. P. Johnson, M. W. Kimmel, D. T. Offermann, P. K. Rambo, J. Schwarz, and T. Shimada. Laser-to-hot-electron conversion limitations in relativistic laser matter interactions due to multi-picosecond dynamics. *Physics of Plasmas*, 22(4):043116, April 2015.

[56] R. W. Hockney and J. W. Eastwood. *Computer simulations using particles*. CRC Press, 1988.

[57] D.R. Welch, D.V. Rose, R.E. Clark, T.C. Genoni, and T.P. Hughes. Implementation of an non-iterative implicit electromagnetic field solver for dense plasma simulation. *Proceedings of the 18th International Conferene on the Numerical Simulation of Plasmas*, 164(1):183–188, December 2004.

[58] M. King, R.J. Gray, H.W. Powell, D.A. MacLellan, B. Gonzalez-Izquierdo, L.C. Stockhausen, G.S. Hicks, N.P. Dover, D.R. Rusby, D.C. Carroll, H. Padda, R. Torres, S. Kar, R.J. Clarke, I.O. Musgrave, Z. Najmudin, M. Borghesi, D. Neely, and P. McKenna. Ion acceleration and plasma jet formation in ultra-thin foils undergoing expansion and relativistic transparency. *Nuclear Instruments and Methods in Physics Research Section A: Accelerators, Spectrometers, Detectors and Associated Equipment*, 829:163 – 166, 2016. 2nd European Advanced Accelerator Concepts Workshop - EAAC 2015.

[59] J.P. Boris. Relativistic plasma simulation-optimization of a hybrid code. *Proceedings of the Fourth Conference on Numerical Simulation Plasmas*, 1970.

[60] F Fiuza, M Marti, R A Fonseca, L O Silva, J Tonge, J May, and W B Mori. Efficient modeling of laserplasma interactions in high energy density scenarios. *Plasma Physics and Controlled Fusion*, 53(7):074004, 2011.

[61] R. Courant, K. Friedrichs, and H. Lewy. Über die partiellen differenzengleichungen der mathematischen physik. *Mathematische Annalen*, 100(1):32–74, Dec 1928.

[62] F. King. *Simulations of High-Intensity Short-Pulse Lasers Incident on Reduced Mass Targets*. PhD thesis, The Ohio State University, 2015. Retrieved from https://etd.ohiolink.edu/.

[63] S. P. D. Mangles, C. D. Murphy, Z. Najmudin, A. G. R. Thomas, J. L. Collier, A. E. Dangor, E. J. Divall, P. S. Foster, J. G. Gallacher, C. J. Hooker, D. A. Jaroszynski, A. J. Langley, W. B. Mori, P. A. Norreys, F. S. Tsung, R. Viskup, B. R. Walton, and K. Krushelnick. Monoenergetic beams of relativistic electrons from intense laser-plasma interactions. *Nature*, 431(7008):535–538, September 2004.

[64] C. G. R. Geddes, Cs Toth, J. van Tilborg, E. Esarey, C. B. Schroeder, D. Bruhwiler, C. Nieter, J. Cary, and W. P. Leemans. High-quality electron beams from a laser wakefield accelerator using plasma-channel guiding. *Nature*, 431(7008):538–541, September 2004.

[65] J. Faure, Y. Glinec, A. Pukhov, S. Kiselev, S. Gordienko, E. Lefebvre, J.-P. Rousseau, F. Burgy, and V. Malka. A laserplasma accelerator producing monoenergetic electron beams. *Nature*, 431(7008):541–544, September 2004.

[66] Alexey V. Arefiev, Vladimir N. Khudik, and Marius Schollmeier. Enhancement of laser-driven electron acceleration in an ion channel. *Physics of Plasmas*, 21(3):033104, March 2014.

[67] Alexey V. Arefiev, Boris N. Breizman, Marius Schollmeier, and Vladimir N. Khudik. Parametric Amplification of Laser-Driven Electron Acceleration in Underdense Plasma. *Physical Review Letters*, 108(14):145004, April 2012.

[68] A. P. L. Robinson, A. V. Arefiev, and D. Neely. Generating "Superponderomotive" Electrons due to a Non-Wake-Field Interaction between a Laser Pulse and a Longitudinal Electric Field. *Physical Review Letters*, 111(6):065002, August 2013.

[69] S.-W. Bahk, P. Rousseau, T. A. Planchon, V. Chvykov, G. Kalintchenko, A. Maksimchuk, G. A. Mourou, and V. Yanovsky. Generation and characterization of the highest laser intensities (10^{22} W/cm^2). *Optics Letters*, 29(24):2837–2839, December 2004.

[70] See www.eli-laser.eu for Extreme Light Infrastructure European Project.

[71] S. A. Gaillard, T. Kluge, K. A. Flippo, M. Bussmann, B. Gall, T. Lockard, M. Geissel, D. T. Offermann, M. Schollmeier, Y. Sentoku, and T. E. Cowan. Increased laser-accelerated proton energies via direct laser-light-pressure acceleration of electrons in microcone targets. *Physics of Plasmas*, 18(5):056710, May 2011.

[72] T. Kluge, S. A. Gaillard, K. A. Flippo, T. Burris-Mog, W. Enghardt, B. Gall, M. Geissel, A. Helm, S. D. Kraft, T Lockard, J. Metzkes, D. T. Offermann, M. Schollmeier, U. Schramm, K. Zeil, M. Bussmann, and T. E. Cowan. High proton energies from cone targets: electron acceleration mechanisms. *New Journal of Physics*, 14(2):023038, 2012.

[73] A. G. Krygier, D. W. Schumacher, and R. R. Freeman. On the origin of superhot electrons from intense laser interactions with solid targets having moderate scale length preformed plasmas. *Physics of Plasmas*, 21(2):023112, February 2014.

[74] A. Zhidkov, J. Koga, A. Sasaki, and M. Uesaka. Radiation Damping Effects on the Interaction of Ultraintense Laser Pulses with an Overdense Plasma. *Physical Review Letters*, 88(18):185002, April 2002.

[75] L.L. Ji, A. Pukhov, I.Yu. Kostyukov, B.F. Shen, and K. Akli. Radiation-Reaction Trapping of Electrons in Extreme Laser Fields. *Physical Review Letters*, 112(14):145003, April 2014.

[76] A. M. Fedotov, N. B. Narozhny, G. Mourou, and G. Korn. Limitations on the Attainable Intensity of High Power Lasers. *Physical Review Letters*, 105(8):080402, August 2010.

[77] T.J.M. Boyd and J.J. Sanderson. *The Physics of Plasmas*. Cambridge University Press, 2003.

[78] Brendan B. Godfrey and Jean-Luc Vay. Numerical stability of relativistic beam multidimensional PIC simulations employing the Esirkepov algorithm. *Journal of Computational Physics*, 248:33–46, September 2013.

[79] J.-L. Vay. Simulation of beams or plasmas crossing at relativistic velocity. *Physics of Plasmas*, 15(5):056701, February 2008.

[80] T.Zh. Esirkepov. Exact charge conservation scheme for Particle-in-Cell simulation with an arbitrary form-factor. *Computer Physics Communications*, 135(2):144–153, April 2001.

[81] B. Cohen. *Multiple Time Scales*. Academic Press, 1985.

[82] G. Chen and L. Chacn. An energy- and charge-conserving, nonlinearly implicit, electromagnetic 1d-3v VlasovDarwin particle-in-cell algorithm. *Computer Physics Communications*, 185(10):2391–2402, October 2014.

[83] D. R. Welch, D. V. Rose, M. E. Cuneo, R. B. Campbell, and T. A. Mehlhorn. Integrated simulation of the generation and transport of proton beams from laser-target interaction. *Physics of Plasmas*, 13(6):063105, June 2006.

[84] G. Chen, L. Chacn, and D.C. Barnes. An energy- and charge-conserving, implicit, electrostatic particle-in-cell algorithm. *Journal of Computational Physics*, 230(18):7018–7036, August 2011.

[85] S. Banerjee, M. Baudisch, Jens Biegert, A. Borot, A. Borzsonyi, Dimitrios Charalambidis, Todd Ditmire, Zsolt Diveki, P. Dombi, Klaus Ertel, M. Galimberti, J. Fulop, E. Gaul, Constantin L. Haefner, M. Hemmer, C. Hernandez-Gomez, M. Kalashnikov, D. Kandula, A. Kovacs, R. Lopez-Martens, Paul D. Mason, I. Marton, I. Musgrave, Karoly Osvay, M. Prandolini, E. Racz, P. Racz, R. Riedel, I. Ross, J. Rosseau, M. Schulz, F. Tavella, Alexandre Thai, and I. Will. Conceptual design of the laser systems for the attosecond light pulse source. In *CLEO: 2013*, page CTu2D.6. Optical Society of America, 2013.

[86] S. Gales. Laser driven nuclear science and applications: The need of high efficiency, high power and high repetition rate laser beams. *Eur. Phys. J. Special Topics*, 224:2631–2637, 2015.

[87] Andrea Macchi, Marco Borghesi, and Matteo Passoni. Ion acceleration by superintense laser-plasma interaction. *Rev. Mod. Phys.*, 85:751–793, 2013.

[88] S. Kneip, C. McGuffey, S. R. Nagel, C. Palmer, C. Bellei, J. Schreiber, C. Huntington, F. Dollar, T. Matsuoka, V. Chvykov, G. Kalintchenko, V. Yanovsky, A. Maksimchuk,

K. Ta Phuoc, S. P. D. Mangles, K. Krushelnick, and Z. Najmudin. Comparative study of betatron radiation from laser-wakefield and direct-laser accelerated bunches of relativistic electrons, 2009.

[89] U. Masood, M. Bussmann, T.E. Cowan, W. Enghardt, L. Karsch, F. Kroll, U. Schramm, and J. Pawelke. A compact solution for ion beam therapy with laser accelerated protons. *Applied Physics B*, 117(1):41–52, 2014.

[90] P. L. Poole, C. D. Andereck, D. W. Schumacher, R. L. Daskalova, S. Feister, K. M. George, C. Willis, K. U. Akli, and E. A. Chowdhury. Liquid crystal films as on-demand, variable thickness (505000nm) targets for intense lasers. *Physics of Plasmas*, 21(6):063109, June 2014.

[91] Poole. P. L. *Liquid crystals as high repetition rate targets for ultra intense laser systems.* PhD thesis, The Ohio State University, 2015. Retrieved from https://etd.ohiolink.edu/.

[92] Anthony Zingale, Jordan Purcell, Patrick Poole, Ginevra Cochran, Christopher Willis, and Douglass Schumacher. ¿ 1 hz renewable films for plasma mirrors for high repetition rate petawatt class laser systems. *Bulletin of the American Physical Society*, 62, 2017.

[93] D.W. Schumacher, P.L. Poole, C. Willis, G.E. Cochran, R. Daskalova, J. Purcell, and R. Heery. Liquid crystal targets and plasma mirrors for laser based ion acceleration. *Journal of Instrumentation*, 12(04):C04023, 2017.

[94] S. Karsch, S. Düsterer, H. Schwoerer, F. Ewald, D. Habs, M. Hegelich, G. Pretzler, A. Pukhov, K. Witte, and R. Sauerbrey. High-intensity laser induced ion acceleration from heavy-water droplets. *Phys. Rev. Lett.*, 91:015001, Jul 2003.

[95] M. Schnürer, S. Ter-Avetisyan, P. V. Nickles, and A. A. Andreev. Influence of target system on the charge state, number, and spectral shape of ion beams accelerated by femtosecond high-intensity laser pulses. *Physics of Plasmas (1994-present)*, 14(3):–, 2007.

[96] U. Zastrau, P. Sperling, A. Becker, T. Bornath, R. Bredow, T. Döppner, S. Dziarzhytski, T. Fennel, L. B. Fletcher, E. Förster, C. Fortmann, S. H. Glenzer, S. Göde, G. Gregori, M. Harmand, V. Hilbert, B. Holst, T. Laarmann, H. J. Lee, T. Ma, J. P. Mithen, R. Mitzner, C. D. Murphy, M. Nakatsutsumi, P. Neumayer, A. Przystawik, S. Roling, M. Schulz, B. Siemer, S. Skruszewicz, J. Tiggesbäumker, S. Toleikis, T. Tschentscher, T. White, M. Wöstmann, H. Zacharias, and R. Redmer. Equilibration dynamics and conductivity of warm dense hydrogen. *Phys. Rev. E*, 90:013104, Jul 2014.

[97] S. Feister, J. A. Nees, J. T. Morrison, K. D. Frische, C. Orban, E. A. Chowdhury, and W. M. Roquemore. A novel femtosecond-gated, high-resolution, frequency-shifted shearing interferometry technique for probing pre-plasma expansion in ultra-intense laser experimentsa). *Review of Scientific Instruments*, 85(11):–, 2014.

[98] M. Nishiuchi, H. Daido, A. Yogo, S. Orimo, K. Ogura, J. Ma, A. Sagisaka, M. Mori, A. S. Pirozhkov, H. Kiriyama, S. V. Bulanov, T. Zh. Esirkepov, I. W. Choi, C. M. Kim, T. M. Jeong, T. J. Yu, J. H. Sung, S. K. Lee, N. Hafz, K. H. Pae, Y.-C. Noh,

D.-K. Ko, J. Lee, Y. Oishi, K. Nemoto, H. Nagatomo, K. Nagai, and H. Azuma. Efficient production of a collimated mev proton beam from a polyimide target driven by an intense femtosecond laser pulse. *Physics of Plasmas (1994-present)*, 15(5):–, 2008.

[99] A. Henig, S. Steinke, M. Schnürer, T. Sokollik, R. Hörlein, D. Kiefer, D. Jung, J. Schreiber, B. M. Hegelich, X. Q. Yan, J. Meyer-ter Vehn, T. Tajima, P. V. Nickles, W. Sandner, and D. Habs. Radiation-pressure acceleration of ion beams driven by circularly polarized laser pulses. *Phys. Rev. Lett.*, 103:245003, 2009.

[100] Peter J. Collings; Michael Hird. *Introduction to Liquid Crystals Chemistry and Physics*. Taylor & Francis Ltd., 1997.

[101] Christopher Willis, Patrick L. Poole, Kramer U. Akli, Douglass W. Schumacher, and Richard R. Freeman. A confocal microscope position sensor for micron-scale target alignment in ultra-intense laser-matter experiments. *Review of Scientific Instruments*, 86(5):–, 2015.

[102] Ch Ziener, P.S. Foster, E.J. Divall, C. J. Hooker, M.H.R. Hutchinson, A. J. Langley, and D. Neely. Specular reflectivity of plasma mirrors as a function of intensity, pulse duration, and angle of incidence. *Journal of Applied Physics*, 93(1):768–770, 2003.

[103] J. H. Bin, K. Allinger, K. Khrennikov, S. Karsch, P. R. Bolton, and J. Schreiber. Dynamics of laser-driven proton acceleration exhibited by measured laser absorptivity and reflectivity. *Scientific Reports*, 7:43548, March 2017.

[104] B. Dromey, S. Kar, M. Zepf, and P. Foster. The plasma mirrorA subpicosecond optical switch for ultrahigh power lasers. *Review of Scientific Instruments*, 75(3):645–649, February 2004.

[105] G. G. Scott, V. Bagnoud, C. Brabetz, R. J. Clarke, J. S. Green, R. I. Heathcote, H. W. Powell, B. Zielbauer, T. D. Arber, P McKenna, and D. Neely. Optimization of plasma mirror reflectivity and optical quality using double laser pulses. *New Journal of Physics*, 17(3):033027, 2015.

[106] A Kon, M Nakatsutsumi, S Buffechoux, Z L Chen, J Fuchs, Z Jin, and R Kodama. Geometrical optimization of an ellipsoidal plasma mirror toward tight focusing of ultra-intense laser pulse. *Journal of Physics: Conference Series*, 244(3):032008, 2010.

[107] M. Nakatsutsumi, A. Kon, S. Buffechoux, P. Audebert, J. Fuchs, and R. Kodama. Fast focusing of short-pulse lasers by innovative plasma optics toward extreme intensity. *Opt. Lett.*, 35(13):2314–2316, Jul 2010.

[108] Robbie Wilson, Martin King, J. Ross Gray, C. David Carroll, J. Rachel Dance, M. Nicholas Butler, Chris Armstrong, J. Steve Hawkes, J. Robert Clarke, J. David Robertson, Cyril Bourgenot, David Neely, and Paul McKenna. Development of Focusing Plasma Mirrors for Ultraintense Laser-Driven Particle and Radiation Sources. *Quantum Beam Science*, 2(1), 2018.

[109] B. H. Shaw, S. Steinke, J. van Tilborg, and W. P. Leemans. Reflectance characterization of tape-based plasma mirrors. *Physics of Plasmas*, 23(6):063118, 2016.

[110] V. M. Ovchinnikov, D. W. Schumacher, M. McMahon, E. A. Chowdhury, C. D. Chen, A. Morace, and R. R. Freeman. Effects of Preplasma Scale Length and Laser Intensity on the Divergence of Laser-Generated Hot Electrons. *Physical Review Letters*, 110(6):065007, February 2013.

[111] S. Jiang, A. G. Krygier, D. W. Schumacher, K. U. Akli, and R. R. Freeman. Effects of front-surface target structures on properties of relativistic laser-plasma electrons. *Physical Review E*, 89(1):013106, January 2014.

[112] S. Jiang, L.L. Ji, H. Audesirk, K.M. George, J. Snyder, A. Krygier, P. Poole, C. Willis, R. Daskalova, E. Chowdhury, N.S. Lewis, D.W. Schumacher, A. Pukhov, R.R. Freeman, and K.U. Akli. Microengineering Laser Plasma Interactions at Relativistic Intensities. *Physical Review Letters*, 116(8):085002, February 2016.

[113] P. McKenna, D. C. Carroll, O. Lundh, F. Nrnberg, K. Markey, S. Bandyopadhyay, D. Batani, R. G. Evans, R. Jafer, S. Kar, D. Neely, D. Pepler, M. N. Quinn, R. Redaelli, M. Roth, C.-G. Wahlstrm, X. H. Yuan, and M. Zepf. Effects of front surface plasma expansion on proton acceleration in ultraintense laser irradiation of foil targets. *Laser and Particle Beams*, 26(4):591–596, December 2008.

[114] K. B. Wharton, C. D. Boley, A. M. Komashko, A. M. Rubenchik, J. Zweiback, J. Crane, G. Hays, T. E. Cowan, and T. Ditmire. Effects of nonionizing prepulses in high-intensity laser-solid interactions. *Physical Review E*, 64(2):025401, July 2001.

[115] Rahul C. Shah, Randall P. Johnson, Tsutomu Shimada, Kirk A. Flippo, Juan C. Fernandez, and B. M. Hegelich. High-temporal contrast using low-gain optical parametric amplification. *Optics Letters*, 34(15):2273–2275, August 2009.

[116] S. Kourtev, N. Minkovski, L. Canova, A. Jullien, O. Albert, and S. M. Saltiel. Improved nonlinear cross-polarized wave generation in cubic crystals by optimization of the crystal orientation. *JOSA B*, 26(7):1269–1275, July 2009.

[117] Henry C. Kapteyn, Margaret M. Murnane, Abraham Szoke, and Roger W. Falcone. Prepulse energy suppression for high-energy ultrashort pulses using self-induced plasma shuttering. *Optics Letters*, 16(7):490–492, April 1991.

[118] G. Doumy, F. Qur, O. Gobert, M. Perdrix, Ph. Martin, P. Audebert, J. C. Gauthier, J.-P. Geindre, and T. Wittmann. Complete characterization of a plasma mirror for the production of high-contrast ultraintense laser pulses. *Physical Review E*, 69(2):026402, February 2004.

[119] C. Thaury, F. Qur, J.-P. Geindre, A. Levy, T. Ceccotti, P. Monot, M. Bougeard, F. Rau, P. dOliveira, P. Audebert, R. Marjoribanks, and Ph Martin. Plasma mirrors for ultrahigh-intensity optics. *Nature Physics*, 3(6):424–429, June 2007.

[120] Yi Cai, Wentao Wang, Changquan Xia, Jiansheng Liu, Li Liu, Cheng Wang, Yi Xu, Yuxin Leng, Ruxin Li, and Zhizhan Xu. Time-resolved measurements on reflectivity of an ultrafast laser-induced plasma mirror. *Physics of Plasmas*, 16(10):103104, October 2009.

[121] Dmitriy Panasenko, Anthony J. Shu, Anthony Gonsalves, Kei Nakamura, Nicholas H. Matlis, Csaba Toth, and Wim P. Leemans. Demonstration of a plasma mirror based on a laminar flow water film. *Journal of Applied Physics*, 108(4):044913, August 2010.

[122] A. S. Pirozhkov, I. W. Choi, J. H. Sung, S. K. Lee, T. J. Yu, T. M. Jeong, I J. Kim, N. Hafz, C. M. Kim, K. H. Pae, Y.-C. Noh, D.-K. Ko, J. Lee, A. P. L. Robinson, P. Foster, S. Hawkes, M. Streeter, C. Spindloe, P. McKenna, D. C. Carroll, C.-G. Wahlstrm, M. Zepf, D. Adams, B. Dromey, K. Markey, S. Kar, Y. T. Li, M. H. Xu, H. Nagatomo, M. Mori, A. Yogo, H. Kiriyama, K. Ogura, A. Sagisaka, S. Orimo, M. Nishiuchi, H. Sugiyama, T. Zh. Esirkepov, H. Okada, S. Kondo, S. Kanazawa, Y. Nakai, A. Akutsu, T. Motomura, M. Tanoue, T. Shimomura, M. Ikegami, I. Daito, M. Kando, T. Kameshima, P. Bolton, S. V. Bulanov, H. Daido, and D. Neely. Diagnostic of laser contrast using target reflectivity. *Applied Physics Letters*, 94(24):241102, June 2009.

[123] S. Steinke, J. van Tilborg, C. Benedetti, C. G. R. Geddes, C. B. Schroeder, J. Daniels, K. K. Swanson, A. J. Gonsalves, K. Nakamura, N. H. Matlis, B. H. Shaw, E. Esarey, and W. P. Leemans. Multistage coupling of independent laser-plasma accelerators. *Nature*, 530:190, February 2016.

[124] R. G. Horn. Refractive indices and order parameters of two liquid crystals. *Journal de Physique*, 39(1):105–109, January 1978.

[125] C. Rdel, M. Heyer, M. Behmke, M. Kbel, O. Jckel, W. Ziegler, D. Ehrt, M. C. Kaluza, and G. G. Paulus. High repetition rate plasma mirror for temporal contrast enhancement of terawatt femtosecond laser pulses by three orders of magnitude. *Applied Physics B*, 103(2):295–302, May 2011.

[126] C. J. Hooker, S. Blake, O. Chekhlov, R. J. Clarke, J. L. Collier, E. J. Divall, K. Ertel, P. S. Foster, S. J. Hawkes, P. Holligan, B. Landowski, W. J. Lester, D. Neely, B. Parry, R. Pattathil, M. Streeter, and B. E. Wyborn. Commissioning the astra gemini petawatt ti:sapphire laser system. In *2008 Conference on Lasers and Electro-Optics and 2008 Conference on Quantum Electronics and Laser Science*, pages 1–2, May 2008.

[127] N. M. Naumova, C. P. Hauri, J. A. Nees, I. V. Sokolov, R. Lopez-Martens, and G. A. Mourou. Towards efficient generation of attosecond pulses from overdense plasma targets. *New Journal of Physics*, 10(2):025022, 2008.

[128] C. Thaury, H. George, F. Qur, R. Loch, J.-P. Geindre, P. Monot, and Ph Martin. Coherent dynamics of plasma mirrors. *Nature Physics*, 4(8):631–634, August 2008.

[129] A. Pukhov, T. Baeva, D. an der Brgge, and S. Mnster. Relativistic high harmonics and (sub-)attosecond pulses: relativistic spikes and relativistic mirror. *The European Physical Journal D*, 55(2):407, November 2009.

[130] A. Lawrence-Douglas. *Ionisation effects for laser-plasma interactions by particle-in-cell code*. PhD thesis, University of Warwick, 2013.

[131] P. Gibbon. *Short Pulse Laser Interactions with Matter: An Introduction.* Imperial College Press, 2005.

[132] P. B. Corkum. Plasma perspective on strong field multiphoton ionization. *Physical Review Letters*, 71(13):1994–1997, September 1993.

[133] L.V. Keldysh. Ionization in the field of a strong electromagnetic wave. *Journal of Experimental and Theoretical Physics*, 20.5:1307–1314, 1965.

[134] M.V. Ammosov. Tunnel ionization of complex atoms and of atomic ions in an alternating electromagnetic field. *Journal of Experimental and Theoretical Physics*, 64:1191–1194, 1986.

[135] N. B. Delone and Vladimir P. Krainov. Tunneling and barrier-suppression ionization of atoms and ions in a laser radiation field. *Physics-Uspekhi*, 41(5):469, 1998.

[136] F. A. Ilkov, J. E. Decker, and S. L. Chin. Ionization of atoms in the tunnelling regime with experimental evidence using Hg atoms. *Journal of Physics B: Atomic, Molecular and Optical Physics*, 25(19):4005, 1992.

[137] Michael E. Jones, Don S. Lemons, Rodney J. Mason, Vincent A. Thomas, and Dan Winske. A Grid-Based Coulomb Collision Model for PIC Codes. *Journal of Computational Physics*, 123(1):169–181, January 1996.

[138] L. Spitzer. *Physics of fully ionized gases.* Courier Corporation, 1963.

[139] Y. Sentoku and A. J. Kemp. Numerical methods for particle simulations at extreme densities and temperatures: Weighted particles, relativistic collisions and reduced currents. *Journal of Computational Physics*, 227(14):6846–6861, July 2008.

[140] V.L. Ginsburg. *Propagation of Electromagnetic Waves in Plasmas.* New York: Gordon and Breach, 1960.

[141] S. C. Wilks and W. L. Kruer. Absorption of ultrashort, ultra-intense laser light by solids and overdense plasmas. *IEEE Journal of Quantum Electronics*, 33(11):1954–1968, November 1997.

[142] T.Y. Brian Yang, William L. Kruer, A. Bruce Langdon, and Tudor W. Johnston. Mechanisms for collisionless absorption of light waves obliquely incident on overdense plasmas with steep density gradients. *Physics of Plasmas*, 3(7):2702–2709, July 1996.

[143] Erich S. Weibel. Anomalous Skin Effect in a Plasma. *The Physics of Fluids*, 10(4):741–748, April 1967.

[144] P. J. Catto and Richard M. More. Sheath inverse bremsstrahlung in laser produced plasmas. *The Physics of Fluids*, 20(4):704–705, April 1977.

[145] A. J. Kemp and L. Divol. What is the surface temperature of a solid irradiated by a Petawatt laser? *Physics of Plasmas*, 23(9):090703, September 2016.

[146] G. E. Kemp, A. Link, Y. Ping, H. S. McLean, P. K. Patel, R. R. Freeman, D. W. Schumacher, H. F. Tiedje, Y. Y. Tsui, R. Ramis, and R. Fedosejevs. On specular reflectivity measurements in high and low-contrast relativistic laser-plasma interactions. *Physics of Plasmas*, 22(1):013110, January 2015.

[147] E. L. Clark, K. Krushelnick, J. R. Davies, M. Zepf, M. Tatarakis, F. N. Beg, A. Machacek, P. A. Norreys, M. I. K. Santala, I. Watts, and A. E. Dangor. Measurements of energetic proton transport through magnetized plasma from intense laser interactions with solids. *Phys. Rev. Lett.*, 84:670–673, Jan 2000.

[148] A. Maksimchuk, S. Gu, K. Flippo, D. Umstadter, and V. Yu. Bychenkov. Forward ion acceleration in thin films driven by a high-intensity laser. *Phys. Rev. Lett.*, 84:4108–4111, May 2000.

[149] R. A. Snavely, M. H. Key, S. P. Hatchett, T. E. Cowan, M. Roth, T. W. Phillips, M. A. Stoyer, E. A. Henry, T. C. Sangster, M. S. Singh, S. C. Wilks, A. MacKinnon, A. Offenberger, D. M. Pennington, K. Yasuike, A. B. Langdon, B. F. Lasinski, J. Johnson, M. D. Perry, and E. M. Campbell. Intense high-energy proton beams from petawatt-laser irradiation of solids. *Phys. Rev. Lett.*, 85:2945–2948, 2000.

[150] Andrea Macchi, Silvia Veghini, Tatyana V Liseykina, and Francesco Pegoraro. Radiation pressure acceleration of ultrathin foils. *New Journal of Physics*, 12(4):045013, 2010.

[151] L. Yin, B. J. Albright, B. M. Hegelich, and J. C. Fernandez. Gev laser ion acceleration from ultrathin targets: The laser break-out afterburner. *Laser and Particle Beams*, 24:291–298, 6 2006.

[152] Stephen P. Hatchett, Curtis G. Brown, Thomas E. Cowan, Eugene A. Henry, Joy S. Johnson, Michael H. Key, Jeffrey A. Koch, A. Bruce Langdon, Barbara F. Lasinski, Richard W. Lee, Andrew J. Mackinnon, Deanna M. Pennington, Michael D. Perry, Thomas W. Phillips, Markus Roth, T. Craig Sangster, Mike S. Singh, Richard A. Snavely, Mark A. Stoyer, Scott C. Wilks, and Kazuhito Yasuike. Electron, photon, and ion beams from the relativistic interaction of petawatt laser pulses with solid targets. *Physics of Plasmas (1994-present)*, 7(5):2076–2082, 2000.

[153] Hiroyuki Daido, Mamiko Nishiuchi, and Alexander S Pirozhkov. Review of laser-driven ion sources and their applications. *Reports on Progress in Physics*, 75(5):056401, 2012.

[154] Marco Borghesi. Laser-driven ion acceleration: State of the art and emerging mechanisms. *Nuclear Instruments and Methods in Physics Research Section A: Accelerators, Spectrometers, Detectors and Associated Equipment*, 740:6 – 9, 2014. Proceedings of the first European Advanced Accelerator Concepts Workshop 2013.

[155] T. Esirkepov, M. Borghesi, S. V. Bulanov, G. Mourou, and T. Tajima. Highly efficient relativistic-ion generation in the laser-piston regime. *Phys. Rev. Lett.*, 92:175003, 2004.

[156] Emmanuel dHumires, Erik Lefebvre, Laurent Gremillet, and Victor Malka. Proton acceleration mechanisms in high-intensity laser interaction with thin foils. *Physics of Plasmas*, 12(6):062704, 2005.

[157] S. C. Wilks, W. L. Kruer, M. Tabak, and A. B. Langdon. Absorption of ultra-intense laser pulses. *Phys. Rev. Lett.*, 69:1383–1386, Aug 1992.

[158] P. Mora. Plasma expansion into a vacuum. *Phys. Rev. Lett.*, 90:185002, 2003.

[159] J. Fuchs, P. Antici, E. dHumires, E. Lefebvre, M. Borghesi, E. Brambrink, C. A. Cecchetti, M. Kaluza, V. Malka, M. Manclossi, S. Meyroneinc, P. Mora, J. Schreiber, T. Toncian, H. Ppin, and P. Audebert. Laser-driven proton scaling laws and new paths towards energy increase. *Nature Physics*, 2(1):48–54, January 2006.

[160] D. Margarone, O. Klimo, I. J. Kim, J. Prokůpek, J. Limpouch, T. M. Jeong, T. Mocek, J. Pšikal, H. T. Kim, J. Proška, K. H Nam, L. Štolcová, I. W. Choi, S. K. Lee, J. H. Sung, T. J. Yu, and G. Korn. Laser-driven proton acceleration enhancement by nanostructured foils. *Phys. Rev. Lett.*, 109:234801, Dec 2012.

[161] O Klimo, J Psikal, J Limpouch, J Proska, F Novotny, T Ceccotti, V Floquet, and S Kawata. Short pulse laser interaction with micro-structured targets: simulations of laser absorption and ion acceleration. *New Journal of Physics*, 13(5):053028, 2011.

[162] Y. Sentoku, K. Mima, H. Ruhl, Y. Toyama, R. Kodama, and T. E. Cowan. Laser light and hot electron micro focusing using a conical target. *Physics of Plasmas*, 11(6):3083–3087, 2004.

[163] J. Badziak, S. Jaboski, P. Parys, M. Rosiski, J. Woowski, A. Szydowski, P. Antici, J. Fuchs, and A. Mancic. Ultraintense proton beams from laser-induced skin-layer ponderomotive acceleration. *Journal of Applied Physics*, 104(6), 2008.

[164] K Ogura, M Nishiuchi, A S Pirozhkov, T Tanimoto, A Sagisaka, T Zh. Esirkepov, M Kando, T Shizuma, T Hayakawa, and H Kiriyama. Proton acceleration to 40\,MeV using a high intensity, high contrast optical parametric chirped-pulse amplification/Ti:sapphire hybrid laser system. *Opt. Lett.*, 37(14):2868–2870, 2012.

[165] A. Higginson, R. J. Gray, M. King, R. J. Dance, S. D. R. Williamson, N. M. H. Butler, R. Wilson, R. Capdessus, C. Armstrong, J. S. Green, S. J. Hawkes, P. Martin, W. Q. Wei, S. R. Mirfayzi, X. H. Yuan, S. Kar, M. Borghesi, R. J. Clarke, D. Neely, and P. McKenna. Near-100 MeV protons via a laser-driven transparency-enhanced hybrid acceleration scheme. *Nature Communications*, 9(1):724, February 2018.

[166] A P L Robinson, P Gibbon, M Zepf, S Kar, R G Evans, and C Bellei. Relativistically correct hole-boring and ion acceleration by circularly polarized laser pulses. *Plasma Physics and Controlled Fusion*, 51(2):024004, 2009.

[167] S Kar, K F Kakolee, M Cerchez, D Doria, A Macchi, P McKenna, D Neely, J Osterholz, K Quinn, B Ramakrishna, G Sarri, O Willi, X H Yuan, M Zepf, and M Borghesi. Experimental investigation of hole boring and light sail regimes of rpa by varying laser and target parameters. *Plasma Physics and Controlled Fusion*, 55(12):124030, 2013.

[168] S. S. Bulanov, E. Esarey, C. B. Schroeder, S. V. Bulanov, T. Zh. Esirkepov, M. Kando, F. Pegoraro, and W. P. Leemans. Radiation pressure acceleration: The factors limiting maximum attainable ion energy. *Physics of Plasmas*, 23(5):056703, 2016.

[169] X. Q. Yan, T. Tajima, M. Hegelich, L. Yin, and D. Habs. Theory of laser ion acceleration from a foil target of nanometer thickness. *Applied Physics B*, 98(4):711–721, Mar 2010.

[170] S.V Bulanov, T.Zh Esirkepov, V.S Khoroshkov, A.V Kuznetsov, and F Pegoraro. Oncological hadrontherapy with laser ion accelerators. *Physics Letters A*, 299(2):240 – 247, 2002.

[171] E. Fourkal, I. Velchev, and C.-M. Ma. Coulomb explosion effect and the maximum energy of protons accelerated by high-power lasers. *Phys. Rev. E*, 71:036412, Mar 2005.

[172] L. Yin, B. J. Albright, K. J. Bowers, D. Jung, J. C. Fernández, and B. M. Hegelich. Three-dimensional dynamics of breakout afterburner ion acceleration using high-contrast short-pulse laser and nanoscale targets. *Phys. Rev. Lett.*, 107:045003, Jul 2011.

[173] Bruno Gonzalez-Izquierdo, Martin King, Ross J. Gray, Robbie Wilson, Rachel J. Dance, Haydn Powell, David A. Maclellan, John McCreadie, Nicholas M. H. Butler, Steve Hawkes, James S. Green, Chris D. Murphy, Luca C. Stockhausen, David C. Carroll, Nicola Booth, Graeme G. Scott, Marco Borghesi, David Neely, and Paul McKenna. Towards optical polarization control of laser-driven proton acceleration in foils undergoing relativistic transparency. *Nature Communications*, 7:12891, September 2016.

[174] F. Wagner, S. Bedacht, V. Bagnoud, O. Deppert, S. Geschwind, R. Jaeger, A. Ortner, A. Tebartz, B. Zielbauer, D. H. H. Hoffmann, and M. Roth. Simultaneous observation of angularly separated laser-driven proton beams accelerated via two different mechanisms. *Physics of Plasmas*, 22(6):063110, 2015.

[175] H. W. Powell, M. King, R. J. Gray, D. A. MacLellan, B. Gonzalez-Izquierdo, L. C. Stockhausen, G. Hicks, N. P. Dover, D. R. Rusby, D. C. Carroll, H. Padda, R. Torres, S. Kar, R. J. Clarke, I. O. Musgrave, Z. Najmudin, M. Borghesi, D. Neely, and P. McKenna. Proton acceleration enhanced by a plasma jet in expanding foils undergoing relativistic transparency. *New Journal of Physics*, 17(10):103033, 2015.

[176] L Obst, J Metzkes-Ng, S Bock, G E Cochran, T E Cowan, T Oksenhendler, P L Poole, I Prencipe, M Rehwald, C Rdel, H-P Schlenvoigt, U Schramm, D W Schumacher, T Ziegler, and K Zeil. On-shot characterization of single plasma mirror temporal contrast improvement. *Plasma Physics and Controlled Fusion*, 60(5):054007, 2018.

[177] M J V Streeter, P S Foster, F H Cameron, M Borghesi, C Brenner, D C Carroll, E Divall, N P Dover, B Dromey, P Gallegos, J S Green, S Hawkes, C J Hooker, S Kar, P McKenna, S R Nagel, Z Najmudin, C A J Palmer, R Prasad, K E Quinn, P P Rajeev, A P L Robinson, L Romagnani, J Schreiber, C Spindloe, S Ter-Avetisyan, O Tresca, M Zepf, and D Neely. Relativistic plasma surfaces as an efficient second harmonic generator. *New Journal of Physics*, 13(2):023041, 2011.

[178] D. W. Schumacher, G. E. Kemp, A. Link, R. R. Freeman, and L. D. Van Woerkom. The shaped critical surface in high intensity laser plasma interactions. *Physics of Plasmas*, 18(1):013102, 2011.

[179] A. Buck, K. Zeil, A. Popp, K. Schmid, A. Jochmann, S. D. Kraft, B. Hidding, T. Kudyakov, C. M. S. Sears, L. Veisz, S. Karsch, J. Pawelke, R. Sauerbrey, T. Cowan, F. Krausz, and U. Schramm. Absolute charge calibration of scintillating screens for relativistic electron detection. *Review of Scientific Instruments*, 81(3):033301, 2010.

[180] M. Thevenet, A. Leblanc, S. Kahaly, H. Vincenti, A. Vernier, F. Quere, and J. Faure. Vacuum laser acceleration of relativistic electrons using plasma mirror injectors. *Nat Phys*, 12(4):355–360, 2016.